UNIVERSITÀ DEGLI STUDI DI TRIESTE

UNIVERSITÀ DEGLI STUDI DI TRIESTE

XXXIII CICLO DEL DOTTORATO DI RICERCA IN

Scienze della terra e meccanica dei fluidi

Funded by: International Center for Theoretical Physics (ICTP)

Titolo della Tesi

Crustal structure and discontinuities beneath the Nepal Himalaya using seismic ambient noise and teleseismic P wave coda autocorrelation

Settore scientifico-disciplinare:

Geo/10 Geofisica della Terra Solida

Dottorando: **Hari Ram Thapa**

Coordinatore: Prof. Stefano Maset

Supervisore di Tesi: Prof. Abdelkrim Aoudia

Co- Supervisore di Tesi: Dr. Surya Pachhai

Anno Accademico 2019/2020

Crustal structure and discontinuities beneath the Nepal Himalaya using seismic ambient noise and teleseismic P wave coda autocorrelation

Thapa Hari Ram

University of Trieste

A thesis submitted for the degree of

Doctor of Philosophy

September 2021

Contents

List of Abbreviations

MFT : Main Frontal Thrust

MBT : Main Boundary Thrust

MHT : Main Himalayan Thrust

MCT : Main Central Thrust

STD : South Tibet Detachment

IYS : Indus Yarlung Suture

SWT : Surface Wave Tomography

ANT : Ambient Noise Tomography

GHS : Greater Himalayan Sequence

LHS : Lesser Himalayan Sequence

rjMcMC : reversible jump Markov chain Monte Carlo

PWS : Phase Weighted Stacking

Abstract

Nepal is a seismically active region because of its tectonic setting, and it already has hosted many disastrous earthquakes in the past. For a better understanding of the crustal structure, physics of earthquakes as well as their detailed high-resolution location and monitoring, and to mitigate the real-time seismic hazard, an adequate 3-D regional velocity model is needed, but so far, the 3-D velocity structure in this region is poorly understood. Here, we present a new high-resolution 3-D shear-wave velocity structure down to 60 km depth beneath the Himalaya Nepal using ambient noise cross-correlations. Our results show significant lateral variation in crustal structure and thus, correlate well with the known geological and tectonic features of the study area. Precise depth of discontinuities is crucial to mitigate the seismic risk. Hence, we also present the application of autocorrelation of teleseismic P coda to recover the shallow and deeper interface in the crust beneath Nepal. The results show the high-resolution images of four major seismic reflectors in the crust beneath Central Nepal. The shallow discontinuity recovered from our study well supported the geology of Nepal. Our results provide for the first-time good constraint both on the seismogenesis and on the earthquake hazard in the Nepal Himalaya.

Keywords: Nepal Himalaya, Ambient noise, Surface wave tomography, Bayesian inversion, 3-D shear wave velocity, Autocorrelation, P-wave reflectivity, S-wave reflectivity, discontinuities

Chapter 1: Introduction

The geodynamic evolution of the lithosphere beneath Nepal has greatly been influenced by the subduction of the Indian plate beneath the Tibetan Plate (Copley et al., 2010). The Himalayan range is thought to have been formed by the collision between the Eurasian and the Indian plate, and to consist of detached slices of the crust of the Indian plate (Molnar, 1984). Seismic tomography images (Monsalve et al., 2008) have shown that the Indian crust extends far northward beneath Eurasia, causing the uplift of the Himalayan region, ultimately thickening the crust in the collision zone. Here, the crust-mantle boundary (Moho) depth is among the deepest observed in the world. In particular, the thickness of the crust varies from 40 to 70 km from Southern Nepal to Southern Tibet (Nábělek et al., 2009; Schulte-Pelkum et al., 2005).

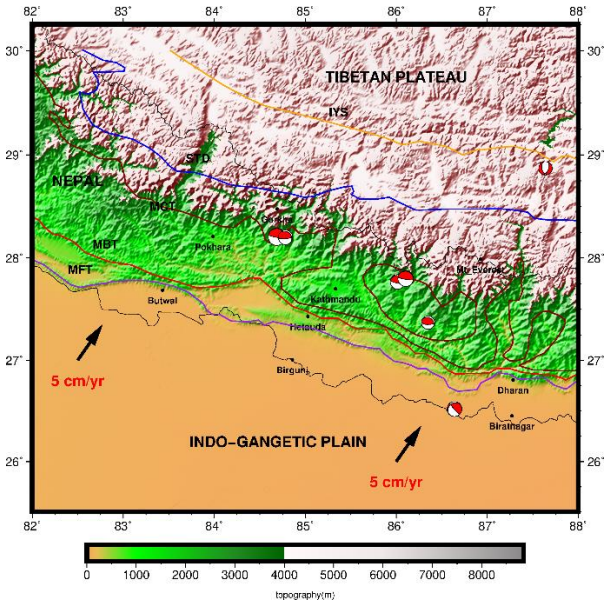

Figure 1.1: Topographic map of the Nepal and its surroundings. The coloured beach balls indicate earthquake after 1976 with magnitude greater than 6. The data for focal mechanism of earthquakes are obtained from Global CMT catalog.

1.1 Tectonic Setting

The continuous movement of the Indian plate toward Eurasia eventually forced itself to break into slices at depth, forming lower and upper blocks. The Main Himalayan Thrust (MHT) is considered as the breaking plane between these two blocks. Nowadays, the Indian

plate is moving towards Eurasia at a rate of 5 cm/year, resulting in a stress build-up in the Himalayan region (Ader et al., 2012; Castaldo et al., 2017; Lavé & Avouac, 2000). Due to this stress build-up, an enormous amount of energy is stored in this region. The stored energy can only be released by major earthquakes, which ultimately makes the Himalayan region vulnerable to major damaging earthquakes. Within the political boundaries of Nepal, there are three major thrust faults. The north-most of these faults is the Main Central Thrust (MCT), which marks a transition from the high-grade metamorphic Greater Crystalline Himalayan Sequence (GCHS) to the lower-grade Himalayan Sequence (LHS). The GCHS is constrained between the Southern Tibetan Detachment (STD) and the MCT. It has been found that STD and MCT have opposite directions of motion. The STD shows a normal motion, while the MCT shows a thrusting motion (Beaumont et al., 2001). The main active fault along the Himalayas is the Main Frontal Thrust (MFT), which marks the southern edge of the Himalayan foothills. The Main Boundary Thrust (MBT) is located north of the MFT and south of MCT. The Nepal Himalayan seismicity is essentially associated with the MBT and a series of overthrust, normal and transverse faults (Ader et al., 2012).

1.2 Objectives and Motivation

A lot of significant scientific questions remain unanswered about the Himalayan formation and seismic hazards, including the geometry of the MHT. The largest instrumentally recorded earthquake in Nepal, for example, the 1934 M_w 8.2 Bihar-Nepal earthquake, 2015 M_W7.8 Gorkha Earthquake, and its biggest aftershocks M_w 7.3 are all associated with rupture of MHT. Bihar-Nepal earthquake has ruptured a >150-km segment of the MHT from Eastern to Central Nepal (Sapkota et al., 2013) while it was reported that the deep segment of MHT was ruptured further west by the Gorkha earthquake and its biggest aftershocks in Central Nepal (Avouac et al., 2015; Duputel et al., 2016; Elliott et al., 2016; Grandin et al., 2015; Lindsey et al., 2015). Since most of the seismicity in Nepal is associated with MHT, it is essential to have an understanding of the velocity structure of the crust and the geometry of the MHT as such information helps in estimating the seismogenic zone beneath the Nepal Himalaya.

The Nepal Himalaya already have experienced many disastrous earthquakes in the past. Figure1.1 shows the distribution of earthquakes having magnitude greater or equal to 6 in Nepal since 1976. It has been reported that small earthquakes (Mw<3) occur almost every day, including occasionally felt earthquakes (4<Mw<5), while moderate earthquakes (6<Mw<7) occur every 10-20 years (Bilham, 2019). To mitigate the real-time seismic hazard, Earthquake Early Warning (EEW) system is regarded as a useful tool (Hsiao et al., 2009). As we know that EEW estimates the severity and onset time of ground shaking after an earthquake based on the lead time. The lead time is difference between S-wave arrival time and P wave arrival time at target. Time is a critical parameter in any EEW system. So, for the precise computation of lead time, a high resolution 3-D regional velocity model is crucial. There are few studies in the Nepal Himalaya by using Ambient Noise Tomography, local earthquake tomography, joint inversion of surface wave dispersion and receiver function data (e.g., Guo et al., 2009; Monsalve et al., 2008; Z. J. Xu et al., 2013). However, the 3-D velocity structure in this region is poorly understood.

The main objective of this study is to improve the 2-D tomography and 3-D shear wave velocity structure in the eastern and central parts of Nepal from Ambient Noise Tomography. The benefits of using ambient noise tomography technique compared to traditional earthquake-based surface wave studies are that; we can take full advantage of the dense distribution of seismic stations across Nepal and part of South Tibet allowing for dense path coverage across the Himalaya Nepal. Again, we can retrieve short periods of data which is sensitive to the shallow part of the lithosphere compared to teleseismic studies, where such short periods are attenuated due to large source to station distance.

Detailed imaging of lithospheric structure along with mapping the geometry of discontinuities within the crust, between the crust and mantle, and between the lithosphere and asthenosphere are critical for improving accurate earthquake location, understanding crustal dynamics, and assessing seismic hazard in earthquake-prone areas. To have an idea about the fundamental and higher modes resonance frequency of site, we need information of shear wave velocity and the depth of discontinuity below the site. So, in this work, we

also mapped the discontinuity beneath the Nepal Himalaya. Since, the dispersion data of surface wave are sensitive to absolute velocities (Julià et al., 2000) and autocorrelation is sensitive to the interface structure (Pham & Tkalcic, 2017), we used autocorrelation of teleseismic P wave coda to estimate the depth of interface. In our work, we implemented an improved autocorrelation technique that uses a part of earthquake seismogram after the P-wave arrivals (Pham & Tkalcic, 2017).

This manuscript contains a comprehensive summary of two projects geared towards providing a new high resolution 3-D shear wave velocity model and mapping of discontinuities of the Crust beneath Himalaya Nepal. It consists of three chapters. The second chapter is focused on the Ambient Noise Rayleigh wave 2-D group and phase tomography and 3-D shear-wave velocity structure of the crust beneath Himalaya Nepal. In the third chapter, we present the autocorrelation of teleseismic P wave coda to recover shallower and deeper crustal interface beneath the Nepal Himalaya. In this chapter, we also present the depth of interface computed from the existed velocity model across our study area and from the velocity model obtained from the Ambient Noise Tomography method.

Chapter 2: Ambient Noise Tomography

Abstract

We present a new high-resolution 3-D shear-wave velocity structure for the crust beneath the Himalaya Nepal obtained from surface-wave analysis of ambient noise data. Here, we estimate the Rayleigh wave group and phase dispersion curves by cross-correlating two years of continuous noise data recorded at 185 broadband stations from the five different temporary networks Cambridge, Hi-CLIMB, Namaste, Hi-MNT, and HiKnet. The measured dispersion curves were inverted to produce the Rayleigh wave group and phase tomography maps from 3 to 35 s period. Local dispersion curves extracted from the group and phase tomography maps were inverted using a self-parameterized Bayesian inversion scheme to obtain a 3-D shear wave velocity structure down to 60 km depth. Our results show significant differences in crustal structure within the region and correlate well with known geological and tectonic features in the study area. Pronounced low velocities observed before the Main Frontal Thrust (MFT) likely correspond to the sedimentary basin that lies in front of the MFT. A high velocity layer observed to be sandwiched between two low velocity layers at 10-15 km depth beneath Nepal and part of South Tibet may indicate the presence of a shear zone. Beneath South Nepal and under the High Himalaya, the presence of a low velocity layer at a depth of 15-25 km and 25-35 km respectively indicates the presence of aqueous fluids with high pore pressure. The low velocities in the mid-crust observed below South Tibet could indicate the presence of partial melt. We found pronounced high velocity at 40-60 km depth beneath the High Himalaya which suggests that the rocks in this region might be undergoing metamorphism to partial eclogite.

Keywords: Himalaya Nepal, Ambient Noise, Surface Wave Tomography, Bayesian Inversion, Rayleigh wave phase, and group tomography, 3-D shear wave structure

2.1 Introduction

The Nepal Himalaya is seismically active region because of its tectonic setting, and it already has witnessed many damaging earthquakes in the past. For a better understanding of the physics of earthquakes as well as their detailed high-resolution location and monitoring, an adequate 3-D regional velocity model is needed. Generally, upper-crustal complexity within a tectonic region can vary dramatically for different locations, especially for the regions like our study area where the geological conditions vary at different locations (Upreti, 1999). Regional 3-D shear wave velocity model of crust can provide the crustal complexity and the Vs profile at a specific place which is useful to compute the amplification behavior of shear wave for a given earthquake. We can understand the lithospheric density structure from the joint inversion of shear wave velocity and other geodynamic data (e.g., topography, crustal motion, earth rotation, laboratory experiments, and heat flow). Also, mapping the major discontinuities within the crust is crucial to improve seismic hazard. To map such discontinuities precisely from the autocorrelation method, we need a 3-D regional velocity model. However, the 3-D velocity structure of the crust in our study area is poorly imaged and therefore less understood although being natural laboratory.

There are few studies carried out to understand the lithospheric structure beneath the Nepal Himalaya, e.g., receiver function analysis (Nábělek et al., 2009; Schulte-Pelkum et al., 2005; Q. Xu et al., 2015), Local Earthquake Tomography (Monsalve et al., 2008), Ambient Noise Tomography (Guo et al., 2009) and joint inversion of surface wave dispersion and receiver function data (Z. J. Xu et al., 2013), but the detailed crustal structure is poorly understood. The previous studies by receiver function analysis mainly focused on the mapping of the crustal interfaces (for example, MHT, Moho, interface between upper and lower Indian crust, etc.) and the local earthquake tomography has poor lateral resolution. For a better understanding of the lithosphere, we need a high-resolution 3-D velocity model, which we can achieve through Ambient Noise Surface Wave tomography.

Previous studies have shown that cross-correlation of long time series recorded at two

stations at the same time mainly leads to the emergence of a surface wave signal propagating between the two stations (Bensen et al., 2007; Shapiro et al., 2005; Shapiro & Campillo, 2004). The resulting surface wave signal corresponds to the surface wave of the earthquake that occurred at one of the two stations and was recorded by the other, and vice versa. Therefore, the phase and group dispersion of the emerged surface wave carries the structural information about the media along the path of surface wave propagation.

The main objective of this work is to implement the phase and group dispersion of Rayleigh wave (obtained from cross correlation of ambient noise) to estimate the 3-D regional shear wave velocities in the Nepal Himalaya. The shallow crust (depth<5 km) of the Nepal Himalaya is poorly understood. To have a high-resolution image of shallow crust, we need the high frequency dispersion data, which can be achieved from the cross correlation of the station pairs having shorter inter-station distances. Since, the lateral resolution in ambient noise tomography depends on the distribution of stations across the study area, we implemented this method to improve the lateral resolution of tomographic images as well as shear wave velocity structure by using dense coverage of stations across our study area. In the past, Ambient Noise Tomography has already been successfully carried out in Central Europe (Verbeke et al., 2012), New Zealand (Lin et al., 2007), Tyrrhenian Basin (Manu-Marfo et al., 2019), Tibet (Yang et al., 2010) and so on.

In this study, we used the ambient noise recordings in the vertical component of the seismogram from five different networks and extracted the inter-station Empirical Green's functions by cross-correlation, which are further used to construct phase and group velocity maps at 3-35 s (sensitive up to 60 km depth) using the method of Yanovskaya and Ditmar (Yanovskaya & Ditmar, 1990). Finally, we obtained the 3-D shear-wave velocity and the corresponding uncertainty up to a depth of 60 km using the Bayesian self-parametric joint inversion approach (Pachhai et al., 2014).

2.2 Data and Method

We took advantage of continuous time-series data recorded by five different networks (Hi-MNT (A. Sheehan, 2001), Hi-CLIMB (Nabelek, 2002), Namaste, HiKnet (L Bollinger et al., 2011), and Cambridge) to provide a high resolution velocity structure for Nepal using ambient noise cross-correlation. The Hi-CLIMB was operated from 2002 to 2005, installed by J. Nabelek and his team, while Hi-MNT was installed from 2000 to 2002 by A. Sheehan and his team. The Namaste and Cambridge network were operated from 2015 to 2016 just after the 2015 Gorkha Earthquake. Namaste Network was operated by Orogen State University, Cambridge Network by Cambridge University, and ICTP, and HiKnet was operated by a French group from 2014 to 2016 and the data was archive by RESEIF.

We strictly did cross-correlation between the data recorded at the same time to avoid the effect of a different distribution of noise source in time scale. Since HikNet, Namaste and Cambridge networks have 2 years common operated period (2015-2016), we decided to combine these networks and produced a single tomographic image. We are the first to use more than 185 broadband stations for a small region along our study area. The distribution of these stations provides unprecedented dense ray coverage to make the ambient noise method a robust technique for studying crustal structure beneath Nepal and some parts of South Tibet.

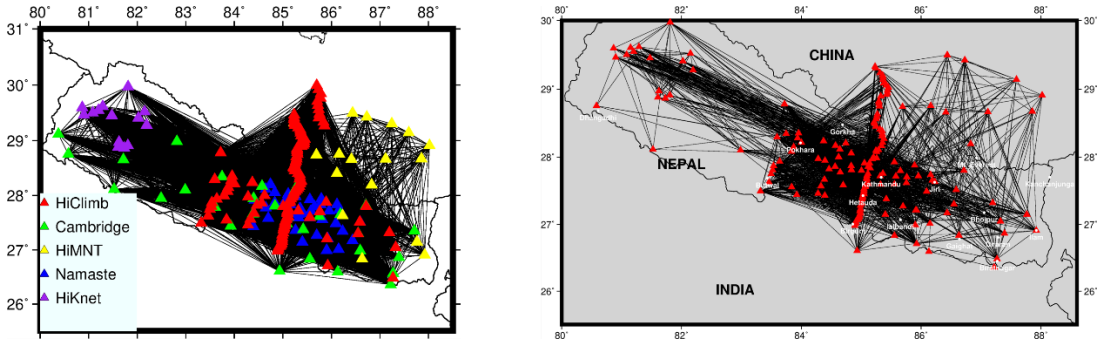

Figure 2.1: Starting ray-coverage where triangles represent the broadband stations of all the network in this study (left). Different color triangles represent the stations belonging to different network and Final ray-coverage used in this study (right).

We see nice ray-coverage in Nepal when we combine all the networks. The ray coverage in

the final phase shows a good crossing of raypaths in Central and Eastern Nepal, but Western Nepal has poor ray coverage. Such a large number of stations distributed in a small region eventually gives high-resolution results. The raypaths shown in the final ray coverage (see in Fig2.1 (right)) are those for which we were able to compute the best Elastodynamic Green's Functions, which were used in the further study. There are raypaths in Western Nepal, but they are almost parallel to each other, which ultimately reduces the resolution in Western Nepal. Thus, the results obtained from the combined network are reliable for Central and Eastern Nepal as well as for part of South Tibet. We see that some of the stations are missing in the final ray coverage which is because the data are not of good quality or data for these stations are missing. In the final ray coverage, we selected only the pairs for which we were able to pick the dispersion curve.

2.2.1 Data Processing

We followed the procedures of Bensen et al., 2007 to calculate the cross-correlation between stations. We cut the continuous waveform data to 1 hour in length and removed the mean, trend, and instrument response from the data. We then applied a bandpass filter of the 0.02-0.2 Hz frequency band and performed one-bit normalization on the filtered data to remove earthquake signals from the data. We also applied spectral whitening to emphasize the higher frequencies and finally performed cross-correlation of the whitened data for any pair of stations. The steps up to spectral whitening is called single station data preparation. The main goal of processing single station data is to remove earthquake signals and instrument irregularities from the time series data and to reduce the effect of low-frequency microseisms and broaden the available frequency band. The example of data processing is shown in figure2.2.

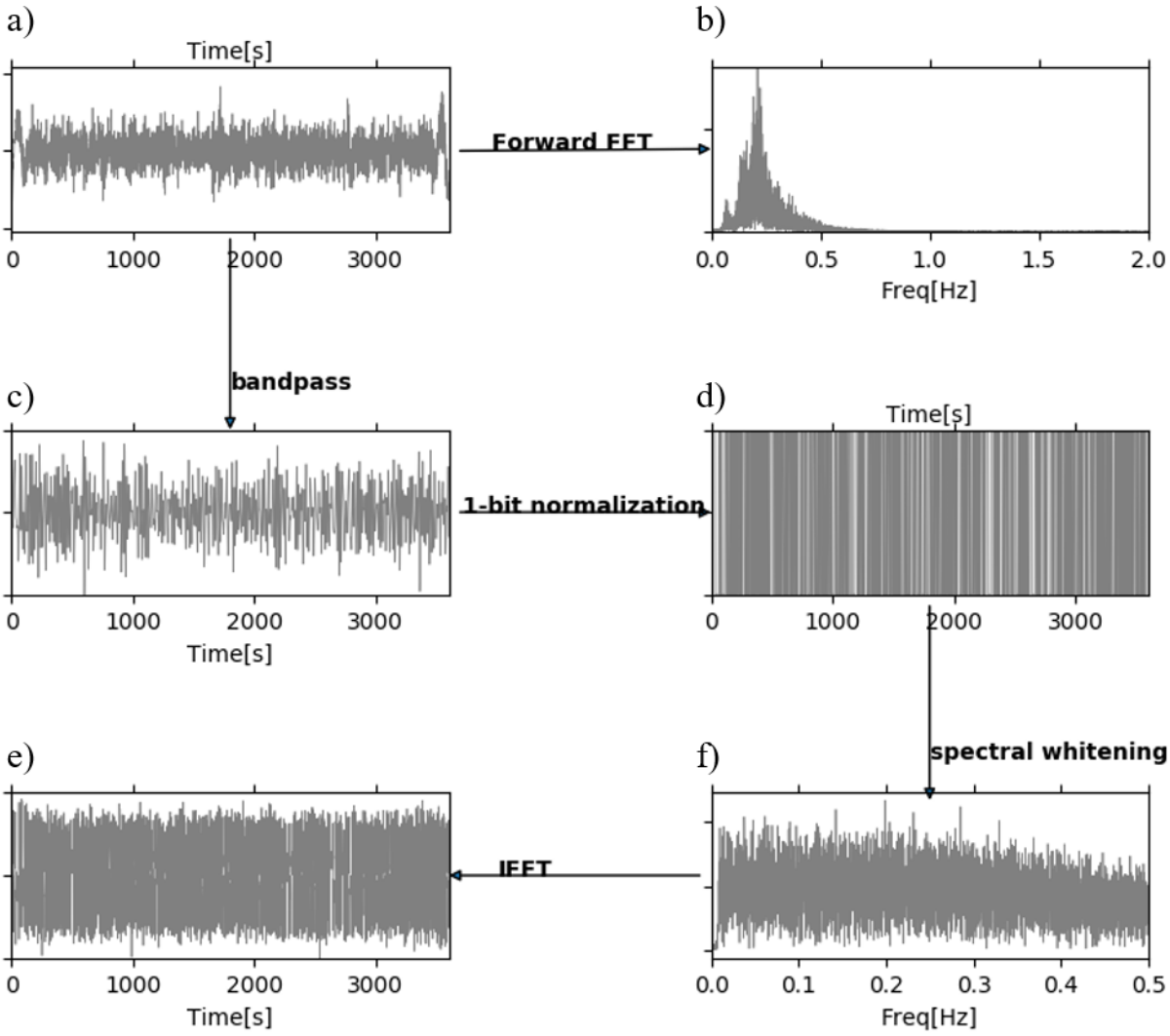

Figure 2.2: An example of data preparation for a single station. The 1-hour waveform is taken from the data recorded by the station THAK after removing the instrument response.

2.2.2 Data Selection Criteria and Methods

We performed cross-correlation between data recorded at the same time to avoid the effect of the different distribution of the noise source in the time scale. We linearly stacked all cross-correlations obtained for specific pairs of stations to improve the signal-to-noise ratio (SNR). The quality of the Rayleigh wave signal is examined using their signal-to-noise ratio (SNR), which is calculated as the ratio of the maximum amplitude of the signal and the root mean square (RMS) of the noise in the time window behind the signal window. In ambient noise cross correlation, we set minimum and maximum velocity of Rayleigh wave (in our work, we set maximum velocity as 4.4 km/s and minimum velocity as 2.0 km/s) to define the signal

window (see in Fig2.3(a)). The noise window is considered around the end of the waveform (we defined noise window around 1300 s in our work).

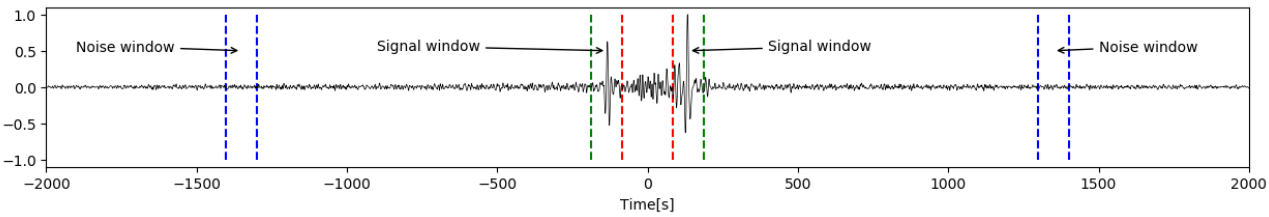

Figure2.3 (a) Stacked cross correlation (showing causal and acausal part) for station pair BIRA-SAGA. The dashed red and green vertical lines indicate the signal window while blue dashed vertical lines indicate the noise window.

The SNR serves as a proxy for estimating the uncertainties (Bensen et al., 2007; Yang & Ritzwoller, 2008) and as a criterion for selecting the best Green functions for dispersion analysis (Yang & Ritzwoller, 2008). We took the average of causal and acausal parts of the stacked cross-correlated waveform to consider the average structure only when the cross-correlation coefficient between causal and acausal parts is more than 0.40 and the SNR of both parts is greater than 10. If the cross-correlation coefficient is less than 0.40, then we took either the causal or the acausal part based on the better SNR ratio. We choose a threshold cross-correlation coefficient of 0.40 because the SNR ratio of the average of the causal and acausal parts is greater than that of the individual part. Since we performed the cross-correlation of the vertical component, the obtained stacked waveform corresponds to the Rayleigh wave originating from an earthquake occurring at one of the two stations and recorded by the other.

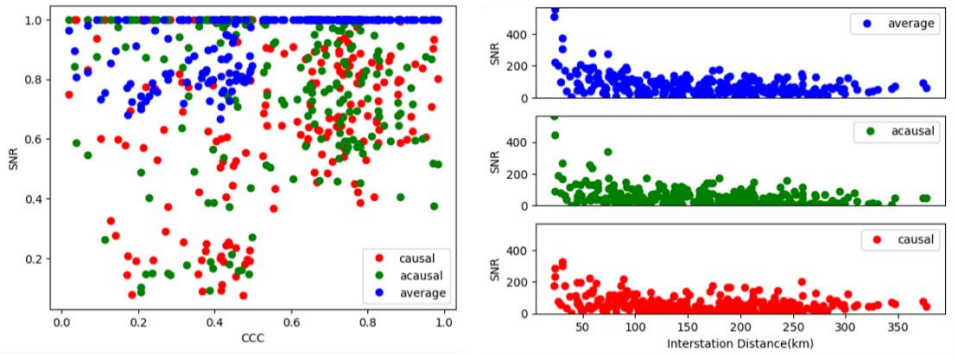

Figure 2.3: Normalized SNR of causal, acausal, and average of causal and acausal vs. cross-correlation coefficient (left) and variation of SNR of causal, acausal, and average of causal and acausal with interstation distance (right).

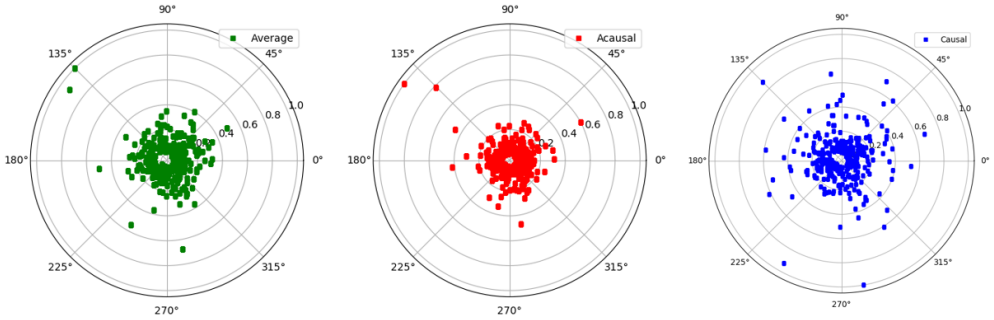

Figure 2.4: Variations of SNR with azimuth.

Polar plots of SNR vs. azimuth (Figure2.4) suggest that the noise source is nearly homogeneous since there is no azimuthal dependence. The SNR is slightly higher at 135 to 200 degrees azimuth (in the causal part), maybe this is due to the noise coming from the Bay of Bengal and the Indian Ocean is stronger than the other sides. But if we average, the SNR is almost the same everywhere. The SNR vs distance plot (see in Fig2.3) shows very nicely a 1/√distance decay of the surface wave. In the next step, we stacked the signals from all 30 days and plotted them together to see if there was a seasonal change, but we saw no effect of seasonal change in the monthly stacked cross-correlations (see in Fig2.5).

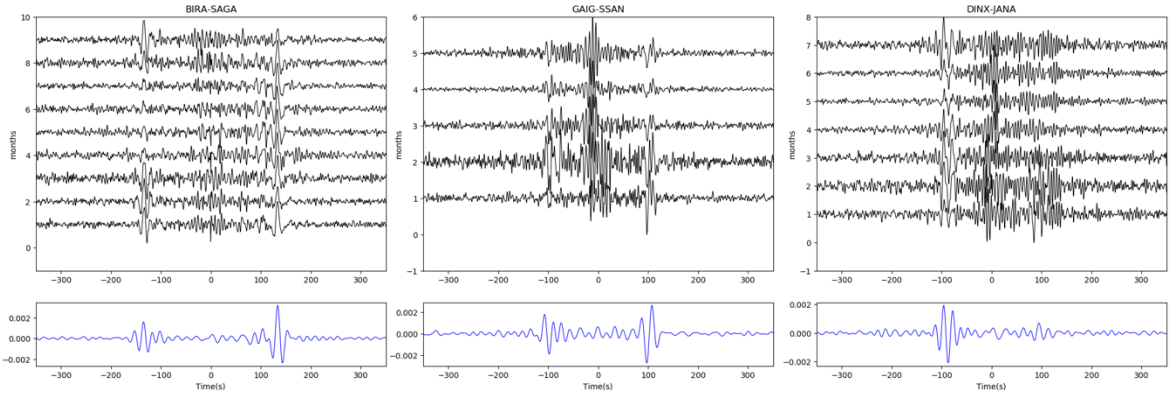

Figure 2.5: Cross-correlation stacked every 30 days (top) in black color and stacking of all data for a given pair of stations (mention above the plot) is in blue color (bottom).

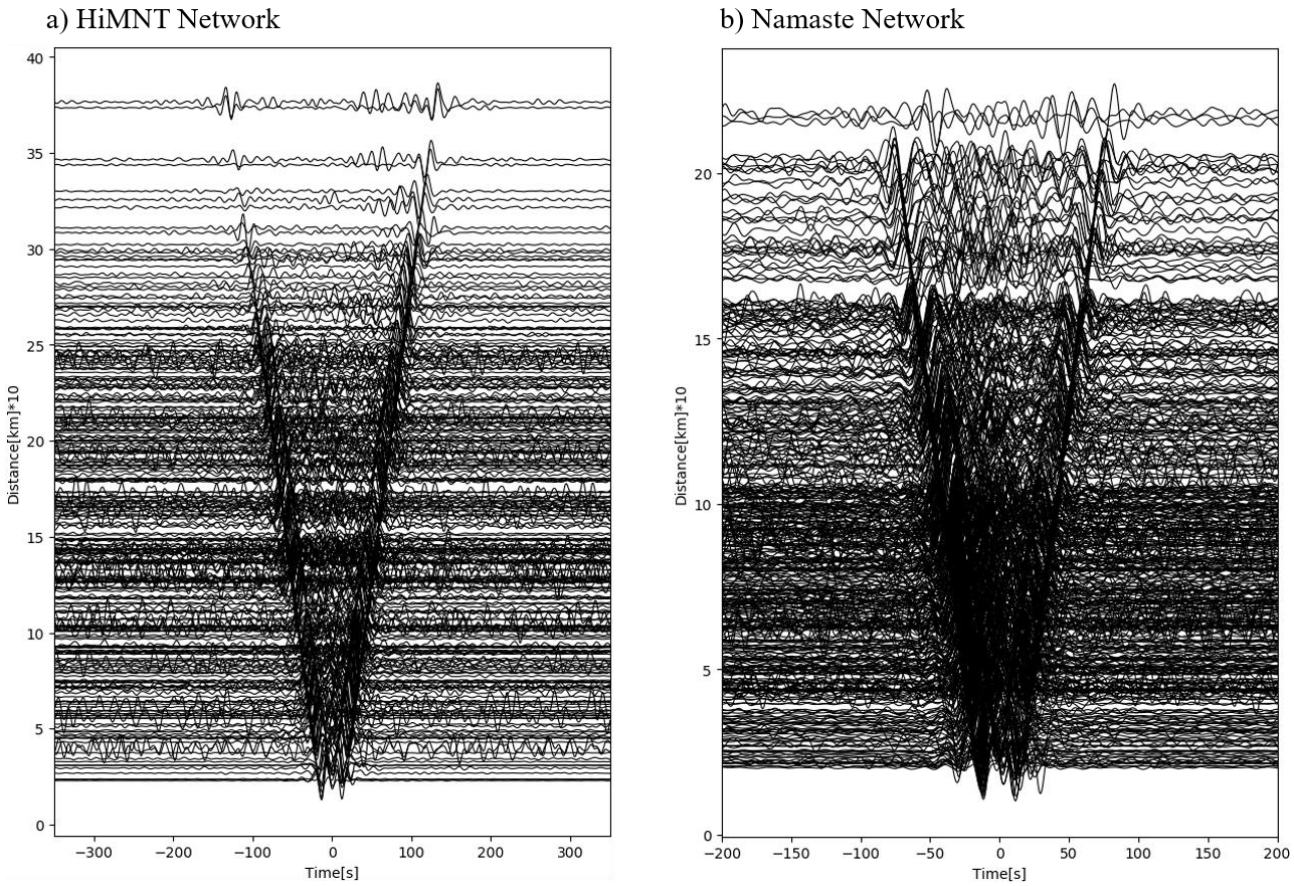

Figure 2.6: Stacked cross-correlation of all possible pairs that have at least 2 months data in common with another station in the pair, after applying a bandpass filter in the period band 10-50 s. The negative lag is called acausal and the positive lag is called causal.

Although the computation time is more expensive in the case of hourly cross-correlation than in the case of daily cross-correlation, we stick to hourly cross-correlation. The main reason is to increase the SNR of the stacked cross-correlation as we have a smaller amount of data for a common period in most of the pair of stations. The SNR of hourly stacked cross-correlation is higher than daily stacked cross correlation as we know when a greater number of waveforms are stacked, the random noise gets canceled with each other, while the signal get enhanced. We could see (see in Fig2.7) that the hourly stacked cross-correlation is much better than the daily stacked cross-correlation.

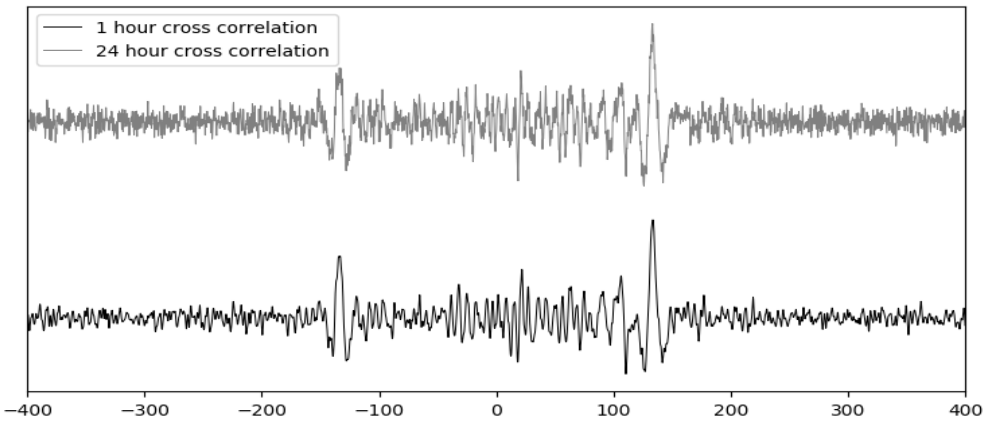

Figure 2.7: Stacked cross correlation of station pair BIRA-SAGA.

We experimented to show why we took only the causal and acausal parts when the stacked cross-correlation has a dominant signal on one side. We have shown the stacked cross-correlation that has a signal in the acausal (LAZE-SIND pair in Fig2.8 (a), (b)), causal (BIRA-MNBU pair in Fig2.8 (c), (d)) and both (BIRA-NAMC pair in Fig2.8 (e), (f)). When we have a signal in the acausal part, we compared the dispersion corresponding to the acausal part and the average. When the signal is dominant in the causal part, we compared the dispersion corresponding to the causal part and the average. If the stacked cross-correlation has a signal in both parts, the dispersion is compared for the acausal part, the causal part, and the average part. When the signal dominates in the acausal part, the dispersion corresponding to the average stacked signal appears to underestimate the group velocity at longer periods. When the signal is dominant in the causal part, the selection of the dispersion curve is easier at shorter periods. When the signal is dominant on both sides, the dispersion corresponding to the average stacked seems to be better than the individual part. This experiment motivated us to choose the dispersion curve of the average stacked when the signal is present on both sides. When the signal is dominant on one side, we chose the dispersion corresponding to the causal or acausal part.

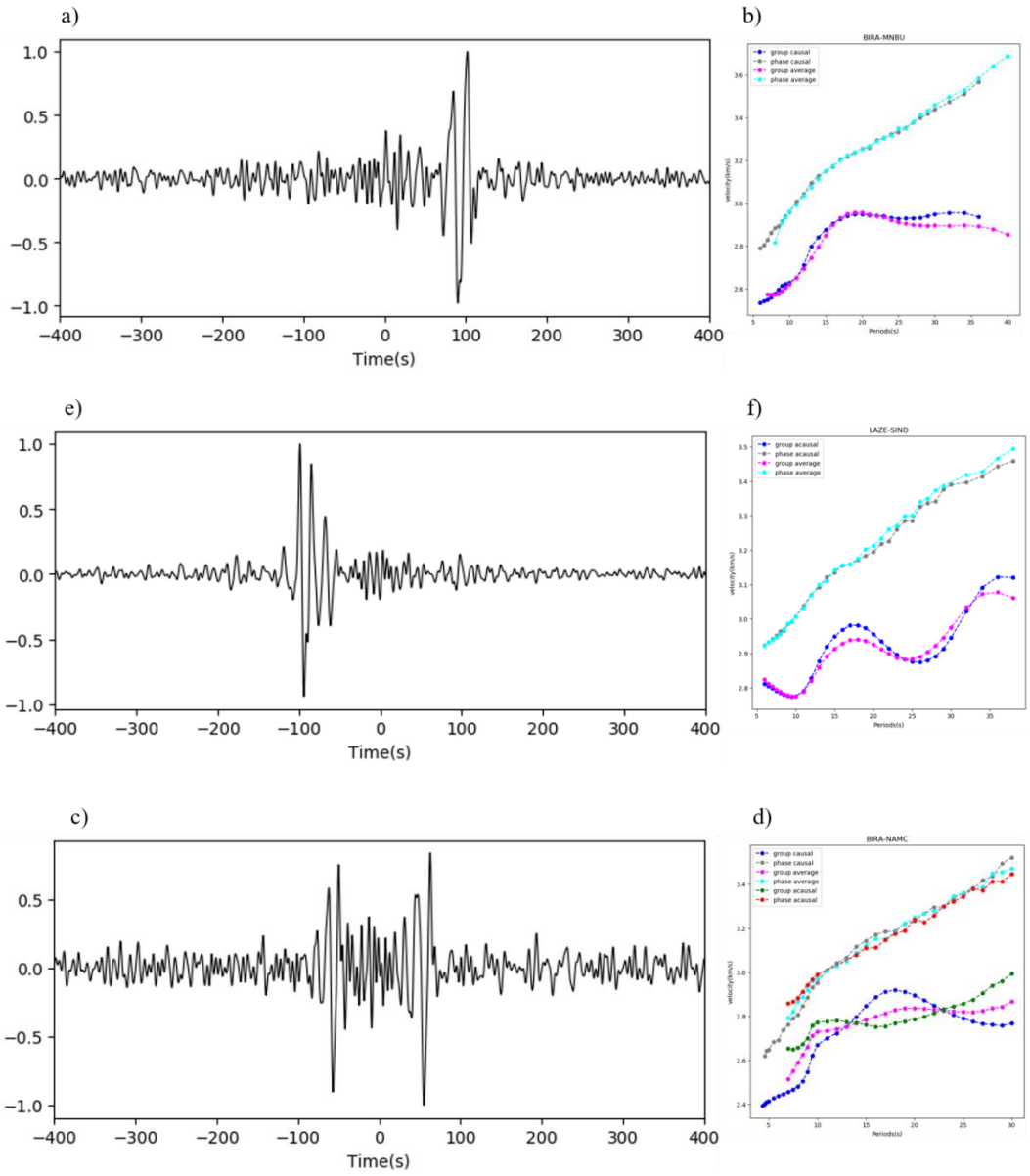

Figure 2.8: Stacked cross-correlation with causal and acausal part for three different stations pair (left). Phase and group dispersion of causal, acausal and average stacked cross-correlation (right).

As we know, the noise sources on earth are not equally distributed. Most sources of noise are near the surface of the earth. For example, industrial activities, traffic, wind, ocean waves, human activities are close to the earth's surface and these sources are the main sources of noise on earth. Such noise sources favor the fundamental mode waves much more than the higher modes. So, by cross correlating the seismic noise data, we could obtain the dispersions corresponding to the fundamental modes of the surface waves. Some examples of the phase and group dispersions of the fundamental modes are shown in figure2.9. The group and phase dispersions are determined based on

Multiple-Filter-Technique (MFT) (Herrmann, 2013). Let us consider a surface represented by an equation

$$f(t, r) = \int_{-\infty}^{\infty} F(\omega, r) e^{i\omega t} d\omega, \text{ where } F(\omega, r) = A(\omega, r) e^{-ikr+\phi}$$

Here, ϕ is source term and k is wavenumber which is the ration of angular frequency (ω) and phase velocity (c).

When we apply narrow bandpass Gaussian filter about center frequency ω_0 by the filter H(ω-ω_0), then the filtered signal is given by

$$g(t,r) = \frac{1}{2\pi} A(\omega_0)\omega_0 \sqrt{\frac{\pi}{\alpha}} exp(i\omega_0 t - k_0 r + \phi)\, exp\left(-\frac{{\omega_0}^2}{4\alpha}(t - \frac{r}{U_0})^2\right)$$

The last term on the right-hand side of the above equation represents the envelope that is maximum at the time of arrival of the group velocity. The group velocity is denoted by U and is given by the partial derivative of ω with respect to k. This equation shows that the narrowband filtered signal can be used to calculate the group velocity by using the time of the envelope maximum and the spectral amplitude A at $\omega = \omega_0$. The amplitude A is given by

$$A = \frac{2\pi}{\omega_0} \sqrt{\frac{\alpha}{\pi}}\, g\left(\frac{r}{U_0}, r\right)$$

The phase velocity is estimated from the phase term when the source term is known. The phase corresponding to the arrival of the group velocity is given by

$$\phi = tan^{-1}\left(\frac{Im\left(g\left(\frac{r}{U_0}, r\right)\right)}{Re\left(g\left(\frac{r}{U_0}, r\right)\right)}\right) = r\frac{\omega_0}{U_0} - r\frac{\omega_0}{c} + 2\pi N$$

The periodicity of the $\tan^{-1}$ function gives the N2π term. The source phase term can be eliminated in the case of the two-station technique, as in the case of cross-correlation of ambient noise where the source term is known.

The group dispersion corresponding to raypath in southern Nepal shows relatively

lower velocity than that of North Nepal and South Tibet at shorter periods, which indicates the low velocity structure at shallow depth in South Nepal. The decreasing group velocity with increasing period along the raypaths at 15-25 s indicates the presence of low velocity structure in the mid-crust.

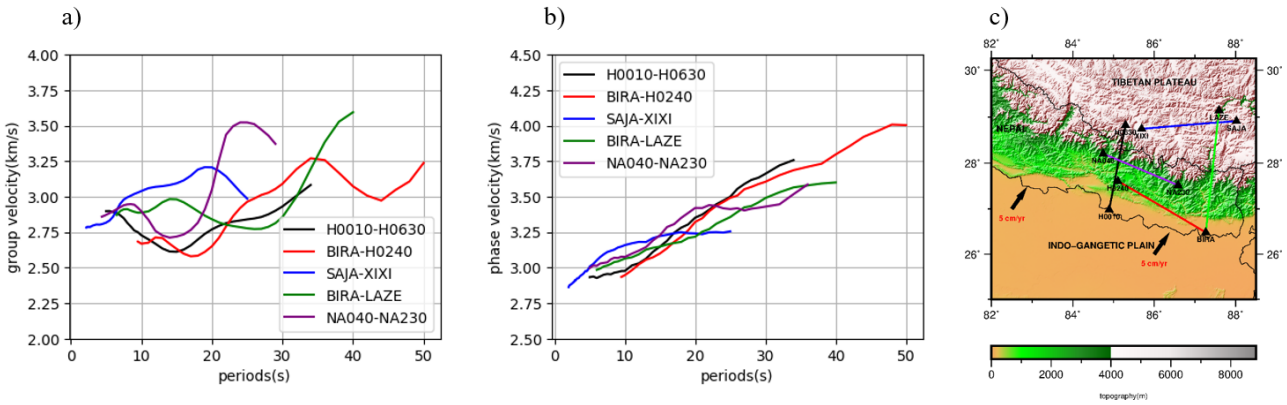

Figure 2.9: The estimated group (left) and phase (middle) dispersion curves along raypaths which are shown in right across the study area.

Multiple-Filter-Technique images of some group and phase dispersions are shown in figure2.10. All the phase and group dispersions across our study area obtained from ambient noise cross-correlations are shown in figure2.11. We observed the variations in the phase and group dispersion curve, which indicate the different velocity structure across the raypaths.

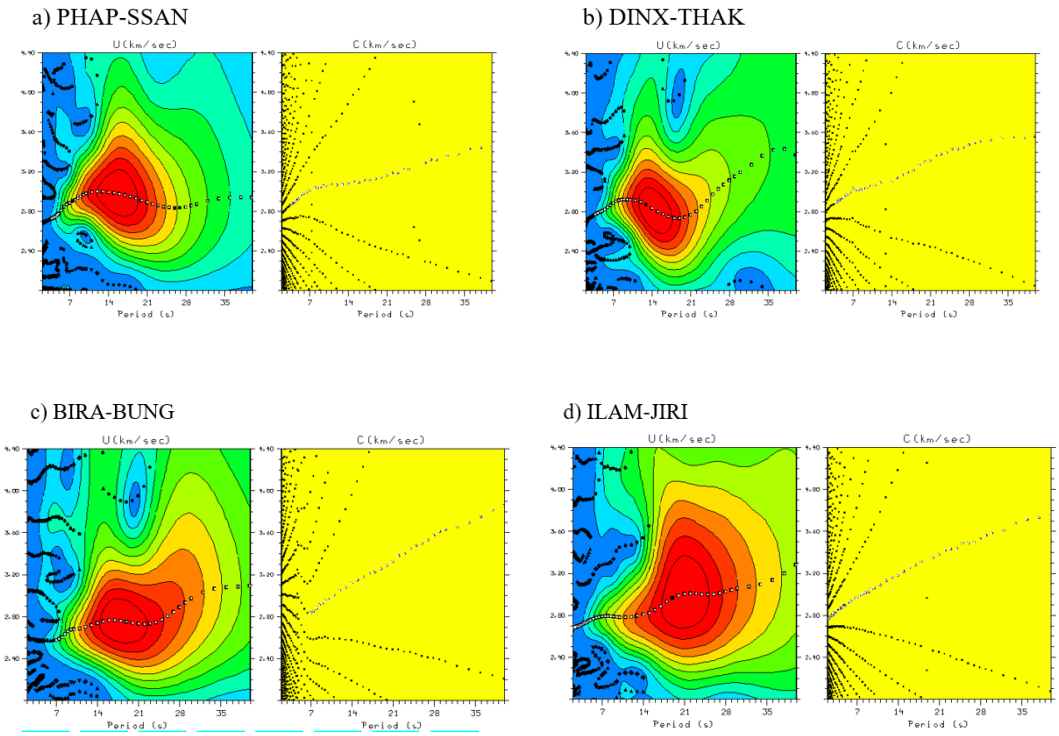

Figure 2.10: Multiple Filter Technique (MFT) image obtained for the pair of stations mentioned above in each figure.

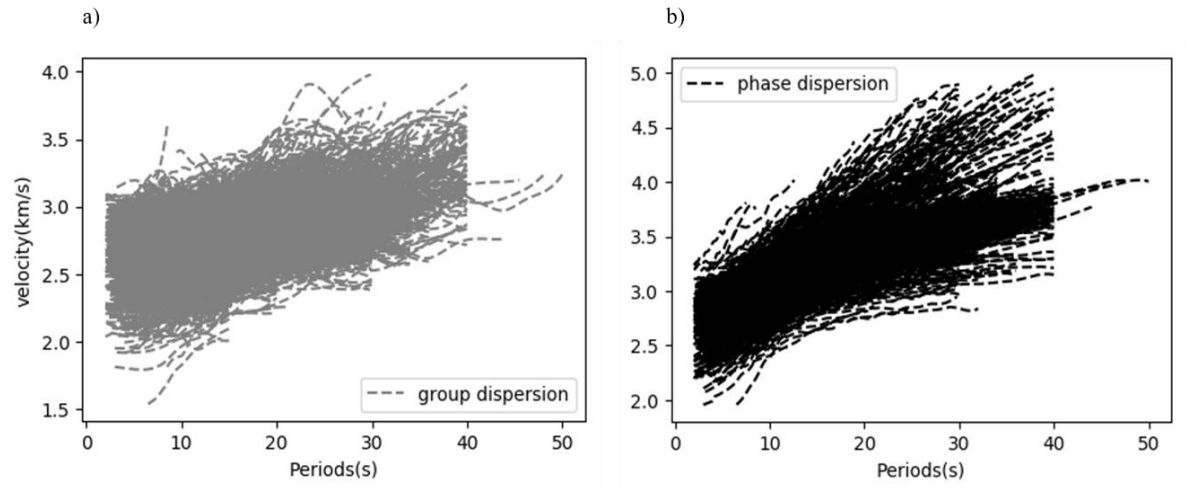

Figure2.11: (a) All group dispersions extracted with Multiple Filter Technique. (b) All phase dispersions extracted from Multiple Filter Technique.

In our work, most of the station pairs has common period less than a year, so the computation of temporal uncertainty is difficult as mentioned in Bensen et al., 2007. If the stations pair were operated for short period of time, then SNR measurement acts as proxy for uncertainties. Hence, we consider only waveforms having SNR greater or equal to 10. The dispersion curves which are shown in figure2.11 are corresponding to the waveforms having SNR>=10.

Thus, in the data processing step, we performed pre-processing of single-station data and the hourly waveforms are cross-correlated for all available station pairs and then stacked to form the EGFs. We have shown the advantage of considering hourly cross-correlation over daily cross-correlation. We computed monthly stacked cross-correlation to see the effect of seasonal change and polar plot to see azimuthal dependence. The quality of the Rayleigh wave signal that emerges after cross-correlation and stacking is evaluated based on their signal-to-noise ratio (SNR). In the final step, we analyze the EGFs using the multiple filter technique (Herrmann, 2013) to measure the Rayleigh wave fundamental mode group and phase velocity dispersions from 3 to 35 s period.

2.2.3 Rayleigh wave tomographic inversion

To estimate the shear wave velocity structure from the ambient noise cross-correlation method, there are two steps of inversion. First, the group and phase dispersions obtained along all possible station pairs are inverted to obtain the group and phase tomography maps at different period (sensitive to different depths) and from these tomographic maps, we extracted local group and phase dispersions. The dispersion of surface waves indicates the changes of elastic properties of the material with depth. Therefore, measurements of surface wave phase and group velocities at different periods can be used to constrain the depth-dependent model of the underlying media. In the second step, we invert the local phase and group dispersions jointly to estimate the 1-D shear wave velocity.

We have used the surface wave tomographic method of Yanovskaya and Ditmar, 1990 to obtain the local group and phase dispersions from Rayleigh wave dispersions extracted from the ambient noise cross-correlation. The surface wave tomographic method is a 2-D generalization of the classical 1-D method proposed by Backus and Gilbert in 1968 (Backus & Gilbert, 1968) and based on the geometric ray approximation. This approximation assumes that the travel time of the surface wave depends only on the media along the great circle path of the surface wave propagation. The main advantage of this tomographic method is that it does not require any apriori parameterization of the basis functions. This is because the damping factor controls the smoothness of the solution such that the results obtained are within the range defined by the observed dispersion curve. Moreover, the residuals of the final travel times are assumed to be randomly distributed (Yanovskaya et al., 1998). In the first step of tomographic inversion, we should choose the appropriate grid size for our study region. In this work, we decided the suitable grid size from checkboard test.

2.2.3.1 Checkerboard test:

To assess lateral resolution, one of the most reliable methods is the checkerboard test. Based on the ray coverage of each period, we calculated the optimum value of damping and smoothing parameters. We estimated the optimum damping value by minimizing the residual and model variance, while the optimum smoothing value was obtained by minimizing the model roughness and residual variance. We carried out the checkerboard test by using the optimum damping and smoothing parameters for each period by dividing the region of interest into an equal grid of size $0.30^0 \times 0.30^0$.

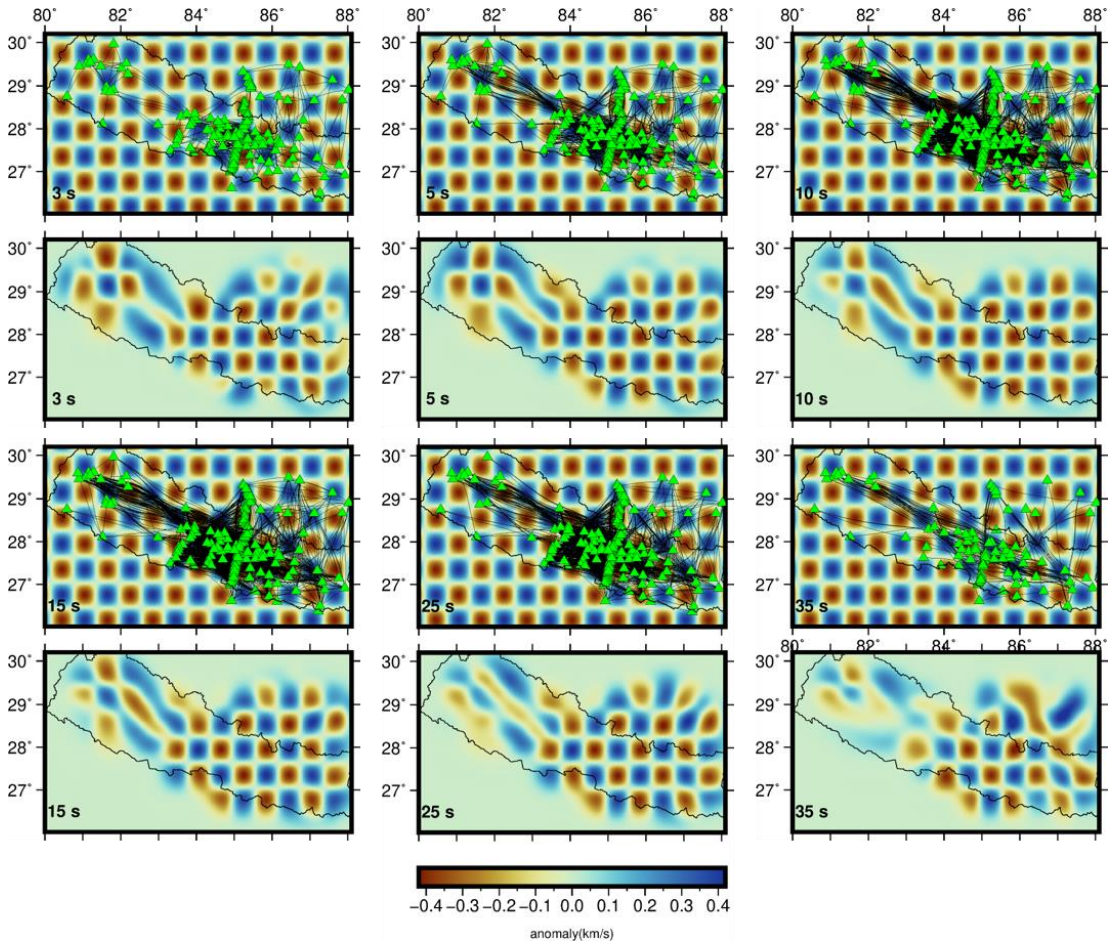

Figure 2.12: Checkerboard test of periods 3-35 s. First and third row shows the initial checkerboard with the ray-coverage of periods mention in the bottom left corner of each plot. Second and fourth row shows the recovered anomaly size of $0.60^0 \times 0.60^0$.

The ray coverage is different for each period, so the resolution is also different for each period. The better the ray coverage, the higher the resolution. We started with a checkerboard with some background velocity (average of the measured group

velocities at each period) having a standard deviation of 0.80 for a grid of size $0.30^0 \times 0.30^0$ and inverted the travel time along each ray path by using the FMST method (Rawlinson et al., 2001). We can see that anomaly of size $0.60^0 \times 0.60^0$ is well recovered for grid of size $0.30^0 \times 0.30^0$ under the coverage of the dense raypaths of the respective periods. We can see a strong smearing artifact for all the periods when the density of raypaths is very low. Central Nepal is well resolved with a grid of size $0.30^0 \times 0.30^0$ as shown in figure2.12. Once we have combined all the networks, we can resolve some of the grids even for the periods 3 s and 35 s that were missing in the individual network. This is one of the advantages of combining different networks.

In our work, we performed the checkerboard test for different grid sizes (for example, $0.15^0 \times 0.15^0$, $0.30^0 \times 0.30^0$, size $0.60^0 \times 0.60^0$, etc.) and found that the grid size of $0.30^0 \times 0.30^0$ is best for our data in each period. After setting the grid size, another important parameter to set before inversion is the damping factor.

2.2.3.2 Selection of damping parameter

We know that the smoothness of the solution increases when we increase the damping factor, but at the same time, the misfit of the data also increases. So, we need to choose a damping parameter that minimizes the data misfit and the smoothness of the solution at the same time. In our work, we executed the surface wave tomography inversion with a damping factor in the range of 0.01- 1.0 (as shown in Fig2.13) and found that 0.20 is suitable for our data across our study area.

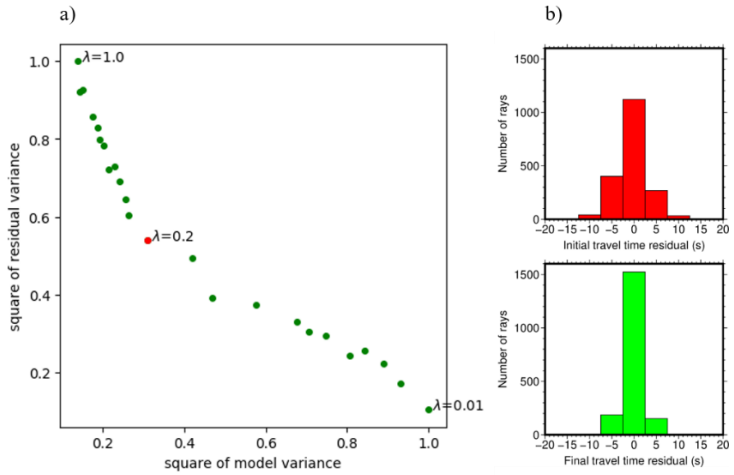

Figure 2.13: Plot of square of model variance vs square of residual variance (left) for damping factor from 0.01 to 1.0 at period 15 s. Data are normalized by its maximum in both axes. The red circle indicates the damping factor used in this study. Distribution of initial and final travel time residuals (right) at period 15 s. The plots are obtained from surface wave tomographic method developed by (*Yanovskaya & Ditmar, 1990*).

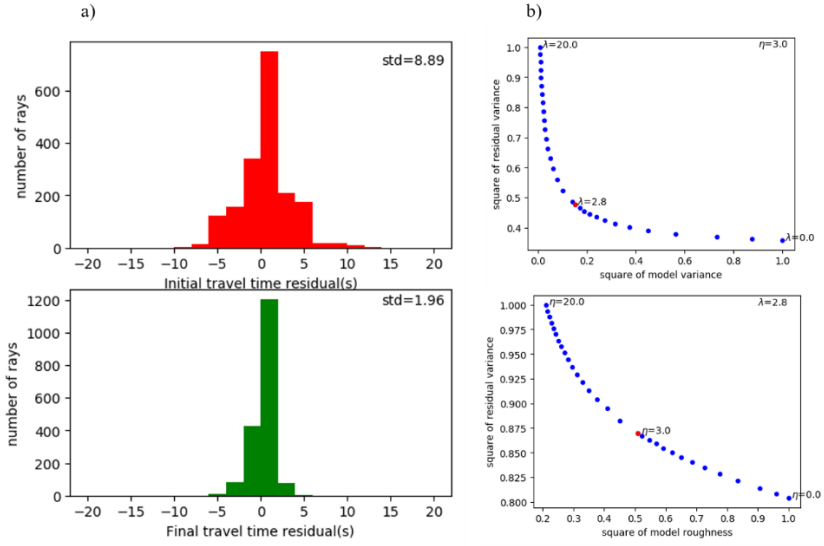

Figure 2.14: Distribution of initial and final travel time residuals at period 15 s for damping factor 2.8 and smoothing factor 3.0 (left). The plots are obtained from Fast Marching Surface wave Tomography (FMST) method developed by (Rawlinson et al., 2001). Plot of square of model variance vs square of residual variance for damping factor from 0 to 20 at period 15 s for fixed smoothing factor 3.0 (top right). Data are normalized by its maximum in both axes. The red circle indicates the damping factor used in this study. Plot of square of model roughness vs square of residual variance for smoothing factor from 0 to 20 at period 15 s for fixed damping factor 2.80 (bottom left).

To increase the reliability of the inversion result from the surface wave tomography

method (Yanovskaya & Ditmar, 1990), we also applied the Fast Marching Surface wave tomography method (FMST) developed by N. Rawlinson (Rawlinson et al., 2001) to obtain a 2-D tomography map.

We chose a period of 15 s for which the ray coverage is dense and calculated the optimum damping and smoothing factor. We should get a smooth model which is not far from the initial model and satisfies the data. So, we calculated the smoothing factor which minimizes the model roughness and data variance simultaneously, and the damping factor which minimizes the model variance and data variance simultaneously.

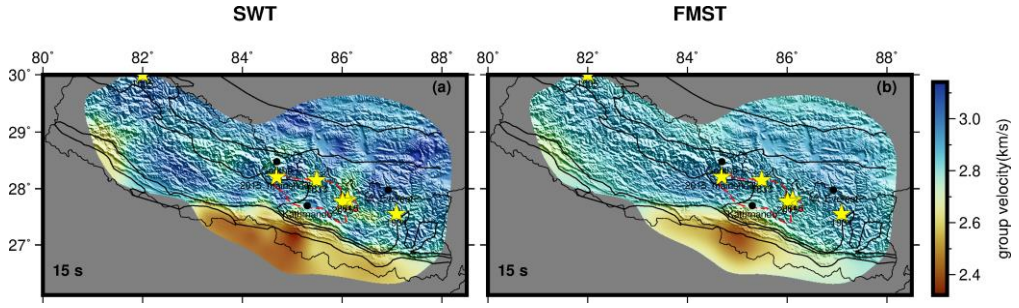

Figure 2.15: 2-D group tomography images at 15s obtained from Surface wave tomography method (left) and FMST method (right). The yellow stars represent the historical earthquake of magnitude greater than 7.0 across our study area.

2.2.4 Shear wave velocity inversion

We extracted the phase and group dispersion at each node of grids of size $0.30^0 \times 0.30^0$ over our study area (Fig2.16 (b)). The extracted group and phase dispersions are called local dispersion and are shown in (Fig2.16(c), (d)). After obtaining local dispersions, we jointly inverted them to obtain a 1-D shear wave velocity-depth profile at each node.

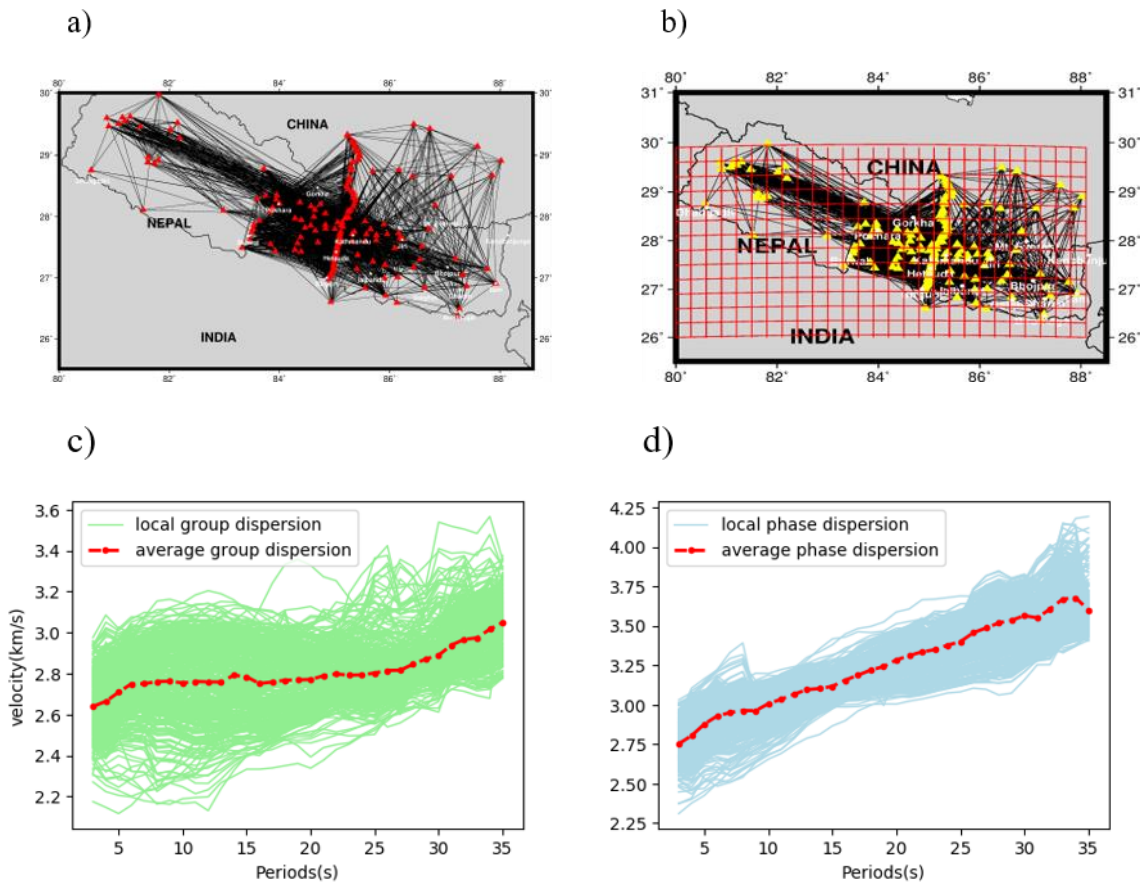

Figure 2.16: a) ray paths for which estimated group and phase dispersions are available. (b) Grids of size $0.30^0 \times 0.30^0$ superimposed over the ray paths in our study area. (c) Local group dispersion and (d) local phase dispersion obtained from the SWT method.

We know that estimating shear wave velocity from local propagation data is a nonlinear inverse geophysical problem. Most geophysical inverse problem are linearized and require a damping parameter to stabilize the inversion process (Herrmann, 2013). Hence, the proper estimation of the uncertainties is challenging job in the case of linear inversion. To overcome the shortcomings of the linear inversion approach, here we use a fully nonlinear Bayesian approach (Dettmer & Dosso, 2012; Pachhai et al., 2014; Pachhai et al., 2015) that does not require damping to compute the 1-D shear wave velocity profiles and the corresponding uncertainties. The parameter uncertainties can come from either measurement errors (i.e., errors in dispersion data obtained from frequency-time analysis) or theoretical errors (i.e., errors resulting from approximation in the model including seismic wave propagation, simplifications in model

parameterization, assumptions in data processing, etc.).

The answer to the inverse problem is expressed in terms of the posterior probability density (PPD) in Bayesian inversion. The information which we know beforehand about the model is termed as prior information and is independent of the data. Bayesian inversion combines prior information and the likelihood (involves the data information), i.e., $p(m|d) \propto p(d|m)\, p(m)$. Here, (m|d) indicates the probability of the model parameter vector (m) for a given data vector (d) (i.e., the posterior probability density), p(d|m) represents the probability of the data for a given model (i.e., likelihood), and p(m) refers to the prior probability of the model parameters (i.e., the number of layers, the layer thickness, and the S-velocity). The data errors are generally unknown quantity and are estimated as the difference between the measured and predicted data. The input reference model includes S-wave velocity and fixed V_p/V_s ratio for different depths, the P-wave velocity is derived from the fixed V_p/V_s ratio, and the density is derived from the P-wave velocity. An uniform prior within a range of reasonable S-wave velocities (based on previous studies (Monsalve et al., 2006; Pandey et al., 1995; Z. J. Xu et al., 2013)) is considered as a function of depth in this work, while the likelihood function is derived based on a Gaussian distribution of data errors.

It is challenging to compute the posterior analytically, especially in the presence of nonlinear inversion. Moreover, the model complexity (i.e., the number of layers in the case of observational data) is not known in advance, and the estimated parameter uncertainties may depend strongly on the model complexity. For example, if we increase the number of layers (i.e., model complexity), the fit between the model prediction and the observed data can be enhanced, but this might not necessarily require by the data and can result unrealistically large uncertainties. On the otherhand, a simple model can fit only a portion of the data, resulting unrealistically small uncertainties. Hence, a parameter sampling approach known as reversible Jump Markov Chain Monte Carlo (rjMcMC) sampling is used to estimate the PPD (Dettmer

& Dosso, 2012; Pachhai et al., 2015).

In the rjMcMC approach, we can change the number of layers (between 1 and 35 from the surface to 70 km depth, below which we define the half-space in this work) and in each iteration the parameters are updated by three different moves: birth, death, and perturbation. A new interface with perturbation of the velocity is introduced at random depth in the birth move. The proposed model in birth move is examined (accepted or rejected) based on the likelihood ratio of the current model to the previous model. The model is updated with additional layer and proceeds to the next iteration if the proposed model is accepted, otherwise, the current model is retained, and a new model has been proposed again. In death move, a random layer is selected and subject to delete (death) with the perturbation of layer thickness and velocity from a randomly selected layer. Then the same procedure as in the case of the birth phase is carried out. In the perturbation move, the number of layers remains the same and only the layer properties (layer thickness and velocity) are permitted to change. The sampling approach, especially rjMcMC, can be very inefficient if low probability regions separate several high probability regions. As a result, the sampling needs a long time to converge to the true model. Thus, interacting Markov chains are used here to achieve faster convergence.

2.2.4.1 Synthetic Experiment

We compared the inversion results of the group, phase, and joint inversion. The purpose of this experiment is to see whether the joint inversion recovers the structure better than the individual phase and group inversion or not. To do this experiment, we computed a synthetic phase and group dispersion for a defined initial model (represented by the solid blue line in (Fig2.17 (b))) and added 2 % of correlated noise to make the dispersion data more realistic. We then inverted the group dispersion data and phase dispersion data separately, and both together using a self-parameterized, fully nonlinear Bayesian approach.

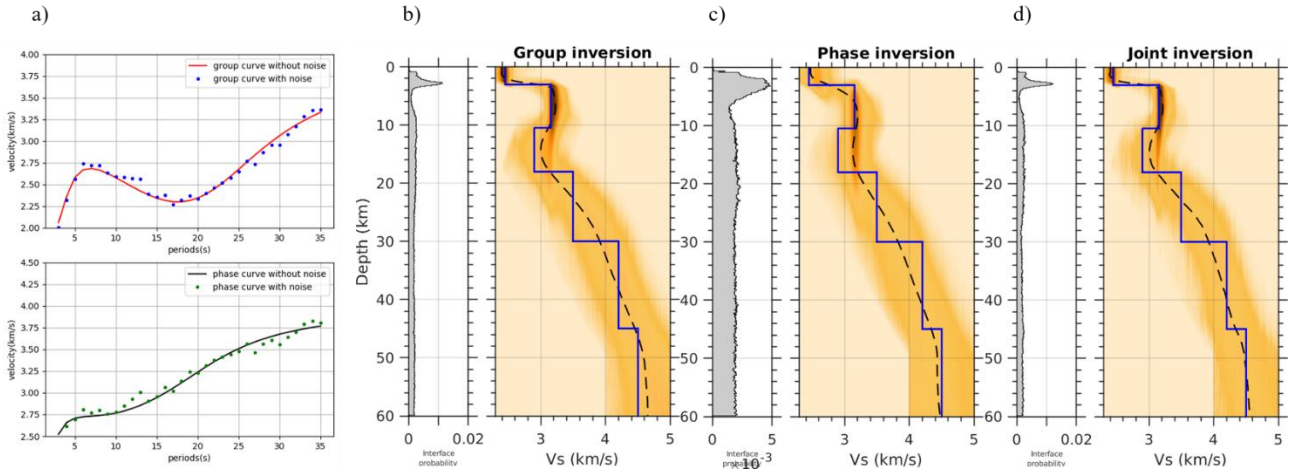

Figure 2.17: a) Synthetic group and phase dispersion data corresponding to the velocity model, represented by the blue solid line. The blue and green solid circles are the group dispersion data and phase dispersion data after adding 2 % of correlated noise to the synthetic dispersion data. b,c,d) The posterior probability for the position of discontinuities and Posterior Probability Density (PPD) for the shear velocity as a function of depth. The black dashed line represents the velocity model obtained from the joint inversion of phase and group dispersion data.

Group inversion recovered shallow structure better than phase inversion, while phase inversion recovered deeper structure better than group inversion. This is expected since the group velocity is more sensitive to the shallow structure than the phase velocity, which can be seen in the sensitivity kernel plot (Fig2.25). The shallow, as well as the deeper structure, are recovered well in the case of joint inversion, which motivates us to execute joint inversion in our work.

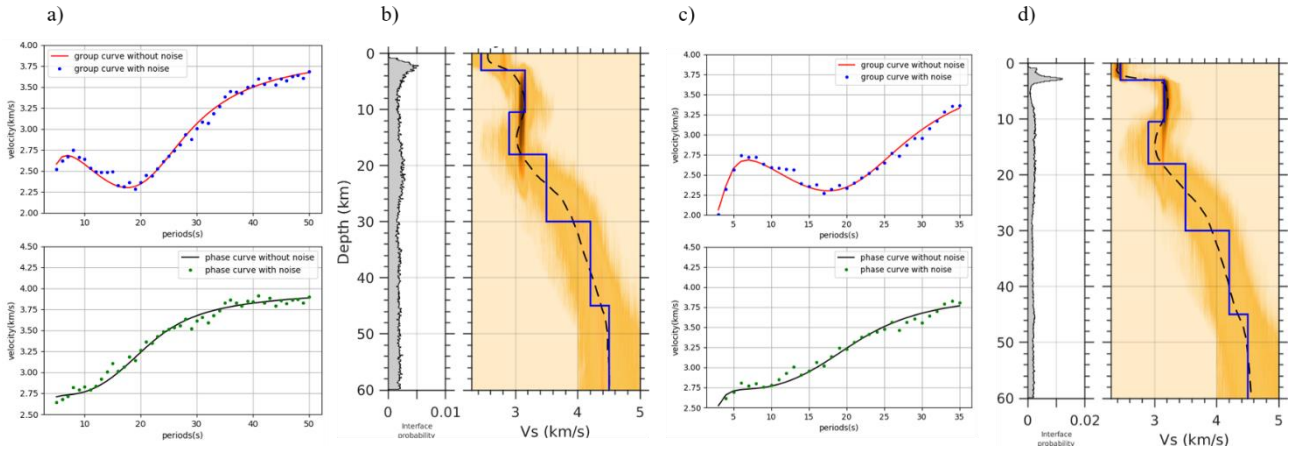

Figure 2.18: (a), (c) Synthetic group and phase dispersion data corresponding to the velocity model, represented by the blue solid line in (b) and (c), respectively. The blue and green solid circles are the group dispersion data and the phase dispersion data after adding 2 % of correlated noise to the synthetic dispersion data. b), d) The

posterior probability for the position of the discontinuities and Posterior Probability Density (PPD) for the shear velocity as a function of depth. The black dashed line represents the velocity model obtained from the joint inversion of phase and group dispersion data.

We accomplished various synthetic experiments to test the resolution capabilities of the transdimensional Bayesian inversion for the dispersion data from 3 to 35 s. We performed the synthetic experiments to compare the shallow structure recovered with the dispersion data with periods less than 5 s and periods greater than or equal to 5 s, and the deeper structure recovered with the dispersion data with periods greater than 35 s and periods less than or equal to 35 s. The motive behind this synthetic experiment is to see the advantage of lower periods to recover shallower structures, and to see that the recovered deeper structure (up to 60 km) is affected when the dispersion data have no periods greater than 35 s. We focused on 3 to 35 s in the synthetic test because we have dispersion data from 3 s to 35 s in our real data. To perform the synthetic experiment, we created the synthetic Rayleigh wave group and phase dispersion for different velocity structures with different Moho depths and variable crustal complexity.

The experiment (Fig2.18) shows that transdimensional Bayesian inversion is sensitive to the shallow structure given the narrow distribution of velocities from the ensemble models, and uncertainties increase as a function of depth. The velocity ensembles are plotted with orange color, and we could see the dark orange color down to a depth of 10 km in both experiments. The inversion is not able to constrain the shallow velocity structure (at a depth of 3 km) when the dispersion data have no periods less than 5 s, but it is reasonably constrained when the dispersion data have a minimum period of 3 s. The low velocity structure at a depth of 10.5 km is recovered to some extent in both cases. The structure below 40 km is recovered well by inversion of dispersion data with periods greater than 35 s, but the recovered model is close to the true model even when dispersion data with periods less than or equal to 35 s are inversed. This experiment gives us the reliability of the inversion model up to a depth of 60 km, which

is also confirmed by the sensitivity kernel map. Since the minimum period in our work is 3 s, we can image shallow velocity structures with high resolution.

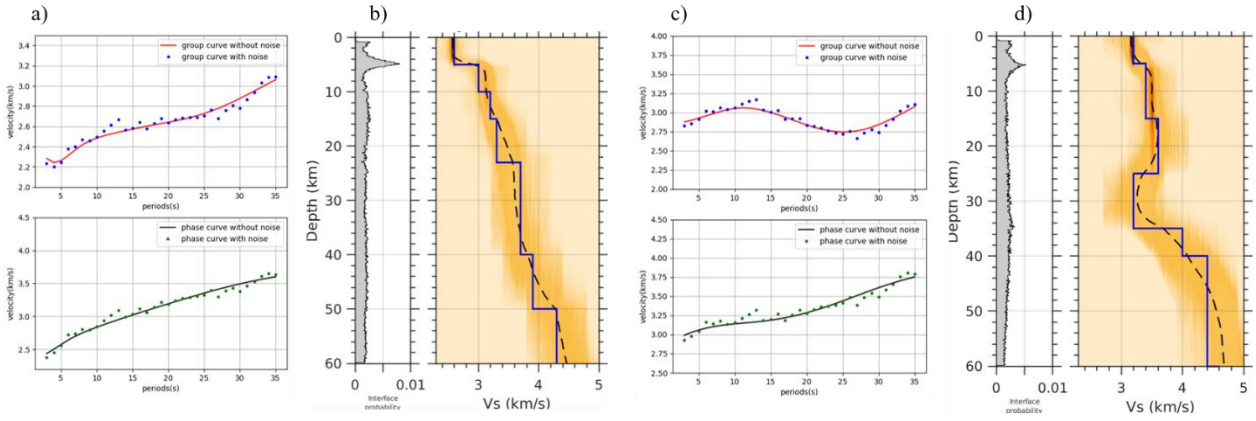

Figure 2.19: (a), (c) Synthetic group and phase dispersion data corresponding to the velocity model, represented by the blue solid line in (b) and (c), respectively. The blue and green solid circles are the group dispersion data and phase dispersion data after adding 2 % of correlated noise to the synthetic dispersion data. (b), (d) the posterior probability for the position of the discontinuities and Posterior Probability Density (PPD) for the shear velocity as a function of depth. The black dashed line represents the velocity model obtained from the joint inversion of phase and group dispersion data.

We performed another synthetic experiment (Fig2.19) to see the performance of the transdimensional Bayesian inversion approach when the velocity simply increases with depth. This time we did not include a low velocity structure in our initial model. We also created a velocity model that includes a 10 km thick low velocity structure in the mid-crust (at 25 km depth). The synthetic phase and group dispersion data for both models are inverted jointly. We could observe that inverted velocity model is close to the initial model and the low velocity at 25 km depth is recovered well in the inversion.

2.3 Results

In general, short periods Rayleigh wave phase and group velocities, in this study 3-10 s, are sensitive to shear-wave velocity structure of the upper crust. At short periods, lateral velocity anomalies are mainly attributed to velocity differences between sediments and the surrounding dense crystalline rocks. Generally, low velocity anomaly corresponds with sediment as shear wave velocity is directly proportional to

the modulus of rigidity (how much rock is compressed) and sediments are usually less compressed, while the high velocity anomaly is associated with dense crystalline rocks since crystalline rocks have high level of compression. In our study area, the Rayleigh wave of 15-25 s group and phase velocity is sensitive to the shear-wave velocity structure of the mid-crust (up to 30 km). Our results show that Rayleigh wave group and phase velocity between 25 to 35 s periods are sensitive to lower crust and uppermost mantle shear velocity structure in Nepal. We observed that Rayleigh wave phase and group velocity between 25 to 35 s periods are predominantly sensitive to lower crust in South Tibet.

2.3.1 Model resolution

We evaluate the lateral resolution of our velocity model from Yanovskaya and Ditmar method which is mainly determined by ray-coverage, damping, and the smoothing parameters applied during the inversion (Yanovskaya & Ditmar, 1990). The lateral resolution in our work is estimated by considering the mean size of an averaging area. The mean size is given by $[S_{min}(x,y) + S_{max}(x,y)]/2$, where, $S_{min}(x,y)$ and $S_{max}(x,y)$ are semi-minor and -major axes of an ellipse of surface defined by S(x,y) in 2-D cartesian coordinates (Yanovskaya et al., 1998).

The information obtained with this method is not different from that obtained with the checkerboard test. We observe the best resolution in the region where we have dense ray coverage. The resolution map up to 120 km is shown in figure2.20. We see that the lateral resolution changes with periods, which is due to the variation of the density of the raypaths and the azimuthal coverage from the cross-correlation. From the resolution map, it can be seen that the laterally resolvable structure is of the order of 30 km in Central and Eastern Nepal for the period range of 3-30 s and decreases to 100 km at period 35 s. At period 35 s, the lateral resolution of 50 km around Central and part of Eastern Nepal can be seen. For most periods, Central and Eastern Nepal and part of Southern Tibet is highly resolved due to the good crossing of raypaths and a large number of stations.

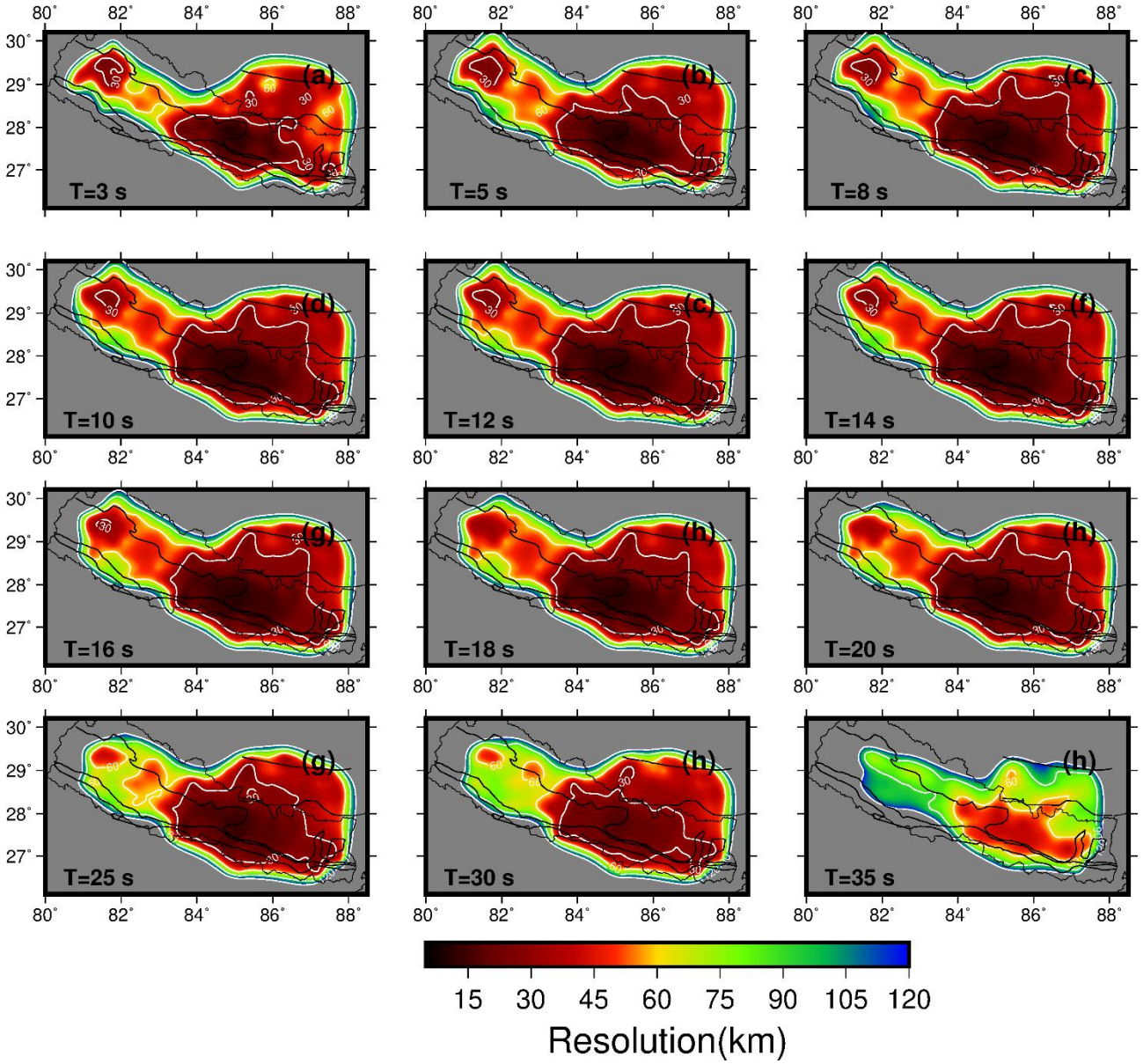

Figure 2.20: The estimated resolution map of periods (3-35 s) obtained from the surface wave tomography method. Periods are mentioned in the bottom left corner of each plot.

2.3.2 Group Tomography

2.3.2.1 Group Tomography of individual network

We used data from five different networks (HiMnt, HiClimb, Namaste, HiKnet and Cambridge) which were operated at different period of time. We strictly did cross-correlation between the data recorded at same time to avoid the effect of different distribution of noise source in time scale. Since HiKnet, Namaste and Cambridge

networks have 2 years common operated period (2015-2016), we decided to combine these networks and produced a single tomographic image. In this way, we produced three different tomographic images, two of them came from HiMnt, HiClimb and one came by combining Namaste, HiKnet, Cambridge networks.

We have found there are common regions where the ray-coverage of all these networks present. Our final objective is to combine all of these networks and produce tomographic images. Before combining them, it is better to see the group and phase velocity solution at common region coming from all these networks. So, here we are presenting the comparison of group velocity images at particular period.

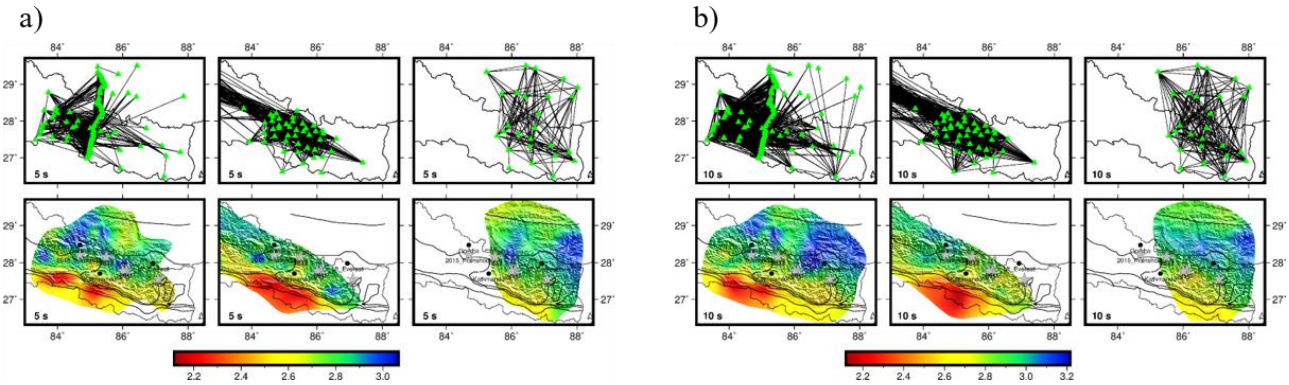

Figure2.21: a) Absolute group velocity images at 5 s and b) at 10s coming from HiClimb (1st column), Namaste, HiKnet, Cambridge (2nd column), HiMnt (3rd column). First row is ray-coverage at each period and second row is absolute group velocity images.

In group tomographic images (see in Fig2.21 and 2.22), we can see HiMnt covered Eastern and Southern Tibet while HiClimb covered Central Nepal as well as some part of Southern Tibet and Eastern Nepal. Namaste, HiKnet, Cambridge covered some part of Eastern Nepal and covered almost all part of Central Nepal. We presented tomographic images between longitude 83^0E and 88^0E with same color palate. At 5 s, the low velocity observed in South of Central Nepal is well compared in HiClimb, Namaste, HiKnet, Cambridge and Combined Network while Southern Eastern Nepal is well compared in HiMnt, HiClimb, Namaste, HiKnet, Cambridge and Combined Network. The region between MBT and STD is well compared where the ray-coverage

is present. The relatively high velocity is observed around Gorkha in HiClimb which is present also in Namaste, HiKnet, and Cambridge. We observed relatively high velocity between IYS and STD in HiMnt Network. At 10 s (see in Fig2.21 (b)), we could see small difference between HiClimb and HiMnt in the region between IYS and STD. This might be the consequence of the density of ray-coverage at that place. We could see dense ray-coverage in the case HiMnt while the HiClimb has poor ray-coverage.

At 15 s (see in Fig2.22 (a)), the ray-coverage is poor in South Tibet when we consider only HiClimb network while the HiMnt network shows a good raycoverage in that region. The solution in individual network under the raycoverage are comparable in the common region. At 20 s, 25 s, and 30 s (see in Fig2.22 (b), (c), and (d)), there are poor raycoverage at Eastern Nepal when we consider only HiClimb network. There is less crossing of raypaths in the case of Namaste, HiKnet and Cambridge. At 20 s, we observed the high velocity around the epicenter of 2015 Gorkha earthquake in HiClimb as well as Namaste, HiKnet and Cambridge. At 30 s, there is high velocity around Kathmandu in all networks.

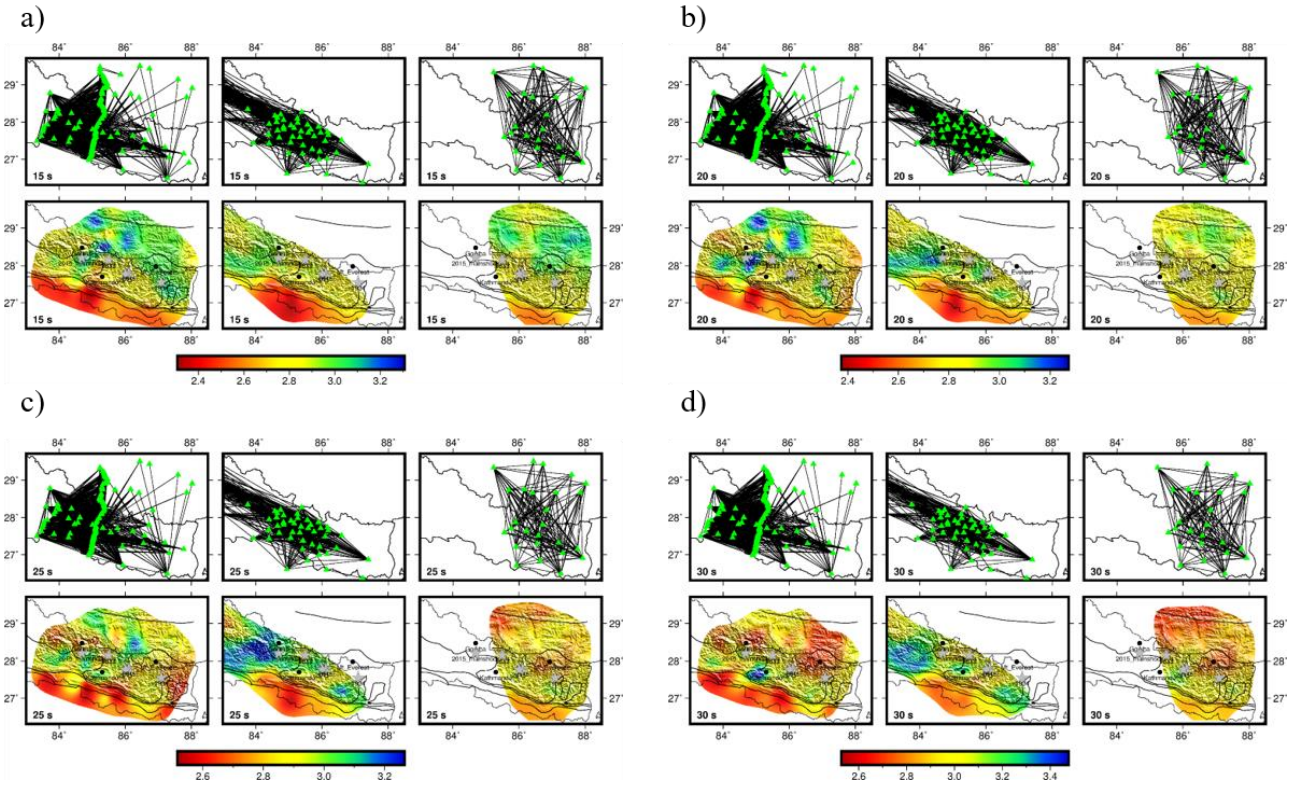

Figure2.22: a) Absolute group velocity images at 15 s, b) at 20s, c) at 25 s, and d) at 30 s coming from HiClimb (1st column), Namaste, HiKnet, Cambridge (2nd column), HiMnt (3rd column). First row is ray-coverage at each period and second row is absolute group velocity images.

2.3.2.2 Group Tomography of combined network

To increase the ray-coverage and lateral resolution, we decided to combine all the networks after comparing the tomographic image in all possible time periods and constructed group velocity maps at periods of 3-35 s (Fig2.23) for areas with good resolution. We know that shorter periods are more sensitive to the shallow crust, while the longer periods are more sensitive to deeper structures. The Rayleigh wave group velocity at 3-35 s can sample up to 70 km in our study area, which can be seen in the sensitivity kernel plot in figure2.25-2.26. The group velocity map shows the presence of low velocities anomalies at short periods beneath the southern region of Nepal. We also observe a major lateral velocity gradient between southern and northern part of the study area which is consistent with the geology of Nepal.

The group velocity tomography map separates the low velocity region in the south from the region in the north. The low velocity in the southern region corresponds to sediments believed to have been deposited by eroded Churia Hills and Mahabharat ranges by rivers and weathering, while the higher velocity in the central and northern regions corresponds to rocks such as conglomerates, schist, gneiss, granite, etc. Low and high velocities in different regions are due to different elastic properties of the material present in that region. In South Nepal, we observed that group velocity at periods of 5-15 s in the eastern part is relatively higher than central part, suggesting presence of compact sediments in eastern part of south Nepal. Another feature we can see in the tomographic group images is the high velocity between MCT and STD. The region between MCT and STD is called the Greater Himalayan Crystalline Sequence (GHCS), which consists mainly of metaigneous rocks and high-grade meta-sedimentary rocks (Hodges, 2000; Murphy & Yin, 2003).

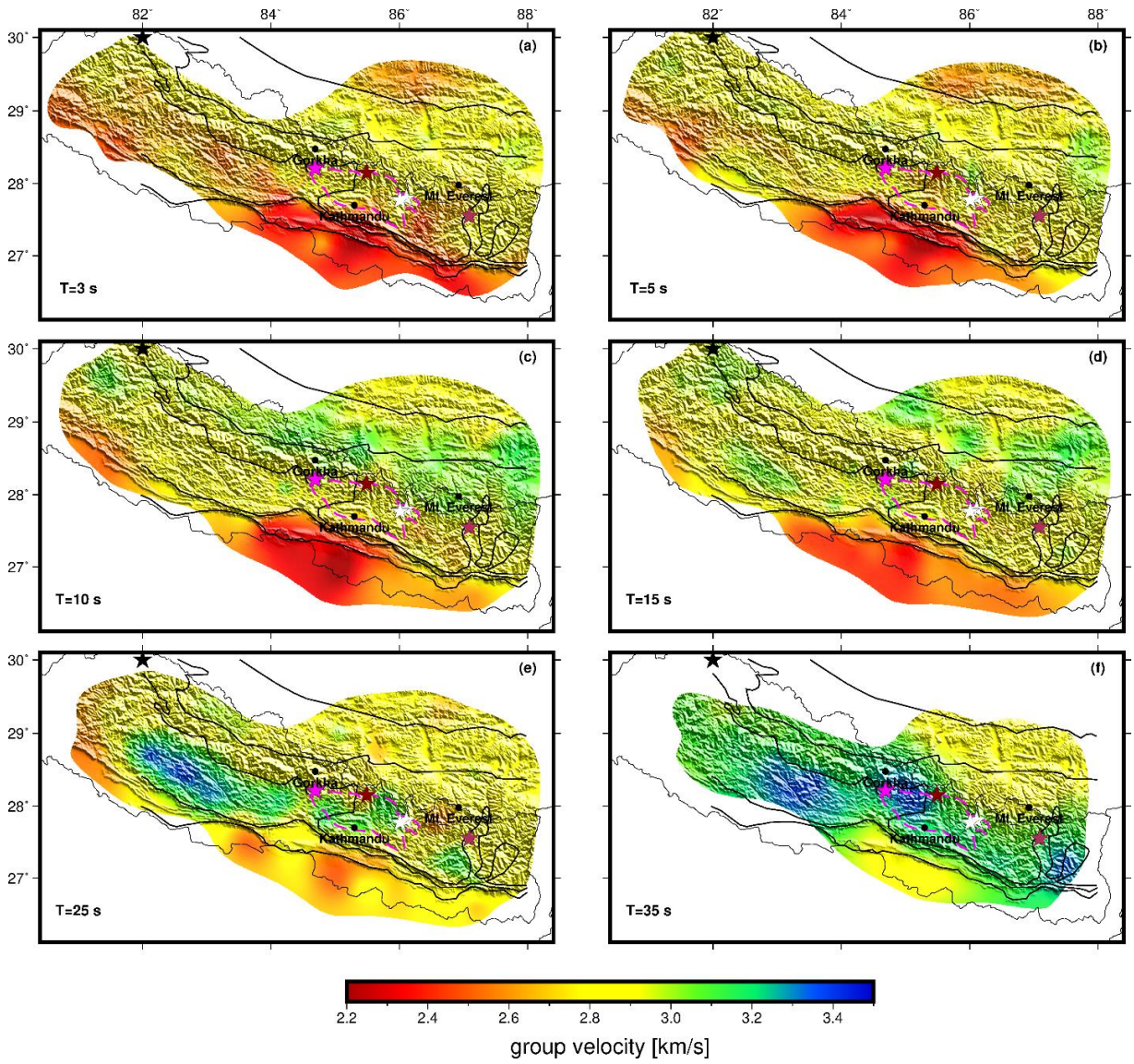

Figure 2.23: 2-D Rayleigh wave group velocity images from 3 s to 35 s. Periods are mentioned at bottom left of each plot. Results are shown only for the resolution length shorter than 120 km. Purple dashed line indicate the rupture of 2015 Gorkha earthquake. Magenta stars and white stars represent the mainshock and biggest aftershocks of 2015 Gorkha earthquake, darkred, maroon and black stars represent the epicenter of 1833, 1934 and 1505 earthquakes.

We observe an area of relatively high velocity at periods 3-15 s in North-West near the Indus Yarlung Suture (IYS) zone that may associate with the presence of dense rocks like ophiolite and mafic (Hébert et al., 2003). At short periods (3-5 s), group tomography shows the low velocity at north of IYS, which might show the presence metasedimentary rocks at shallow depth. At periods of 25-35 s, the velocity in the northern region is relatively lower than in the southern region, which could correlate with the thicker crust in the northern region compared to the southern region. The

group velocity map at 35 s shows the high velocity around the epicenter of 2015 Gorkha earthquake.

The maps of group velocity anomalies (Fig2.24) for periods 3-12 s show pronounced low velocity anomalies in Southern Nepal, indicating the presence of sediments. We could see that MHT acts as a boundary separating high and low velocity anomalies up to a period of 20 s. At longer periods of 30-35 s, we could see low velocity anomalies in the north of STD, which is an interesting feature because at shorter periods the high velocity anomaly was present there. At higher periods, the central part of Nepal shows a high velocity anomaly.

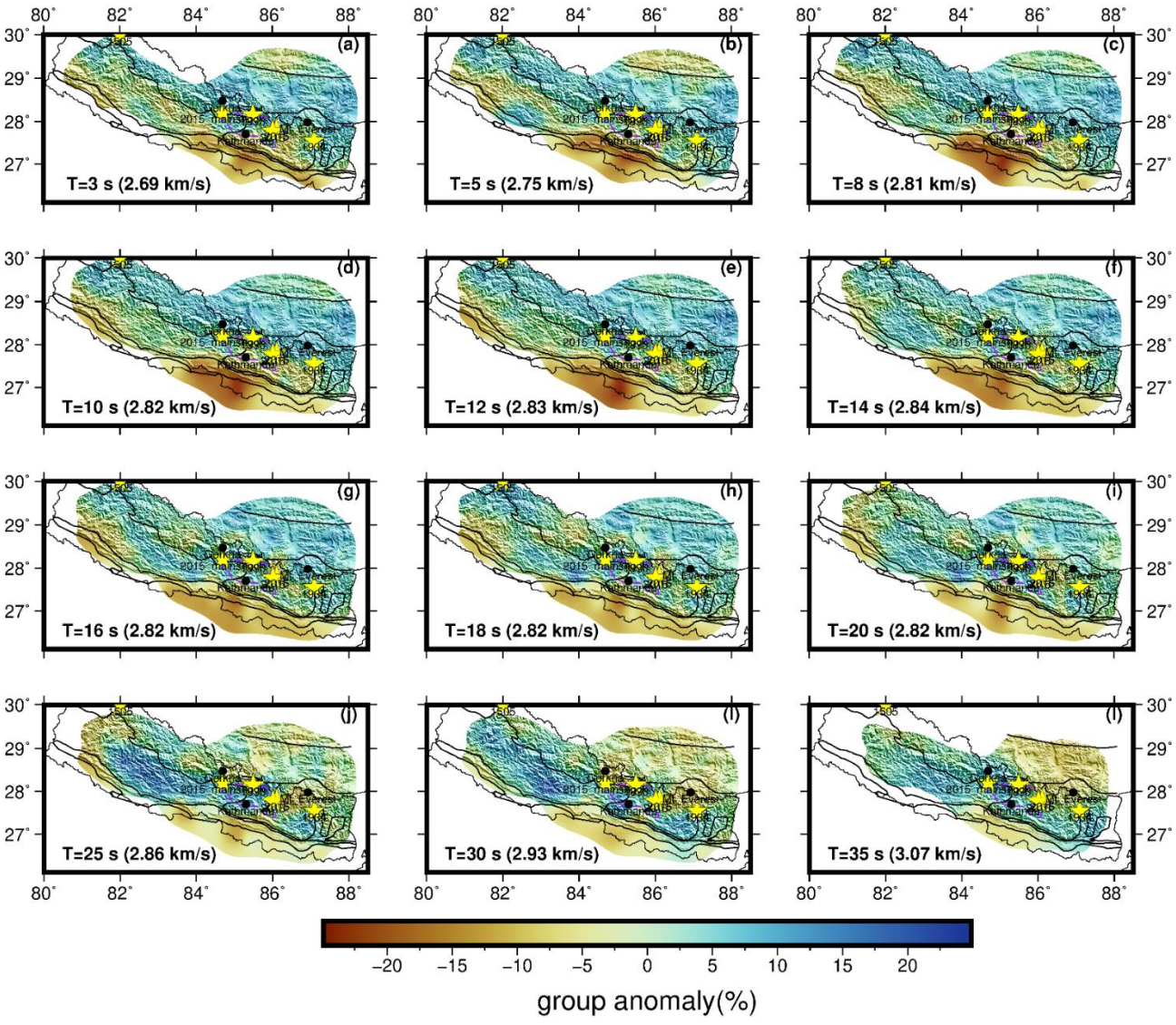

Figure 2.24: Rayleigh wave group velocity anomaly images from 3 s to 35 s. Period and mean velocity is mentioned at bottom left of each plot. Yellow stars are the earthquakes of magnitude greater than 7.0 across our study area.

2.3.3 Phase Tomography

2.3.3.1 Phase Tomography of individual network

The phase velocity images coming from HiMnt, HiClimb, Namaste, HiKnet, and Cambridge are well compared at short periods (see in Fig2.25 (a) and (b)) in the region under the ray-coverage. The velocity structure observed in these periods is same as we observed in the group tomography.

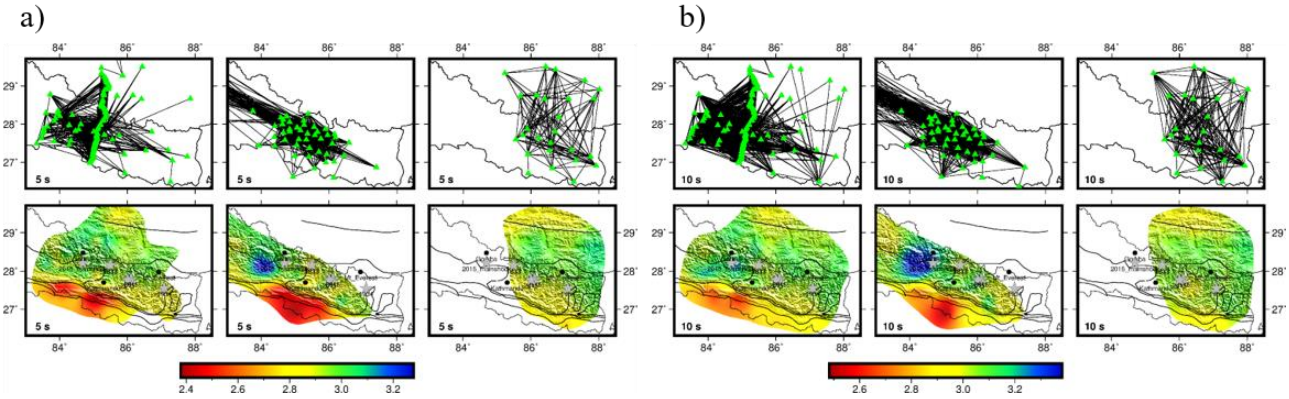

Figure2.25: a) Absolute phase velocity images at 5 s and b) at 10s coming from HiClimb (1st column), Namaste, HiKnet, Cambridge (2nd column), HiMnt (3rd column).). First row is ray-coverage at each period and second row is absolute phase velocity images.

At periods from 15 s to 30 s, one remarkable difference appeared around Gorkha in the phase tomographic images coming from, Namaste, HiKnet, and Cambridge. If we closely see the raycoverage at that place, most of the raypaths are parallel to each other. In other words, we do not have good crossing of raypaths in that place. So, the solution coming from Namaste, HiKnet, and Cambridge is not trustworthy. At the same place, there are quite good crossing of raypaths in case of HiClimb Network. At periods from 15s to 30 s, we could see relatively low phase velocity in South Tibet which is different from the structure we have seen in shorter periods. This feature is consistent in all the networks.

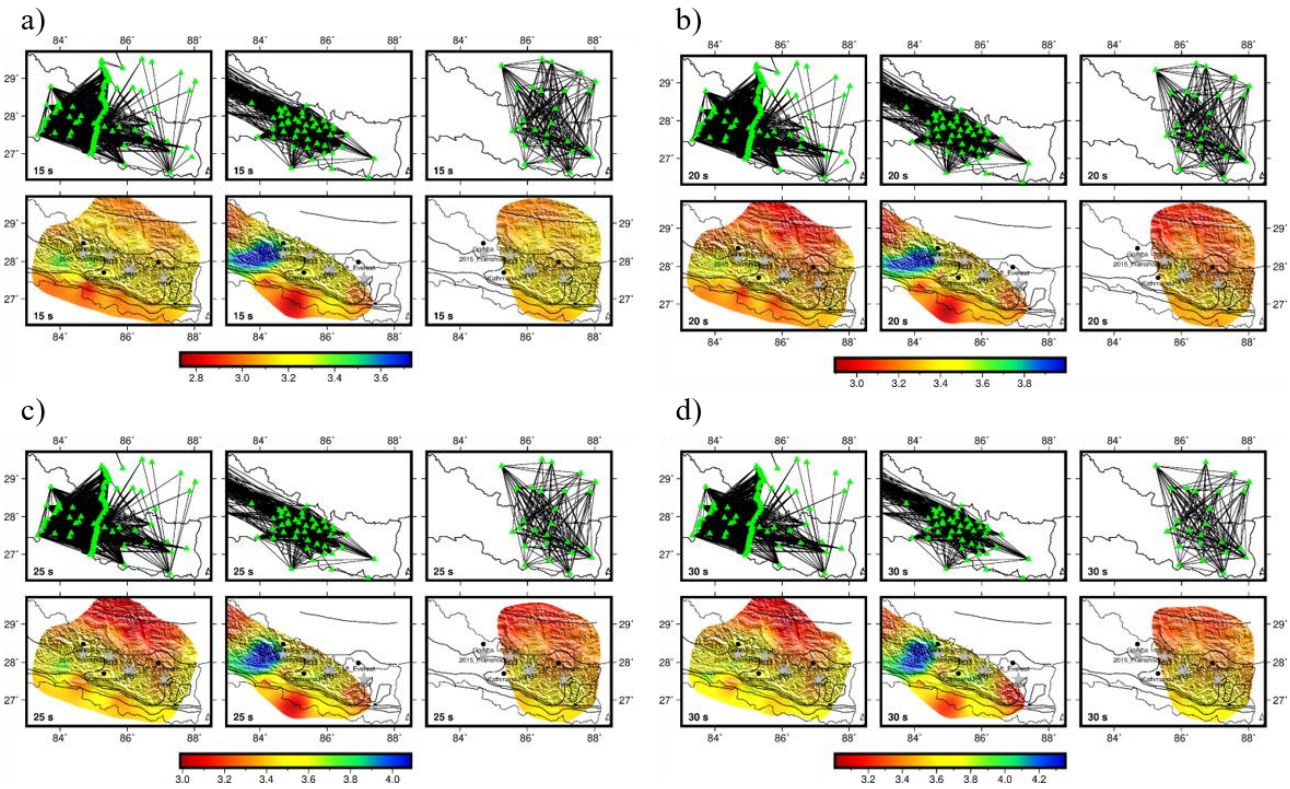

Figure2.26: a) Absolute phase velocity images at 15 s, b) at 20s, c) at 25 s, and d) at 30 s coming from HiClimb (1st column), Namaste, HiKnet, Cambridge (2nd column), HiMnt (3rd column). First row is ray-coverage at each period and second row is absolute phase velocity images.

2.3.3.2 Phase Tomography of combined network

Phase velocity maps of combined networks for periods 3-35 s are shown in (Fig2.27) for areas with good resolution. The phase velocity at a given period is larger than the group velocity, which is common, and samples a deeper structure, which is confirmed by the sensitivity kernel plot in (Fig2.29-2.30).

The phase velocity map up to 10 s has almost the same structure as the group velocity. At periods of 15-35 s, the phase velocity map shows the relatively lower velocity in the north of STD. The phase velocity anomalies shows that there are differences between the structure beneath the south and north and between east and west. The velocity gradient is more pronounced up to 10 s. At lower periods, the southern region with low velocity is separated from the northern region with high velocity in shorter periods, while at longer periods, the velocity in the southern region is relatively higher

than that in the northern region, which can be seen from the phase anomaly map (Fig2.28). The phase velocity maps up to 10 s show the relatively low velocity at north of IYS. The low velocity at 10 s might indicate the presence of partial melt at the mid-crust depths. The pronounced high velocity is observed around the epicenter of 2015 Gorkha earthquake at the period 35 s.

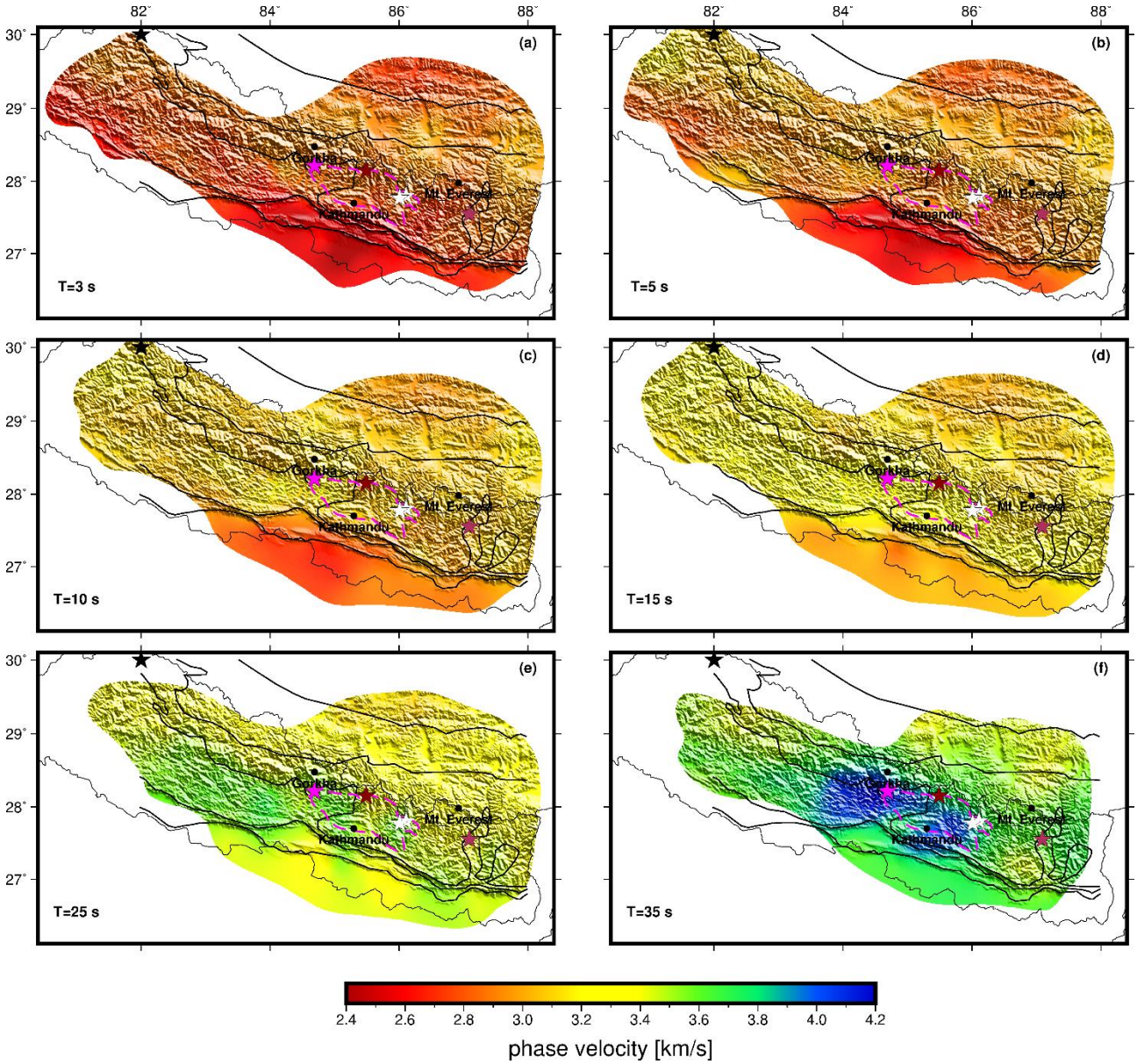

Figure 2.27: 2-D Rayleigh wave phase velocity images from 3 s to 35 s. Period is mentioned at bottom left of each plot. Results are shown only for the resolution length shorter than 120 km. Purple dashed line indicate the rupture of 2015 Gorkha earthquake. Magenta stars and white stars represent the mainshock and biggest aftershocks of 2015 Gorkha earthquake, darkred, maroon and black stars represent the epicenter of 1833, 1934 and 1505 earthquakes.

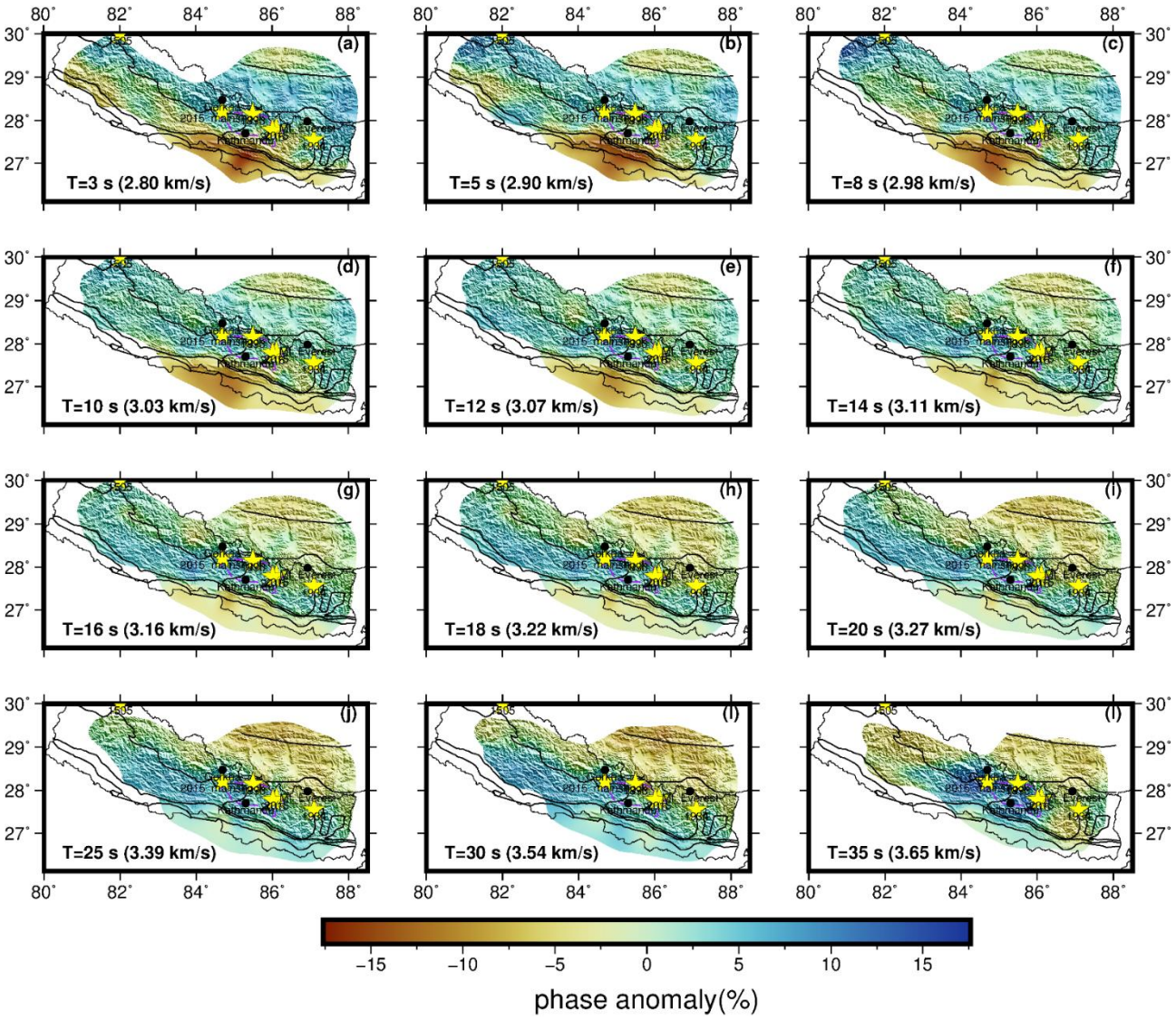

Figure 2.28: Rayleigh wave phase velocity anomaly images from 3 s to 35 s. Period and mean velocity is mentioned at bottom left of each plot. Yellow stars are the earthquakes of magnitude greater than 7.0 across our study area.

2.3.4 Sensitivity kernel

The group and phase sensitivity kernels indicate to what depth the group and phase of the Rayleigh wave are more sensitive at certain periods. We can calculate them by taking the partial derivative of the dispersion velocities with respect to the shear wave velocities. As we know in the case of the surface wave, energy is concentrated in a near-surface layer. Generally, the high energy of a surface wave is concentrated at the depth equivalent to half of its wavelength which implies that high frequency (small

wavelength) surface waves are sensitive to very shallow parts of the structure, while lower frequencies (longer wavelengths) become sensitive to deeper layers. For the same period, phase velocity measurements sample deeper structures than group velocity measurements. We can see that the sensitivity amplitudes for group velocities are higher compared to phase velocities for short periods, while for longer periods the phase sensitivity amplitudes are higher. Thus, for a shallow structure, the group velocity is sensitive and for a deep structure, the phase velocity is sensitive.

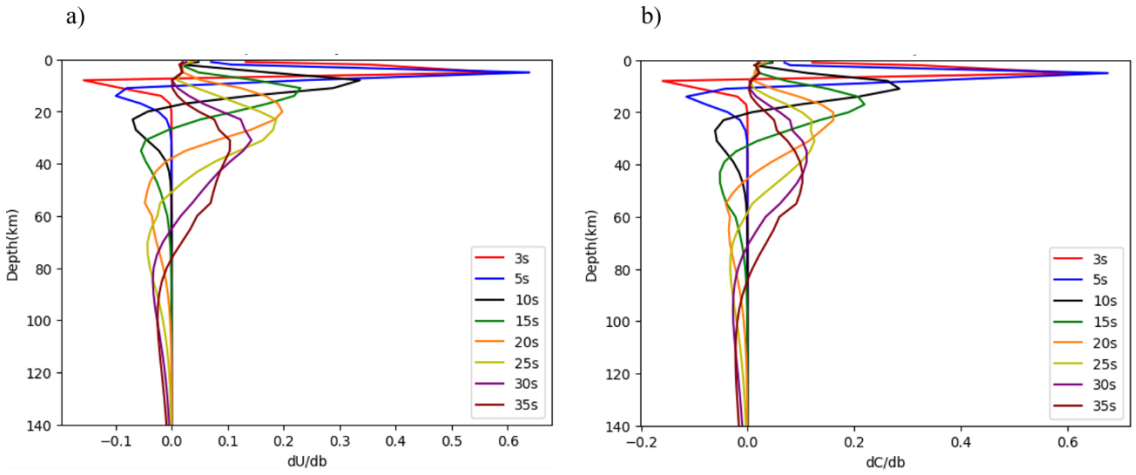

Figure 2.29: Group (left) and phase (right) sensitivity kernel for different periods (3-35 s).

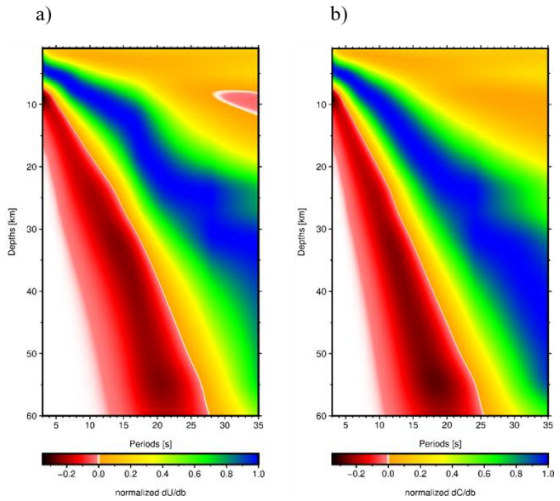

Figure 2.30: Group (left) and phase (right) sensitivity map for different periods (3-35 s).

We chose the local dispersion at the node where we have the best resolution and calculated the sensitivity amplitude at different depths. The Rayleigh wave group sensitivity map (Fig2.30) shows that we can sample up to 50 km at periods of 35 s,

while the phase can sample up to 60 km.

2.3.5 Shear wave velocity structure

We computed the 1-D shear wave velocity depth profile and uncertainties at each node of grids of size $0.30^0 \times 0.30^0$ over Nepal and part of South Tibet. To construct the 3-D shear wave velocity model over our study region, we combined all 1-D shear wave velocity depth profiles. The standard deviation at different depths is shown in figure2.31. The overall standard deviation in our study region from depth 0 to 60 km is less than 0.40, indicating that the velocity is fairly well constrained and resolved from the surface to a depth of about 60 km. The standard deviation is higher where the ray coverage is poor.

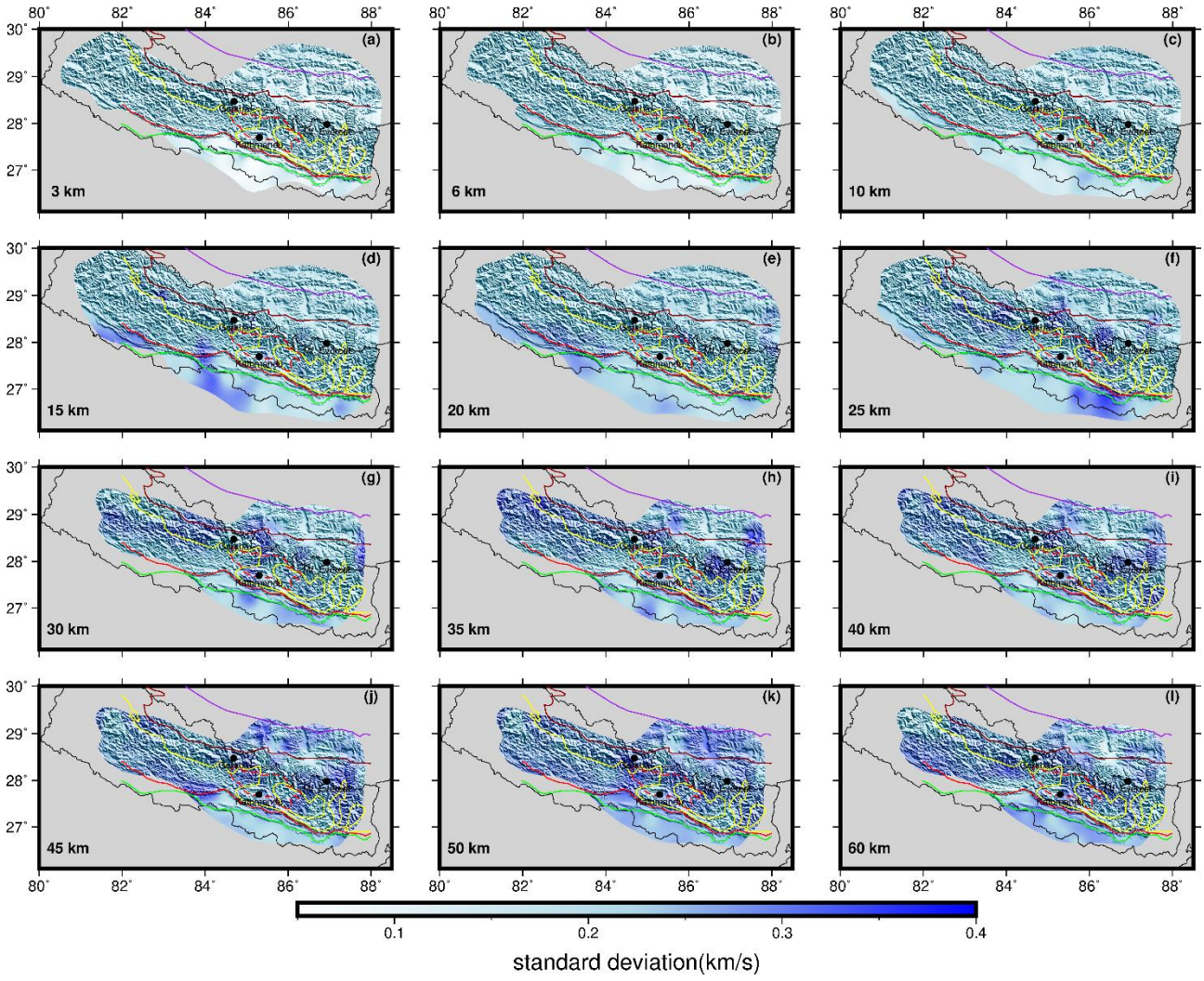

Figure 2.31: Standard deviation at different depth (mentioned in bottom left corner of each plot) across the study area.

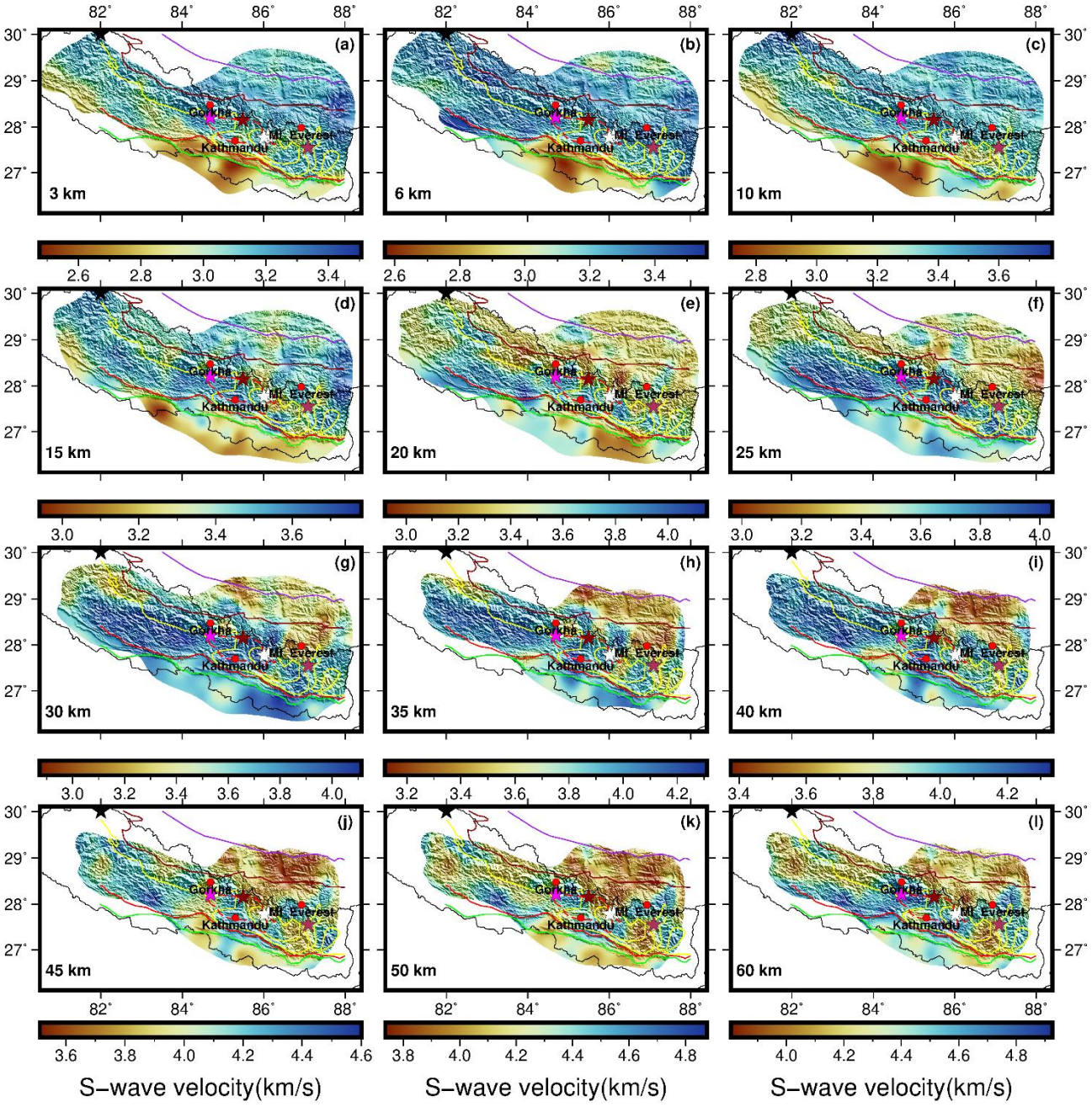

Figure 2.32: Shear wave absolute velocity variation map at different depths (3-60 km) across our study area (Nepal and Some part of South Tibet). Green solid line represents MFT, red solid line represents MBT, yellow solid line represents MCT, dark red solid line represents STD, purple solid line represents IYS, black solid lines is the political boundary of Nepal, red dashed line represent the rupture of 2015, Gorkha Earthquake. The stars represent the earthquakes of magnitude greater than 7.0.

Our results indicate the lateral variation shear wave velocity in shallow structure of crust and uniform in deeper structure (see in Fig2.32). We observed the low shear wave velocity in the south of MBT and the relatively high velocity in the north of MBT at shallower depth (upto 15 km). The low velocity in south of MBT is also observed by

Mitra el al., 2006. The velocity structure reverses at 20 km depth, low velocity at South Tibet, and relatively high velocity at Nepal. At 20-25 km depth, we observe an interesting feature of relatively high velocity in the region between MCT and STD, which indicates a stronger middle crust beneath Nepal. Same results obtained by Bai et al., 2019 from P wave velocity model. At a depth of about 50-60 km, the absolute shear wave velocity map shows almost uniform velocity throughout Nepal, and the anomaly map (Fig2.33 (b)) at these depths still shows low velocity anomaly under South Tibet and high under Nepal.

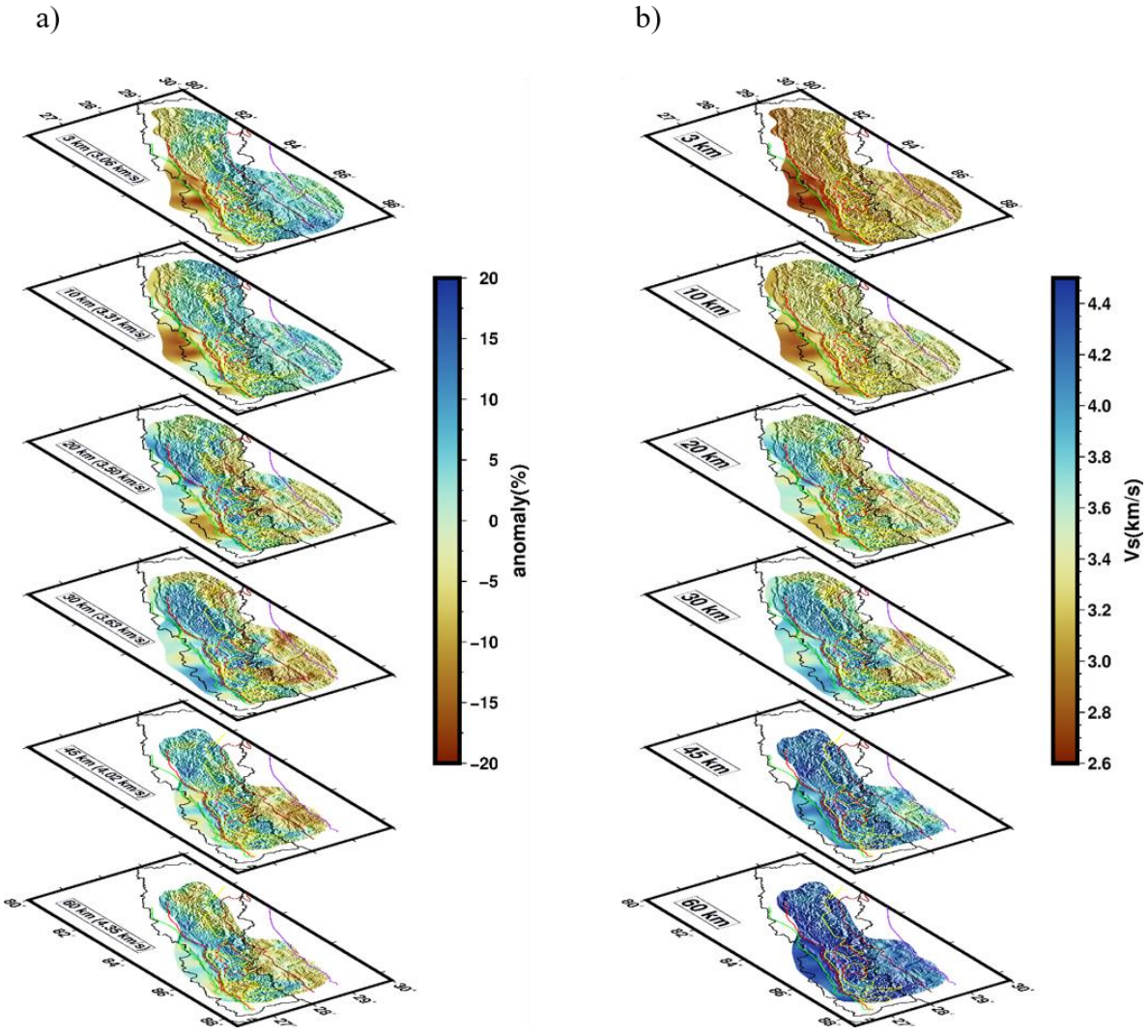

Figure 2.33: 3-D Shear wave velocity structure in Map view. a) Shear wave anomaly map. b) Absolute shear wave velocity map at different depths across our study area (Nepal and Some part of South Tibet). Depth and the corresponding mean velocity are mentioned in the bottom-left corner of each plot. Green solid line represents MFT, red solid line represents MBT, yellow solid line represents MCT, dark red solid line

represents STD, purple solid line represents IYS, black solid lines is the political boundary of Nepal, red dashed line represent the rupture of 2015, Gorkha Earthquake.

2.3.6 North-South S-wave velocity profile

We created five different profiles with a resolution of 60 km over our study area, oriented along South-North. The profiles along South-North were created to be perpendicular to the strike of the 2015 Gorkha Earthquake (Zhang et al., 2016). We visualized the shear wave velocity profiles of top 5 km and structure deeper than 5 km down to 60 km. The velocity profiles of top 5 km (see in Fig2.34) well correlated with the surface geology of our study area. We observed two distinguishing structures along North-South profiles, the low velocity in South of MCT and relatively high velocity in North of it. We also observed the low velocity beneath STD (see in Fig2.34 (f)).

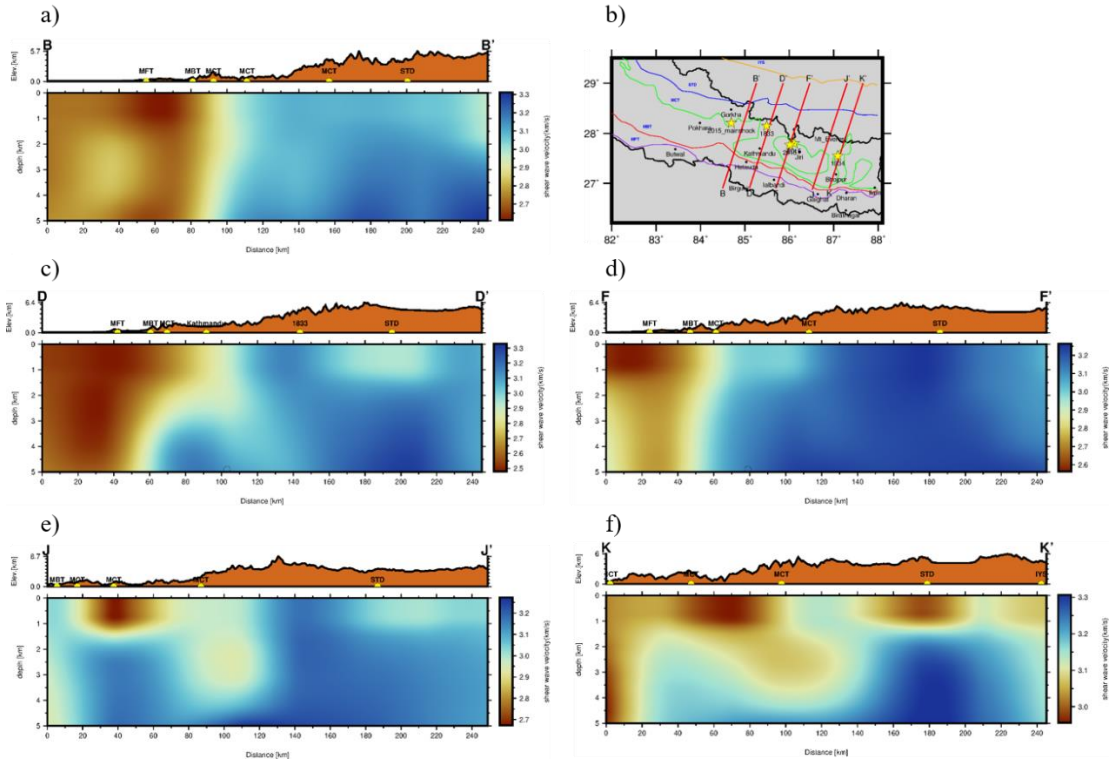

Figure 2.34: Shear velocity structure of top 5 km (a, c, d, e, f) across five different cross-sections along South-North. Topography along each profile is plotted with chocolate color. b) All the profiles are shown in map by thick red lines.

The vertical profiles of deeper structure (5-60 km) (Fig2.35) suggest a variable crustal thickness and complexity beneath Nepal and South Tibet. Each profile shows a clear

picture of the northward dipping Indian plate. All profiles show low velocity up to 10 km in the south of Nepal and the depth of the low velocity structure decreases as it moves northward.

In profile BB' (see in (Fig2.35 (a))), we observed the pronounced low velocity at 10-20 km depth beneath South Nepal. The low velocity layer is observed at 15 km depth between MFT and MCT, which deepens further at north of MCT to 25 km. We also found the high velocity around the hypocenter of 2015 Gorkha earthquake. This high velocity feature around the hypocenter 2015 Gorkha earthquake is also observed in P wave velocity model (Bai et al., 2019). The high velocity is observed at a depth greater than 45 km in south Nepal.

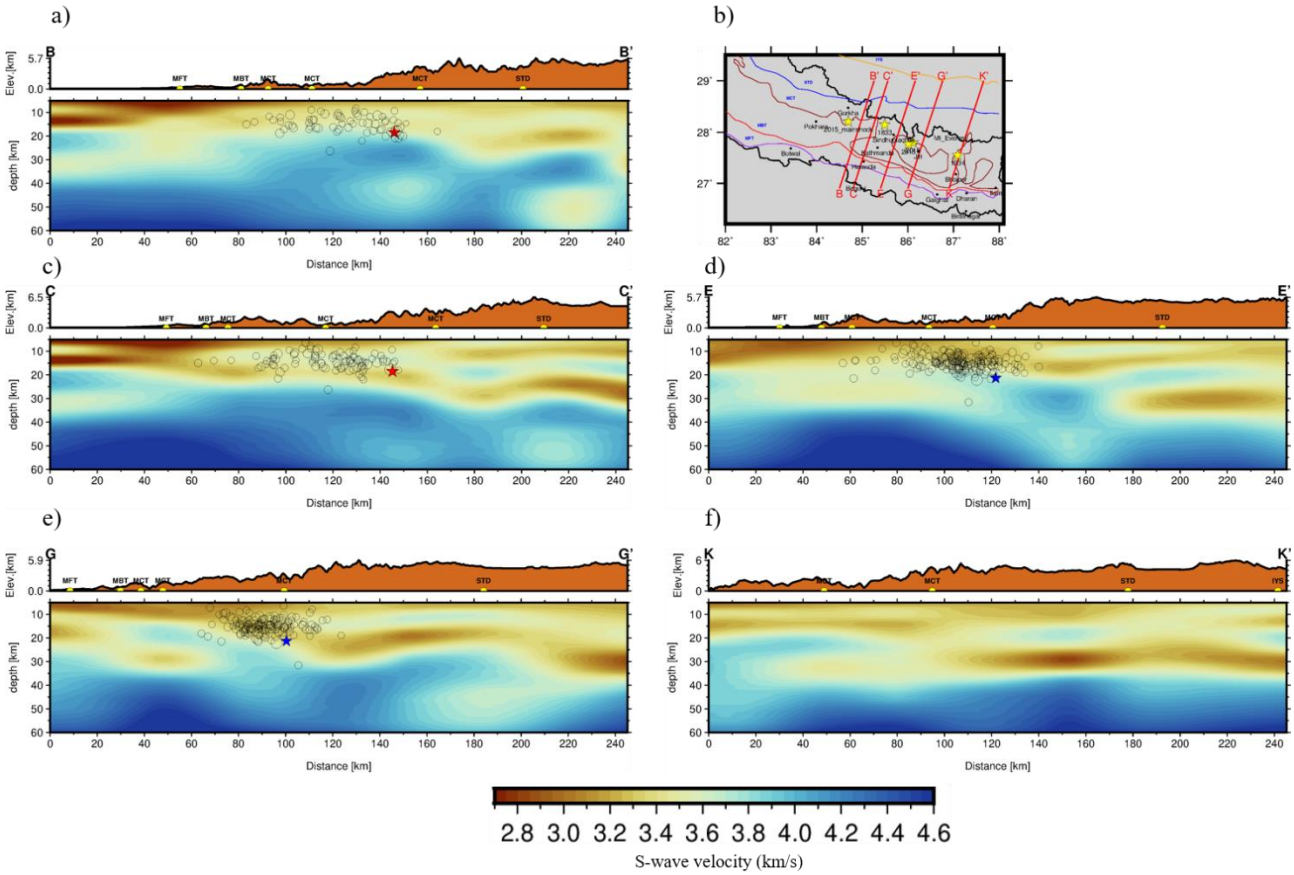

Figure 2.35: Shear velocity structure (a, c, d, e, f) across five different cross-sections along South-North. The black circles are the relocated aftershocks of 2015 Gorkha Earthquake (within 60 km away from the profile), red star indicates the mainshock and blue star represents the biggest aftershocks of 2015 Gorkha Earthquake. Topography along each profile is plotted with chocolate color. b) All the profiles are shown in map by thick red lines.

Along profile CC’ (see in (Fig2.35(c))), there is a clear low velocity layer which is deepening towards north. The depth of low velocity layer is ranges from 10-30 km across this profile. We observed low velocity structure at a depth of 30-40 km at south of MFT. Another noteworthy feature observed in this profile is relatively high velocity layer sandwiched between two low velocity layers beneath South Tibet at depth of 15 km and beneath the region south of MCT at depth 10 km. The high velocity is observed at a depth greater than 45 km in south Nepal like in profile BB’.

In profile EE’ (see in (Fig2.35 (d))), our results show a low velocity layer at a depth 10-30 km. We observed the double ramp beneath High Himalaya. Interestingly, the aftershocks of 2015 Gorkha earthquakes are concentrates along this region. There is another low velocity layer at a depth of 30 km in the region south of MCT. We also observed a high velocity at 30 km depth below the High Himalaya which separates the two low velocity structure. We observed high velocity at a depth greater than 45 km as we noticed in profile BB’ and CC’.

In profile GG’ (see in (Fig2.35 (e))), double low velocity layer is observed at depth of 10 km and 20-30 km in South Nepal. This low velocity layer is observed at a depth of 20 km beneath High Himalaya and at 30km beneath South Tibet. As like in other profiles, we observed the high velocity at a depth greater than 45 km in South Nepal. The relatively high velocity structure is observed at depth of 10 km beneath South Nepal and South Tibet. In profile KK’, we observed a complex structure between MCT and STD. In this region, we observed the velocity inversion at depth 15 and 25 km. The distinct low velocity layer at a depth of 15 km in the region south of MCT and at a depth 25-30 km in north of MCT is observed along this profile.

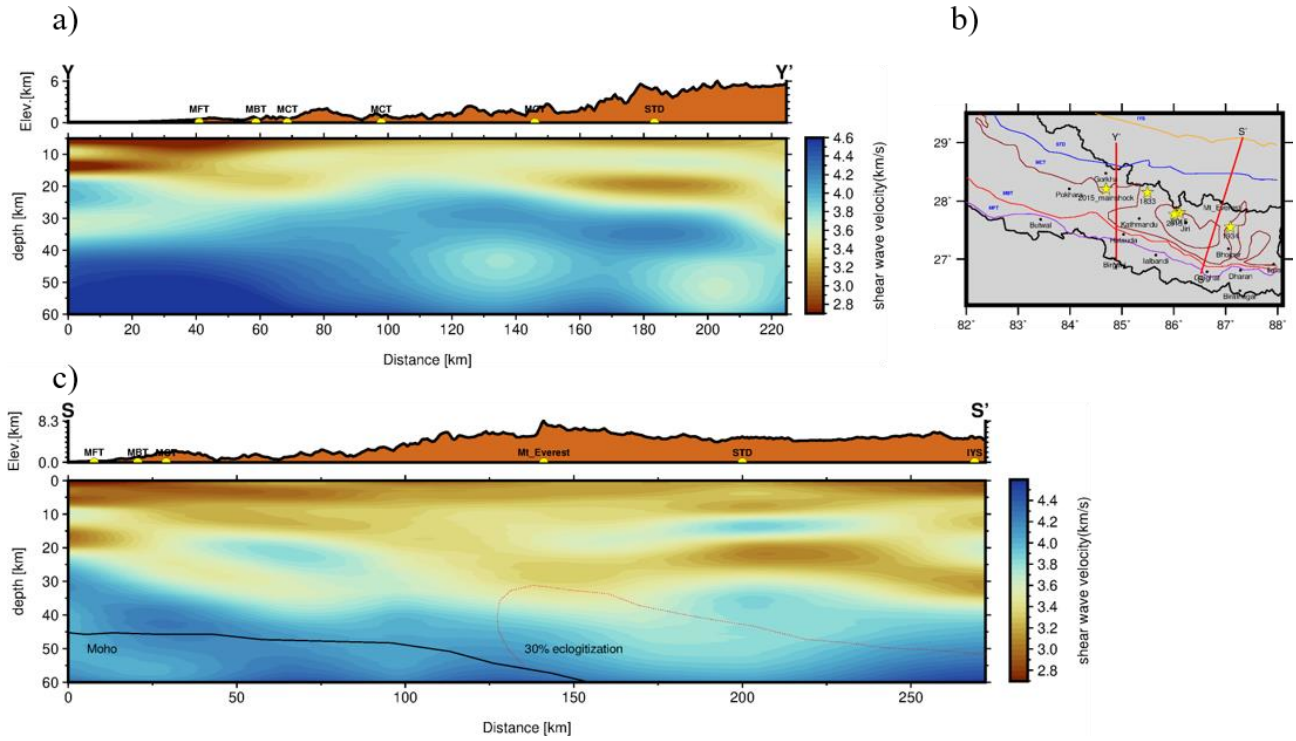

Figure 2.36: Shear velocity structure across two different cross-sections along South-North. Profiles are shown in map (right) by red thick lines.

We created two more profiles along South-North across our study area (Fig2.36). The idea behind creating these profiles is to observe shear wave velocity model along the profile for which the depth of the Moho and the complexity of the crust were studied by using the receiver function (Nábělek et al., 2009; Schulte-Pelkum et al., 2005). The thick black line along the YY' and SS' (see in Fig2.36 (a) and (c))) profiles represent the Moho studied by Nabelek et al., 2009 and Pelkum et al., 2005, respectively. Another study was conducted along the YY' (Fig2.36 (a)) profile by Xu et al., 2012. Here, the authors found the presence of a low velocity structure beneath southern Nepal, which is we also observed in our work. We observed an S-wave velocity of less than 2.8 km/s to a depth of 10 km in the south of MFT. The low velocity observe at mid-crustal depths beneath Nepal (10-20 km) and South Tibet (20-30 km) compares well with the work of Xu et al., 2012.

Along profile SS' (Fig2.36 (c)), a relatively high velocity layer is sandwiched between two low velocity layers at Southern Nepal and High Himalaya. The high velocity layer

at 10 km depth below South Nepal continues north of STD. The low shear wave velocity layer is observed at depth 10-30 km along this profile. The velocity gradient of upper crustal shear waves along the SS' profile is steeper beneath Nepal than beneath South Tibet. A high velocity structure (4-4.4 km/s) is present at 40-60 km depth beneath Mt. Everest. The red dotted line shows the region where Pelkum et al., 2005 claim partial eclogitization.

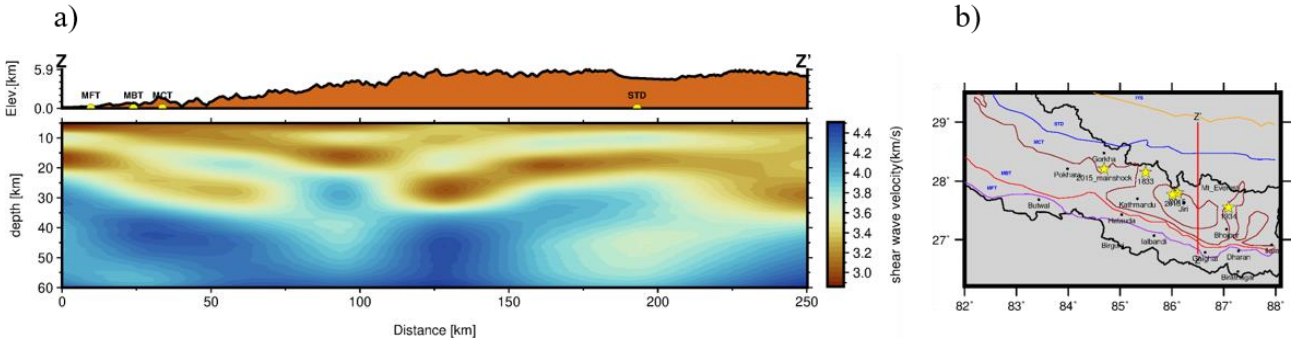

Figure 2.37: Shear velocity structure across South-North at longitude 86.5^{0}E. The profile is show in the map (right) by thick red line.

The south-north profile at longitude 86.5^{0}E shows shear wave velocity variation from latitude 26.75^{0}N to 29^{0}N (Fig2.37 (b)). We made this profile to show the enhanced shear wave velocity structure along this profile proposed by Guo et al., 2009. Since, we have dispersion data of 3 s, we recovered the shallower structure with high resolution, and we are the first to present the 3-D S-wave velocity model at a depth of less than 5 km. The previous model along this profile provided the S-wave velocity model from 5-35 km depth. The resolution in our study area is less than 30 km, which is better than previous studies (Guo et al., 2009). So, our S-wave model along this profile seems to be better in depth and lateral resolution as we combined the data from five different networks. Another study along this profile used local earthquake tomography method (Monsalve et al., 2008) to provide an image of the P-wave velocity and V_p/V_s model along profile. The main features observed along this profile are the presence of a low velocity layer down to 10 km depth from the surface beneath South Nepal. We observed this low velocity layer deepening towards north of MFT. The distinct low velocity layer at depth of 20-30 km beneath High Himalaya and South

Tibet is observed along this profile. There is 5 km thick high velocity layer sandwiched between two low velocity layers. The high velocity layer continues to the north of STD. Very high shear wave velocity is observed beneath the High Himalaya at a depth of 40-60 km. A low velocity layer is found at a depth of 15-25 km under the High Himalayas and South Tibet.

The velocity profile along SS' and ZZ' (see in Fig2.36 (a), 2.37(a)) is compatible with the attenuation model from previous studies. It has been observed that P and S waves are attenuated significantly more as they travel through the crust beneath the High Himalaya and the South Tibetan Plateau than waves traveling through the crust beneath the Lesser Himalaya (Sheehan et al., 2014). At the location where the attenuation is high, our results show a low S-wave velocity. In particular, high attenuation is observed at shallow depths in South Nepal, which is well consistent with the low shear wave velocity observed in our study. The low shear wave velocity below South Tibet up to a depth of 40 km is indicated by high attenuation in this region. The high S-wave velocity below the High Himalaya at 40-60 km depth is also consistent with the low attenuation observed at this depth and low velocity at 20-30 km beneath South Nepal agrees well with the high attenuation observed in a previous study at Lesser Himalaya (Sheehan et al., 2014).

2.3.7 East-West S-wave velocity profile

We created five different profiles with a resolution of 60 km over our study area, oriented along East-West. The profiles along East-West were created to parallel the strike of the 2015 Gorkha Earthquake (Zhang et al., 2016). We presented the velocity profiles of top 5 km and deeper structure (5-60 km). The shear wave velocity profiles of top 5 km (see in Fig2.38) clearly shows the upper crustal heterogeneities along East-West in our study area. We observed the low velocity structure below the epicenter of big earthquakes (Mw>7) (see in Fig2.38 (d) and (e)) that was occurred in our study area and beneath Katmandu (see in Fig2.38 (c)). We noticed that relatively high velocity structure separated the two low velocity along East-West profiles (see in

Fig2.38 (a), (e), and (f)). In profile NN' (see in Fig2.38 (d)), we obtained relatively high velocity structure (approximately 100 km) between the mainshock and biggest aftershocks of 2015 Gorkha Earthquake.

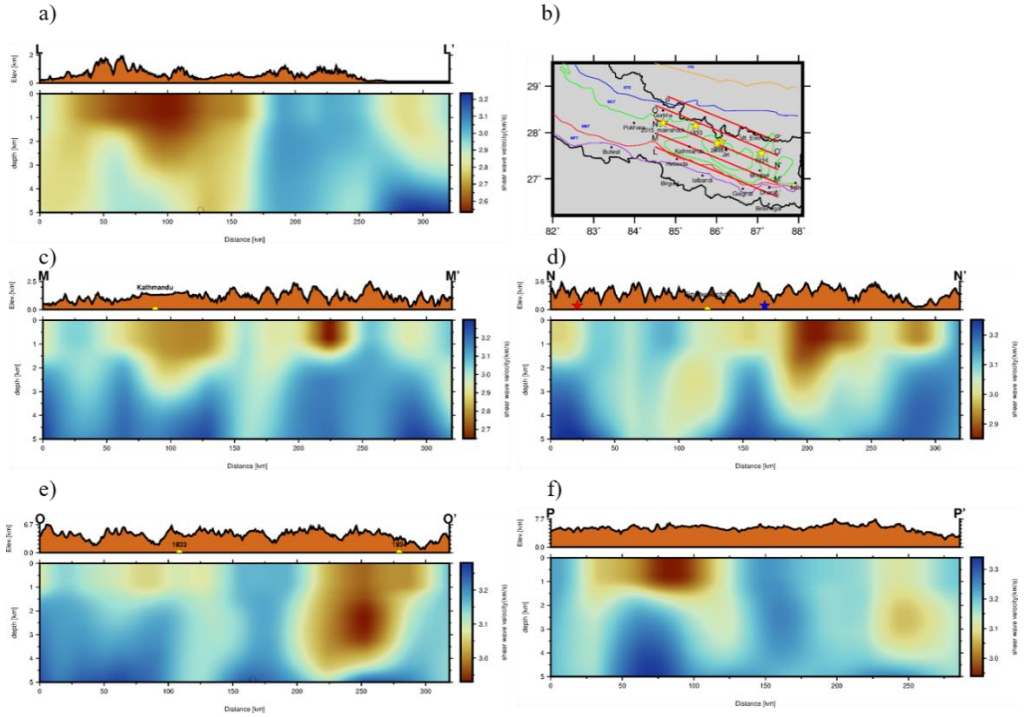

Figure 2.38: Shear velocity structure of top 5 km (a, c, d, e, and f) across five different cross-sections along East-West. The red and blue stars represent the epicenter of mainshock and biggest aftershocks of 2015 Gorkha Earthquake. Yellow circles represent the location of Kathmandu, Sindhuplachok and epicenter of 1934 and 1833 earthquakes. Topography along each profile is plotted with chocolate color. b) All the profiles are shown in map by thick red lines.

All the velocity profiles of structure from depth 5 km to 60 km along East-West (Fig2.39) clearly show a low velocity structure to a depth of 10-30 km and the Indian crust below 30 km. The depth of low velocity layer is increasing as we move northwards (for example, low velocity layer is found at 10 km in profile LL' (Fig2.39 (a)) and at 20-30 km in profile PP' (Fig2.39 (f))). There is not much lateral variation in the depth of low velocity along each profile. We observed double low velocity layer at the west of the epicenter of biggest aftershock of 2015 Gorkha earthquake (see in Fig2.39 (f)). In profiles NN' and OO' (Fig2.39 (d, e)), the high velocity structure (>4.4 km/s) is observed at 50 km depth. The high velocity structures are consistently present at 50 km depth in South Tibet and Eastern Nepal in all the profiles. Particularly, NN'

profile links the mainshock of 2015 Gorkha Earthquake and its largest aftershocks. The velocity structure along this profile (Fig2.39 (d)) shows that the hypocenter of the mainshock of 2015 Gorkha Earthquake and its largest aftershocks are located at the interface. We also observed the low velocity structure present at a depth of 20-30 km between the hypocenter of mainshock of 2015 Gorkha earthquake and its biggest aftershocks.

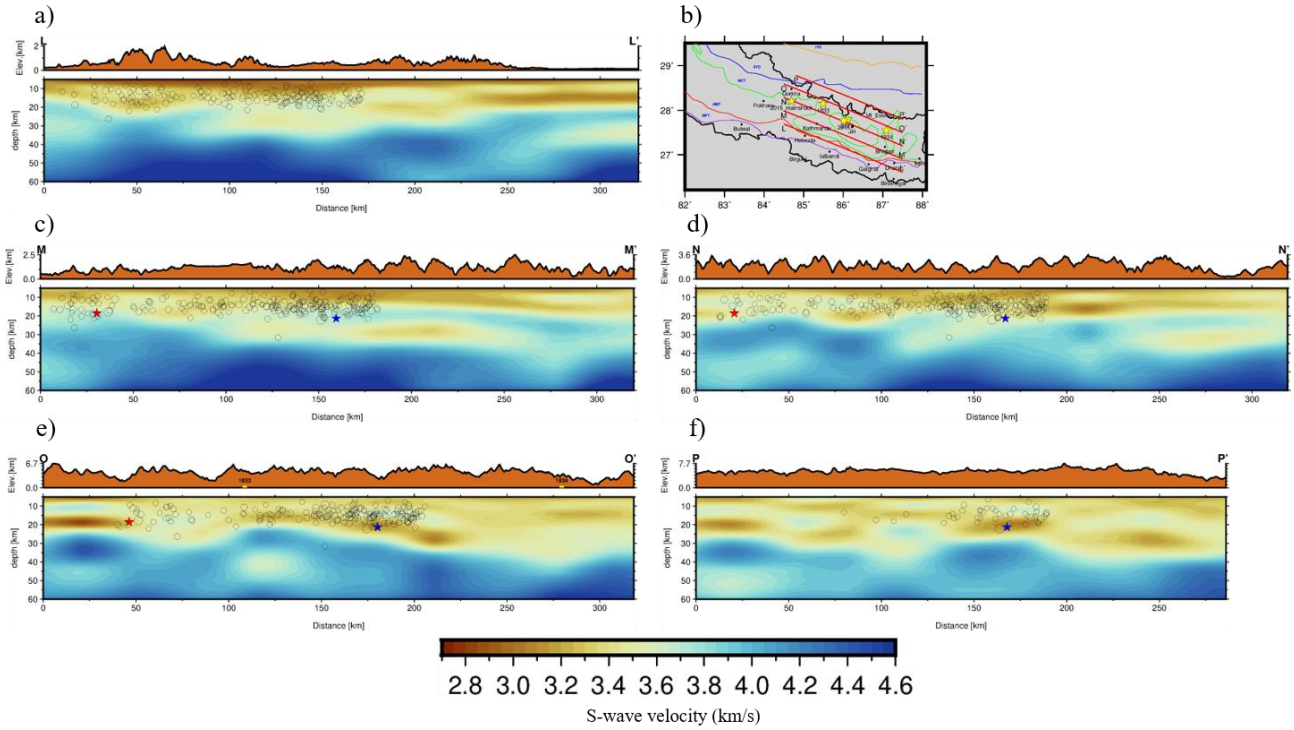

Figure 2.39: Shear velocity structure (a, c, d, e, and f) across five different cross-sections along East-West. The black circles are the relocated aftershocks of 2015 Gorkha Earthquake (within 60 km away from the profile), red star indicates the mainshock and blue star represents the biggest aftershocks of 2015 Gorkha Earthquake. Topography along each profile is plotted with chocolate color. b) All the profiles are shown in map by thick red lines.

2.3.8 S-wave uncertainty profile

The one standard deviation from the estimated mean shear wave velocity along the North-South and East-West sections are presented in figure2.40-2.43. The standard deviations profiles shows that high uncertainty near the location of interfaces which might be the smearing of the velocity structure (Manu-Marfo et al., 2019). The results

show that uncertainties in each section are less than 0.40 which indicates that the inverted velocity are reasonably well resolved from surface down to depth 60 km.

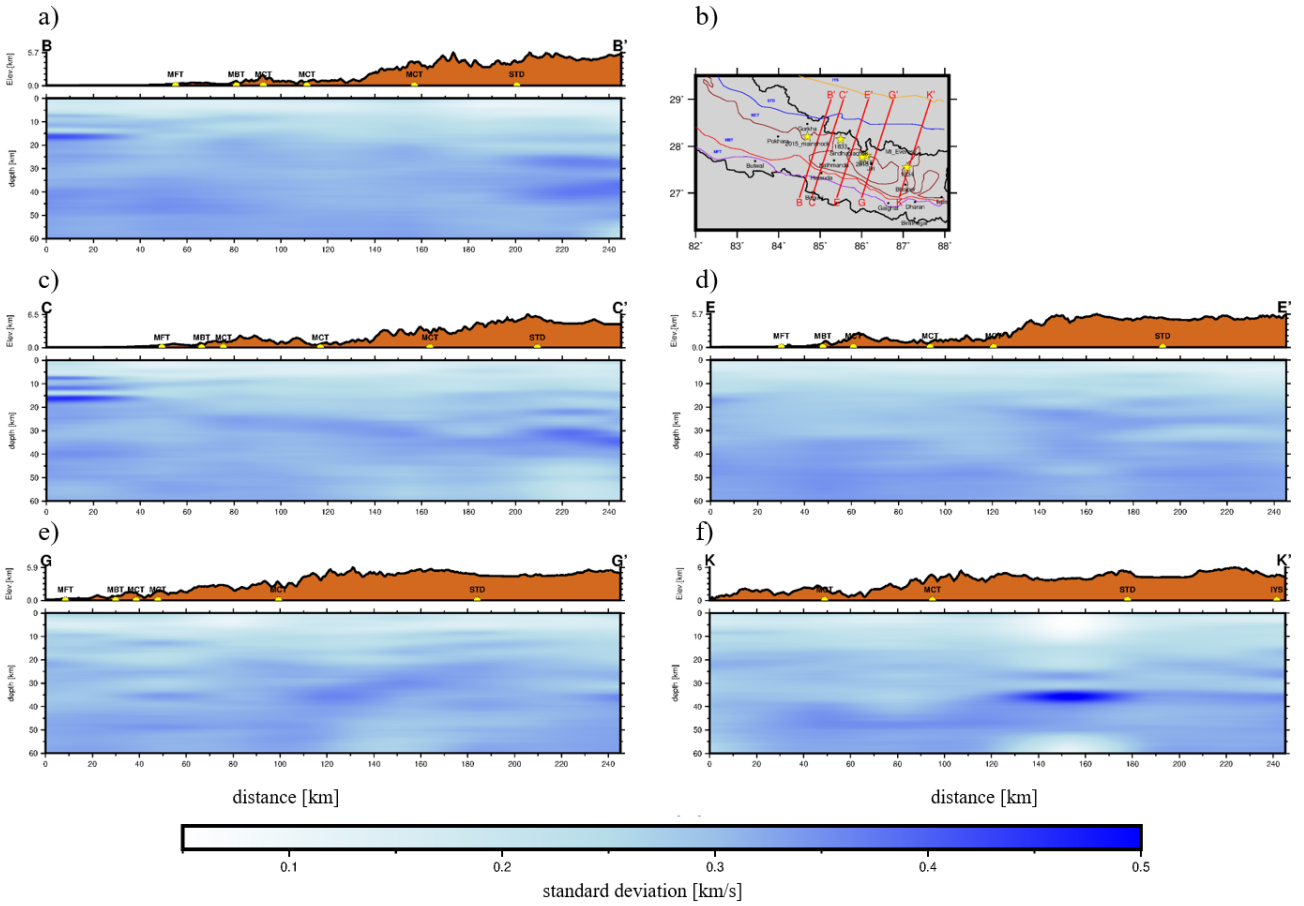

Figure2.40: standard deviations of the vertical sections corresponding to the shear wave velocity profiles shown in Figure2.35.

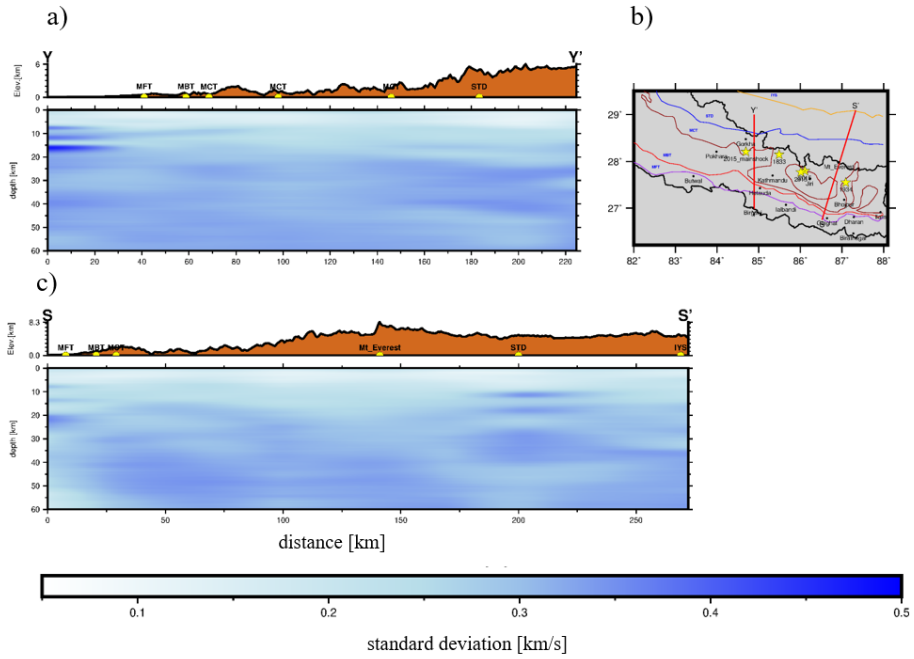

Figure2.41: standard deviations of the vertical sections corresponding to the shear wave velocity profiles shown in Figure2.36.

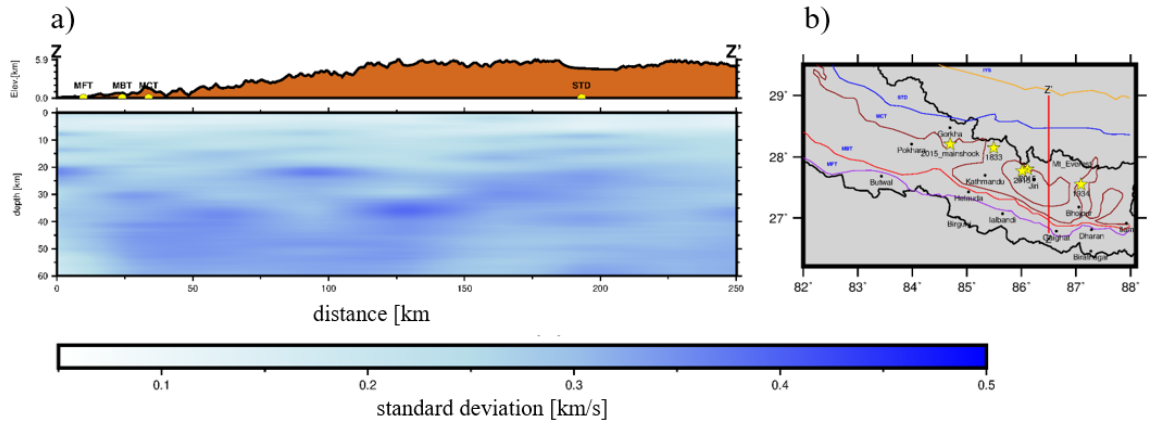

Figure2.42: standard deviations of the vertical sections corresponding to the shear wave velocity profiles shown in Figure2.37.

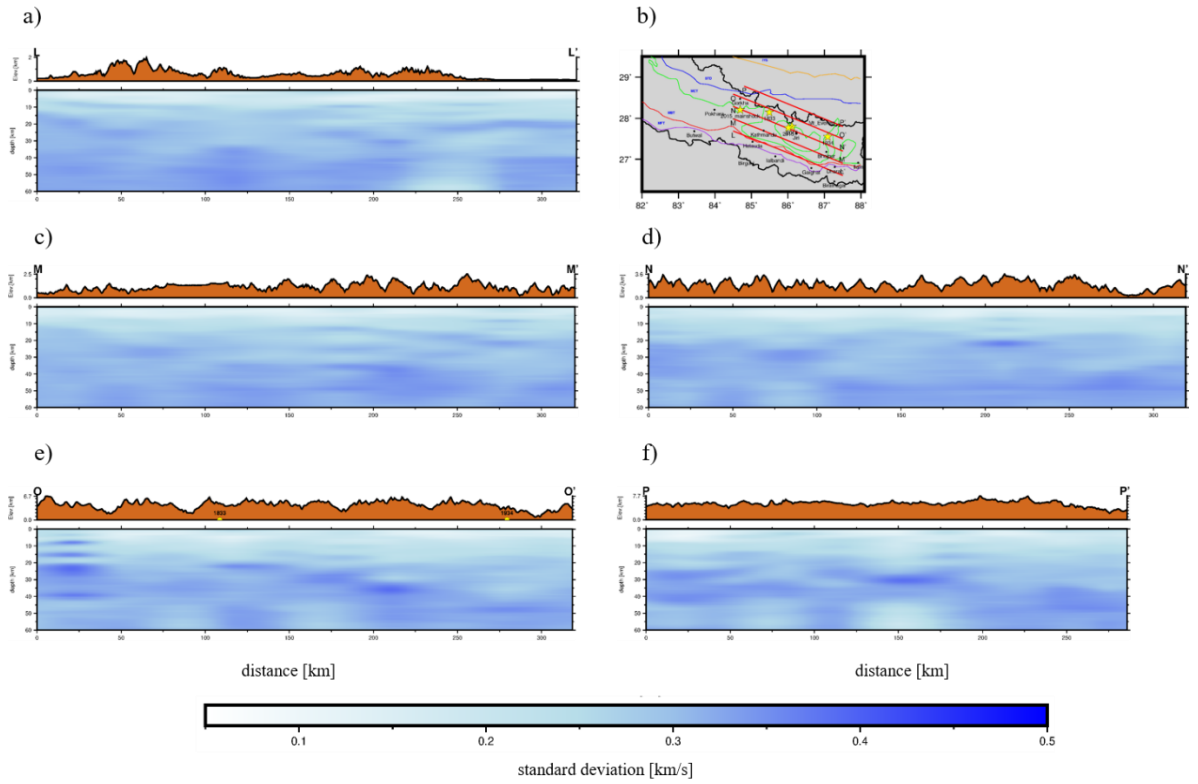

Figure2.43: standard deviations of the vertical sections corresponding to the shear wave velocity profiles shown in Figure2.39.

2.4 Discussions

The lateral variation of shear wave velocity in our study region at shallow depths (up to 15 km) seems to be well correlated with the main feature of the surface structure. At shallow depths, the MBT separates the low and high velocities in Nepal. The low velocity in the south of the MBT may result from the thick sedimentary cover in the Indo-Gangetic plains and alluvial sediments, while the high velocity in the north of the MBT indicates the presence of high-density rocks (e.g., granite, schist, marble, phyllite, gneiss, quartzite, etc.) (Upreti, 1999). We observed the relatively high velocity in the south of MBT over East Nepal as Central Nepal. This could indicate the presence of compact sediments in Eastern Nepal and loose sediments in Central Nepal. Looking at the shear wave velocity structure at South Tibet up to 15 km (see in Fig2.28), we observe that the velocity increases as a function of depth, but low velocity structure is detected at 20 km depth. The low velocity at this depth might indicate the presence of a low mid-crustal velocity structure beneath South Tibet (Guo et al., 2009). At depths of 20-25 km, the shear wave velocity seems to be high in the region between MCT and STD. The relocated aftershocks distribution of the 2015 Gorkha Earthquake (Bai et al., 2016) shows that most aftershocks occurred in this region (between MCT and STD), as shown in figure2.44. The larger earthquakes in our study area (represented by the black star in Fig2.33) also occurred in the same region. This may indicate the presence of a strong mid-crustal layer beneath this region. The previous study shows that a high P-wave velocity occurred in the aftershock zone and hypocenter of the mainshock of the 2015 Gorkha Earthquake (Bai et al., 2019). The structure determined from the P-wave velocity is well supported by our study.

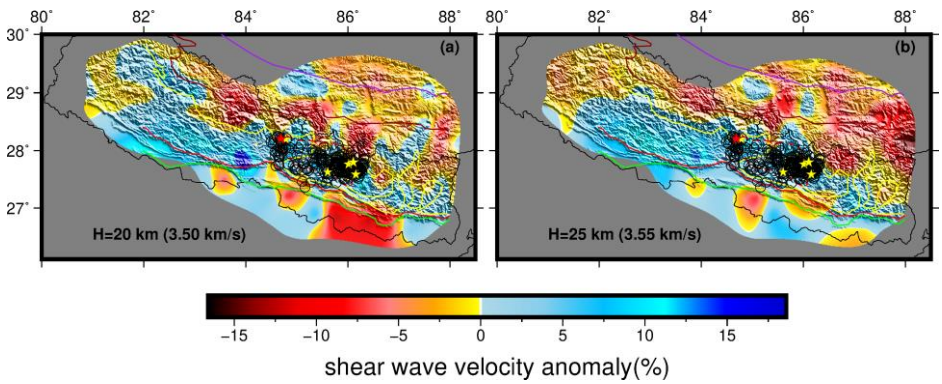

Figure 2.44: Shear wave anomaly map at depths 20 and 25 km across our study area. The black circles represent the location of relocated aftershocks of 2015 Gorkha Earthquake, red stars represent the location of Mainshock, and yellow stars represents the aftershocks of magnitude greater than 6.0.

The relatively lower velocities in the middle and lower crust below South Tibet than under Nepal suggests the presence of weak crust beneath South Tibet. S-wave velocity of about 4.2 km/s and 3.8 km/s at a depth of 45 km beneath Nepal and South Tibet indicates that we are likely sampling the upper mantle beneath South Nepal and are still in the lower crust below South Tibet. These results support the presence of a thick crust beneath South Tibet. At the same time, our results show the variation in crustal thickness as we move from South Nepal to South Tibet.

The low velocity observed below the epicenter of 1934, 1833 and 2015 earthquakes might indicate the presence of loose sediments. The low shear wave velocities indicate the low elastic stress that might explain why the seismic rupture did not propagate to surface in each earthquake. The low velocity in the west of epicenter of biggest aftershocks of 2015 Gorkha earthquake might have controlled the size of earthquakes. We observed that rupture of 2015 Gorkha earthquakes stopped in this region. The low velocity beneath Katmandu, Sindhuplachok and STD might indicate the presence of sediments in the shallow crust. The shear wave velocity might have correlation with the ground shaking. It is assumed that shaking is high in the region having low shear wave velocity and vice versa (Khan, 2013). Our results show the low shear wave velocity beneath the region which were hardly hit by 2015 Gorkha Earthquakes (for example, Sindhuplachok, Kathmandu valley, etc.). Hence, we assumed that having shear wave velocity model of shallower depth provides constrain on the seismic hazard analysis in seismically active region like our study area, Nepal.

Lateral variation of shear wave velocity in the top 5 km along the profiles in North-South and East-West might represent the lateral heterogeneities in the upper crust beneath the Nepal Himalaya. The relatively high velocity in each profile might

represent presence of compact sediments in that region.

The low velocity layer observed at shallow depths below South Nepal along profile ZZ' (Fig2.37 (a)) indicates the presence of a thick sedimentary basin. The decreasing thickness of the low velocity layer towards north of MFT indicates the presence of compact sediments or dense rocks in shallow crust beneath north Nepal. The most exciting feature observed along profiles ZZ' (Fig2.37 (a)) and SS' (Fig2.36 (a)) is a high velocity layer sandwiched between two low velocity layers below Lesser Himalaya. The high velocity layer observed beneath South Nepal is further extended to the north of STD. This high velocity layer beneath South Nepal at a depth of 10 km is explained as a shear zone as receiver function of stations in this region shows polarity reversal in radial component and transverse component (Schulte-Pelkum et al., 2005). The shear wave velocity model along the SS' and ZZ' profile shows that this high velocity lies between two low shear velocity layers under the High Himalaya and part of South Tibet. This suggests the presence of a continuous shear zone as far north as STD at depths of 10-15 km. A similar type of shear wave velocity structure was found in the Southern Zagros collision zone. Pilia et al., 2020 found a high velocity layer between two low velocity layers and they interpreted the high velocity layer as the base of the Phanerozoic sedimentary cover (Pilia et al., 2020). Another remarkable feature observed along these profiles is the very high S-wave velocity (4.2-4.5 km/s) at a depth of 40-60 km below the High Himalaya. The V_p/V_s model (Monsalve et al., 2008) shows that the V_p/V_s ratio at this depth beneath the High Himalaya is high (about 1.80). If we calculate the P-wave velocity using the S-wave velocity from our model and V_p/V_s from the model of Monsalve et al., 2006 (Monsalve et al., 2006), then the P-wave velocity at 40-60 km beneath the High Himalaya is 7.5-8.1 km /s. With such a high V_p/V_s, high S and P wave velocities in the lower crust indicate the presence of partial eclogitization. As we know, the velocities in the lower crust (V_s =4.2-4.5 km/s, Vp =7.5-8.1 km/s) are fast even for mafic crust at temperature and pressure conditions typical for a depth of 40-75 km but can be easily reached when some of the material has been converted to eclogite. Eclogitization is corresponding with notable changes

in petrophysical properties, remarkably a density (10-15%) and V_p increase which may give a mantle like velocity to an eclogitized crust. It has been found that dry crust subducted into roots of continental collision zones will undergo eclogitization only if hydrous fluids are available (Austrheim et al., 1997). The high velocity observed at depth greater than 45 km beneath Terai (region south of MFT) and Lesser Himalaya indicate presence of upper mantle materials at these depths. The relatively low velocity at these depth beneath South Tibet clearly indicates the presence of thicker crust in this region than Nepal.

The low velocity layer observed beneath Lesser Himalaya (15-25 km depth) and High Himalaya (25-30 km depth) may indicate the presence of aqueous pore fluids as suggested by the calculations of Nakajima et al., 2001 and Sato and Ito, 2002. The fluid may be obtained from dehydration reactions (water released from sediments) as the Indian plate slides beneath Eurasia. The presence of aqueous fluids lowers the effective Coulomb stress, which brings nearby materials closer to failure. Therefore, the presence of fluids plays an important role in seismic activity. Another possibility is the presence of partial melt. There is ample field evidence from GHS that melt was present during much of its deformation history (Jamieson et al., 2004). The origin of the crustal fluid/partial melt is commonly correlated with the high heat generation in the Himalayan arc as a result of the India-Asia collision (Hochstein & Regenauer-Lieb, 1998). We know that the velocity of the shear wave also depends on the composition of the rock.

Shear wave velocity profiles oriented along SW-NE direction clearly shows up-dip (towards south-west) and down-dip (towards north-east) low velocity which further broadens beneath South Tibet (see in Fig2.35 (e)). The velocity of this layer is nearly 14 % lesser than upper and lower strata. The low velocity observed might be related with presence of anisotropic minerals or water content released by sediments while Indian plate subducted beneath Tibetan plate. The interface between the low and high velocity is considered as the MHT where all the major thrusts MFT, MBT and MCT

splits at depth from this single decollement zone (Nábělek et al., 2009; Schulte-Pelkum et al., 2005). We observed the double ramp in MHT (see in Fig2.35(c)) near to the hypocentre of recent Mw 7.8 Gorkha earthquake of 2015. It is assumed that ramps on the MHT are the barriers and play an important role in the rupture of the MHT during the occurrence of big earthquakes (Bai et al., 2019; X. Wang et al., 2017). Previous studies showed that flat portion between double ramps in the MHT has ruptured during the Gorkha earthquake and both ramps along the up-dip and down-dip played a crucial role in controlling the rupture in both directions (Avouac et al., 2015; Elliott et al., 2016; Grandin et al., 2015).

The low velocity in the middle of the crust observed beneath South Tibet is consistent with previous studies (Nelson et al., 1996; Pelkum et al., 2005; Unsworth et al., 2005; W. Zhao et al., 1993). The low velocity to a depth of 40 km indicates the presence of mechanically weak crust beneath South Tibet, which plays a significant role in Himalaya-Tibetan orogenic processes. The thick crust located beneath South Tibet could cause the additional heat in the crust and the temperature line to extend to the melt line of the materials which is supported by thermal structure across our study region (Henry et al., 1997; Royden, 1993). Based on the thermal structure and composition of the rocks, partial melting seems to occur within the crust beneath South Tibet (McKenna & Walker, 1990). Thus, the low mid-crustal velocity observed in our study at South Tibet might be the indication of presence of partial melt. The low velocity in the middle and upper crust at South Tibet could also indicate the presence of warm, felsic rocks similar to those exposed in the Himalayas (Bollinger et al., 2006).

2.5 Conclusion

We created the high-resolution (less than 30 km in central Nepal and 60 km over most of the region) group and phase velocity maps in periods of 3-35 s over Nepal and part of South Tibet by cross-correlating ambient noise data recorded by stations distributes across our study area. The 2-D tomography results clearly show the velocity gradient

along South-North. At shorter periods (sensitive to shallow structures), the south of the MBT shows low group and phase velocities, while the north shows relatively high velocities. These results correlate well with known geological and tectonic features in our study region. The decreasing group velocity with an increasing period in many regions indicates the presence of low velocity structures in the crust beneath Nepal and South Tibet. High group and phase velocities between MBT and STD could be associated with high crustal strength. The relatively low velocity at periods of 20-35 s over southern Tibet indicates the presence of thick crust at South Tibet.

We determined a high-resolution shear-wave velocity structure of the crust beneath the Nepal Himalaya by using a self-parameterized Bayesian approach. Our results show the presence of a low velocity layer in the shallow crust, which might indicate the sediments deposition in the upper crust of the Nepal Himalaya. The low velocity structure in the mid-crust at South Tibet, High- Himalaya, and South Nepal indicates the presence of either partial melt or aqueous fluids at high pore pressure. We successfully presented the high-resolution images of the MHT along the profiles which are perpendicular and parallel to the strike of 2015 Gorkha earthquake. The geometry of MHT reveals the double ramp along SW-NE direction. Our results also indicate the presence of weak mid-crust at South Tibet and strong mid-crust at High Himalaya. Our results show the presence of high velocity beneath the High Himalaya at a depth of 40-60 km (V_s=4.0-4.5 km/s), which could be evidence of partial eclogitization. The high velocity layer sandwiched between two low velocity layers at 10-15 km depth beneath Nepal and part of South Tibet could indicate the presence of an anisotropic layer. The shear wave velocity obtained across South Tibet shows the relatively low S-wave velocity in the crust up to 50 km which might indicates the presence of thicker crust in South Tibet than in Nepal. The shear wave velocity model along the collision between Indian and Tibetan plate shows the Indian plate subducting towards the Tibetan plate.

Chapter 3: Autocorrelation of Coda of Teleseismic P wave

Abstract

We present the application of autocorrelation of teleseismic P coda to recover shallow and deeper interfaces in the crust beneath Nepal and South Tibet. We used the data recorded by stations belongs to Hi-CLIMB and Hi-MNT network to compute the autocorrelograms. The autocorrelograms are equivalent to the records from the virtual source at the surface and reflection phases from the interfaces by the station on the surface. We inverted the reflection delay time of P and S-waves by using the existed velocity model across the study area to compute the depth of interface below a particular station. We successfully mapped the Moho below the station located in the South and North of MFT. The depth of Moho obtained by inverting two-way travel time of 2p and 2s phases is around 40 km in South of MFT and 48-70 km in North of MFT. We also recovered the interface between mid-crust and lower crust beneath High Himalaya and South Tibet at depth 40-60 km. We found upto 9 km thick sediments deposit in the South of MFT. Our results show the thickness of sediments decreasing from 9 km to 3 km while moving northward and MHT is flat in the South of MFT and deepening towards the North. The depth of MHT varies from 10-20 km within Nepal. The Moho in the South of MCT is flat and has a depth of around 40 km and deepens towards the North of MCT. The depth of Moho varies from 40-60 km within Nepal while moving from South to North. We also inverted the reflection delay time by using the local 1-D velocity model obtained by the Ambient Noise Tomography method to measure the depth of interfaces. We found that the depth of interface obtained from existed velocity model and the velocity model obtained by the Ambient Noise Tomography method are comparable.

Keywords: Autocorrelation, Teleseismic P wave coda, reflection delay time, interface, spectral whitening, Phase weighted stacking, S wave reflectivity, P wave reflectivity.

3.1 Introduction

The Himalaya-Nepal region hosts large earthquakes as a result of the collision between Indian and Eurasian plates (Molnar et al., 1993). Past studies suggest that large earthquakes in this region occur at the interface, which separates the subducting Indian plate from the Himalayas (Avouac et al., 2015; Bilham, 1995; Duputel et al., 2016; Elliott et al., 2016; Grandin et al., 2015; Lindsey et al., 2015; Martin et al., 2015; Sapkota et al., 2013). However, the exact geometry of such interface and other crustal discontinuities as well as the velocity/density structure below and above these discontinuities are poorly understood. Ruigrok & Wapenaar, 2012 studied the crustal interfaces beneath Himalayas and Tibet by using autocorrelation of global phases but their works especially focused Tibetan plateau. The variation of Moho depth in different locations beneath the Indian crust has been reported by Zhu and Kanamori, 2000. Schulte-Pelkum et al., 2005 also studied the discontinuities in Indian crust. They used time delay between direct and converted waves to estimate the depth of decollement and Moho depth in the crust beneath Nepal and South Tibet. Recently, the lateral variation of Main Himalayan Thrust (MHT) was studied from the local earthquake tomography method by Bai et al., 2019. They found that MHT deepens towards North-Northeast (NNE) parallel to the plate convergence direction as the Indian plate subducts beneath Tibet.

The information about the interior of the Earth comes from the variation of the seismic wave velocities with depth. The velocity of the seismic wave depends on the density as well as the elastic parameter which is the function of temperature, pressure, and the composition of the material. Inside the Earth, discontinuities separate media with different acoustic properties. Acoustic properties are defined in terms of the impedance which is simply the product of the seismic velocity and the density of the medium. Hence, the seismic discontinuities in the crust infer the variation of the seismic velocity and density of the structure. Once we know the elastic parameters, we can estimate the strength of the materials between crustal layers and can infer rheological properties in

the first order. For example, if the strength of the crustal layer is high, it is brittle and can host fractures, thus defining the seismogenic zone.

A detailed understanding of the crustal structure and geometry of discontinuities is crucial to improve earthquake locations and understanding seismic hazards in the region. The crust and upper mantle beneath Himalaya Nepal has extensively studied by receiver function method (e.g., Nábělek et al., 2009; Nelson et al., 1996; Schulte-Pelkum et al., 2005; Q. Xu et al., 2015). Hence, in this study, we are focusing on the imaging of the crustal discontinuities beneath the Himalayas of Nepal by using new technique (autocorrelation of the coda of P-wave) instead of the Receiver function method. Autocorrelation is the cross-correlation of the data with itself. The use of the autocorrelation technique has recently emerged as a powerful imaging tool for mapping crustal and upper mantle structures (Kennett, 2015). The autocorrelation approach promises to provide new information on the P wave structure of the shallow Earth's interior that is different from the S wave structure recovered by receiver function. Hence, the autocorrelation of the P wave coda can be used in conjunction with the receiver function technique to increase constraints on the crust.

An improved autocorrelation method (Pham & Tkalcic, 2017) uses a part of seismograms recorded by stations corresponding to earthquakes after P wave arrivals, namely, the P wave coda (Paulssen et al., 1993), to image the interface below a particular station. The approach relying on earthquakes has three major advantages over ambient noise. First, the incidence of P waves arriving from teleseismic earthquakes is near vertical, so it facilitates the extraction of desired vertical reflectivity (Ruigrok & Wapenaar, 2012; Sun & Kennett, 2016). Second, the computation cost is significantly smaller in the case of coda processing. Third, body waves from teleseismic earthquakes generally have richer content in a high-frequency band than ambient noise data which provides the higher resolution of relatively shallow seismic discontinuities. Pham and Tkalcic, (2017) used the P wave coda autocorrelation to map the shallow discontinuities as well as to retrieve Moho (Pham

& Tkalcic, 2017, 2018). Their work motivates us to use reflection signals to map the discontinuity in the crust beneath Himalaya Nepal by using improved autocorrelation method.

3.2 Data and Methodology

3.2.1 Theory

Seismic waves from distant earthquakes arriving at seismic stations propagate near vertically and are reflected by the free surface and so propagate downward, subsequently being reflected back upwards again by discontinuities beneath the station. Once, we have the data from a station, we can convert the coda wave train to reflectivity record using the autocorrelation technique.

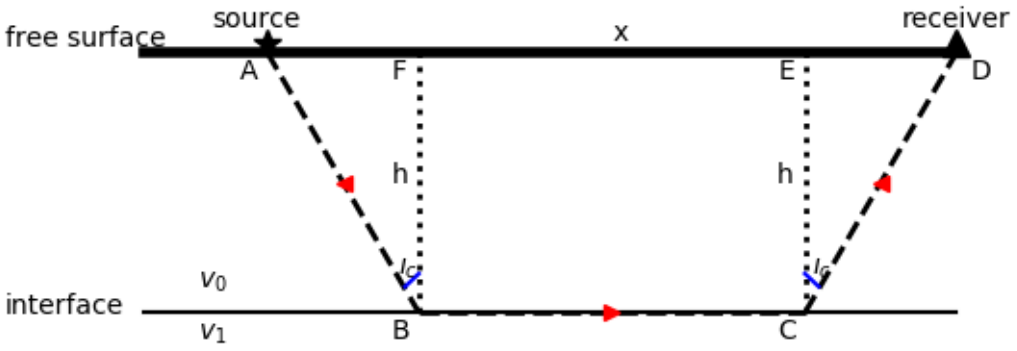

Figure 3.1: schematic representation of the refraction seismology.

Let us consider that the source and receiver are both placed on the free surface and there is an interface at depth h and the distance between source and receiver is x as shown in figure (3.1). Let us consider i_c as the angle of the incident wave, v_0 and v_1 are the velocities of the different layers. Let us say T is the travel time to reach the receiver from the source.

$$AB = \frac{h}{\cos i_c}$$

$$CD = \frac{h}{\cos i_c}$$

$$AF = h\tan i_c$$

$$DE = h\tan i_c$$

$$BC = AD - AF - DE = x - h\tan i_c - h\tan i_c = x - 2h\tan i_c$$

$$T = \frac{AB}{v_0} + \frac{BC}{v_1} + \frac{CD}{v_0} = \frac{2h}{v_0 \cos i_c} + \frac{x}{v_1} + \frac{2h\tan i_c}{v_1} = \frac{x}{v_1} + \frac{2h}{\cos i_c}\left(\frac{1}{v_0} - \frac{\sin i_c}{v_1}\right)$$

$$T = \frac{x}{v_1} + \frac{2h}{\sqrt{1-\frac{v_0^2}{v_1^2}}}\left(\frac{1}{v_0} - \frac{v_0}{v_1^2}\right) = \frac{x}{v_1} + \frac{2h}{\sqrt{v_1^2 - v_0^2}}\left(\frac{v_1^2 - v_0^2}{v_1^2 v_0}\right)$$

$$T = \frac{x}{v_1} + 2h\sqrt{\frac{1}{v_0^2} - \frac{1}{v_1^2}} \qquad (3.1)$$

If the angle of incidence is 90^0 and for the flat layer, the ray-parameter is simply the slowness at the point of incidence. When the angle of incidence is 90^0, then x=0. So, the above equation modified as:

$$T = 2h\sqrt{\frac{1}{v_0^2} - \beta^2} \qquad (3.2)$$

To demonstrate the feasibility of exploiting the autocorrelation of the coda of the first P arrival from distant earthquakes to recover the discontinuities (having epicentral distance in the range $30^0 - 95^0$), we generated an impulsive seismogram by using reflectivity code (B. Kennett, 1983). The result of our autocorrelation is a symmetric pulse. In our work, we need only the positive offset (causal), so we took the one-sided autocorrelogram. A general feature of autocorrelogram is that the large peak corresponds to zero delay time. The large central pulse is suppressed by using the taper function. We performed autocorrelation of both vertical and radial components of the seismogram. The first prominent peak in the vertical and radial autocorrelogram corresponds to the 2p and 2s phase, respectively. The 2p phase in autocorrelogram is formed from all pairs having the same time difference with the transmitted phase 1p and reflection 3p. The schematic representation of different phases that appear in impulse response is shown in figure3.2.

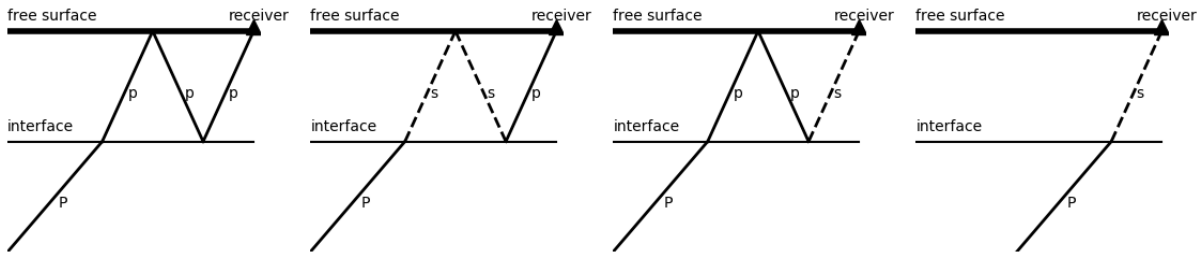

Figure 3.2: Schematic representation of first order reverberations for a homogeneous layer above a half space.

In figure3.2, we tested different homogeneous layers above the half-space with different properties. The incident wave is P, and the receiver is placed at the surface which records an impulsive compressional plane wave arriving near vertically. The upcoming P- waves beneath the seismic stations will generate P- to -S converted phases at sharp interfaces below the receiver. When the P wave incident on the interface, it splits into P and SV waves. Spitted P wave reach the receiver as the first arrival P while the SV wave is recorded on the receiver as 1s phase. If the spitted P wave is reflected by the free surface and again reflected by the interface it reaches to the receiver as a 3p phase. While the reflected p wave incident on the interface there will be mode conversion also which makes 2p1s phase. If spitted s wave reflected from the free surface which again reflected from the interface and reaches to the receiver becomes 3s phases. While the s wave incident on the interface there will be mode-conversion also which makes 1p2s phase. We can see the schematic representation of all the explained phases in figure3.2.

The 2p phase in autocorrelogram is formed from all pairs having the same time difference with the transmitted phase 1p and reflection 3p. The reflection delay time for the 2p phase is given by;

$$\Delta t_{2p} = t_{3p} - t_{1p} = 2H\sqrt{\frac{1}{v_p^2} - \beta^2} = 2H\eta_p \qquad (3.4)$$

The 2s phase in autocorrelogram is formed from all pairs having the same time difference with the transmitted phase 1p and reflection 1p2s as shown in figure3.2.

Hence, the reflection delay time for the 2s phase is given by;

$$\Delta t_{2s} = t_{1p2s} - t_{1p} = 2H\sqrt{\frac{1}{v_s^2} - \beta^2} = 2H\eta_s \quad (3.5)$$

Where V_p and V_s are the velocities of P- and s-wave, β is the ray parameter, η_p and η_s are the vertical and radial slowness, H is the depth of the discontinuity. If we ignore the ray parameter, then it becomes simple velocity formula in which the wave covers the distance 2H, and the time taken is equaled to reflection delay time. From vertical and radial autocorrelogram, we will get the reflection delay time of 2p and 2s phases and we simply invert the reflection time to a depth of the discontinuity by using equations 3.4 and 3.5.

3.2.2 Data selection and processing

We downloaded data from IRIS which were recorded by stations belongs to Hi-CLIMB (Nabelek, 2002) and Hi-MNT (A. Sheehan, 2001) network in the period from 2001-10-06 to 2004-04-10. We considered the waveform which has the signal 200 s after P arrival and 25 s before P arrival. The onset of P arrival is inspected on the vertical seismogram and the time of arrival is calculated using Taup, which needs depth and epicentral distance of the event. We rotate the north-south and east-west horizontal component seismograms into radial and transverse components, respectively. Since, we are looking for isotropic discontinuities, we just need vertical and radial components. The transverse component is considered if we are interested to map the anisotropic discontinuities.

We extracted P wave coda from events with Mw>5.5 and the epicentral distances in the range 30^0 -95^0. We selected this range because the P phase is well separated from other phases. For epicentral distances greater than 95^0, it is difficult to separate the coda of P wave from PcP waves. We used stations located in the southern part of Nepal. The reason behind this choice is that flat-layer approximation is valid in this region and our main aim here is to map the isotropic discontinuities. Later, we also considered stations located in High Himalayas and South Tibet to map the deeper interfaces. In

this work, we make use of the data from the Hi-CLIMB array and Hi-MNT network to recover the shallow, mid-crustal, and deeper interface beneath the seismic stations. All the earthquakes recorded by station H0010 is shown in figure3.3.

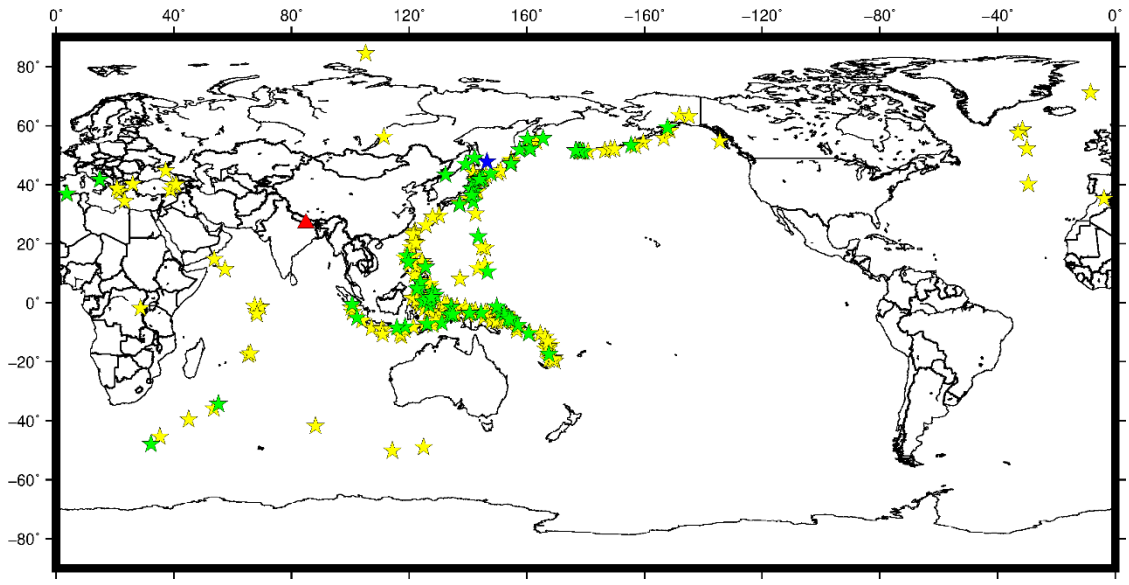

Figure 3.3: Location of station H0010 (belongs to Hi-CLIMB network) and the location of all the teleseismic (30-95^0) earthquakes recorded by it. Green stars show the location of earthquakes which are selected for further study based on SNR and yellow stars indicate the earthquakes recorded by station H0010 which are discarded.

The data were selected based on SNR around the P wave arrival. We selected the data by visual inspection of both radial and vertical seismogram. Since we considered teleseismic P coda wave, vertical seismograms were selected more than radial ones. As the vertical component is more sensitive to the P wave than the radial component. For example, our selection procedure selected 70 vertical and 37 radial seismograms in the teleseismic data set for station H0010. All the earthquakes that were recorded in station H0010 are shown with a yellow, green, and blue star in figure3.15. The blue star represents the earthquakes that were chosen to show the processing steps above. The green stars are the one which was selected in this study.

While selecting the data, a possible concern might be related to the source-side arrivals of depth phases after the arrival of the P wave. Usually, depth phases carry the information of prominent reflectors near the hypocenter and might cause ambiguities

in the interpretation of the discontinuities beneath the receiver. In our study, we roughly avoid this possibility by rejecting those waveforms which have visually recognizable surface reflection pP. There might be a probability of the presence of hidden depth phases in the waveform which could be amplified by the whitening as the receiver-side signals do. If the hidden pP exists in the coda waveform, the delay and polarity vary as a function of hypocentral depth as well as source surroundings. Therefore, to mitigate the ambiguities coming from source-side signals, we should consider earthquakes that cover a wide diversity of depths and geological structures so that the incoherent source-side signals will cancel destructively, and the coherent receiver-side signals will emerge from the noise. If we use a limited number of earthquakes concentrated in a specific region, there might be an issue with the source-side signal. In our study, most selected earthquakes originate from $0\text{-}360^0$ azimuth to the receiver. Most of the earthquakes have a hypocentral depth greater than the interface under the receiver. Therefore, we could get recovered signals that are free from the potential ambiguities caused by hidden source-side signals.

We cut the signal 10 s before and 35 s after the P arrival and remove the mean and trend from the seismogram. We applied frequency band 0.15-1.0 Hz to recover deeper interfaces and 0.5-3.5 Hz to recover shallow interfaces. The passband of the instrument is 0.01-10 Hz, so it is not necessary to make instrument correction in our applications as the instrument response only serves as a scaling factor and does not perturb the autocorrelogram (e.g., Gorbatov et al., 2013). We then performed a fast Fourier transform (FFT) of the signal. Before that, we padded zero so that the length of the seismogram becomes double the original length to avoid the aliasing effect. After FFT, to enhance the higher frequency content and lowers the lower frequency content in the signal, we applied spectral whitening. The spectral whitened spectrum is obtained by dividing the amplitude spectrum by smoothened average of the spectrum. Finally, we computed the autocorrelation of spectrally whitened data. In the frequency domain, convolution operation requires that phase spectrums be added together, whiles for the correlation operation, the phase spectrums are subtracted from one another. In both

cases, the amplitude spectrums are multiplied. For autocorrelation operation, the phase spectrums of both the signals are the same, so the autocorrelation retains the amplitude information of the response function but cancels the phase. Hence, we computed the autocorrelation by taking the square of absolute amplitude spectrum, and to get the autocorrelation in the time domain, we applied Inverse Fast Fourier Transform (IFFT).

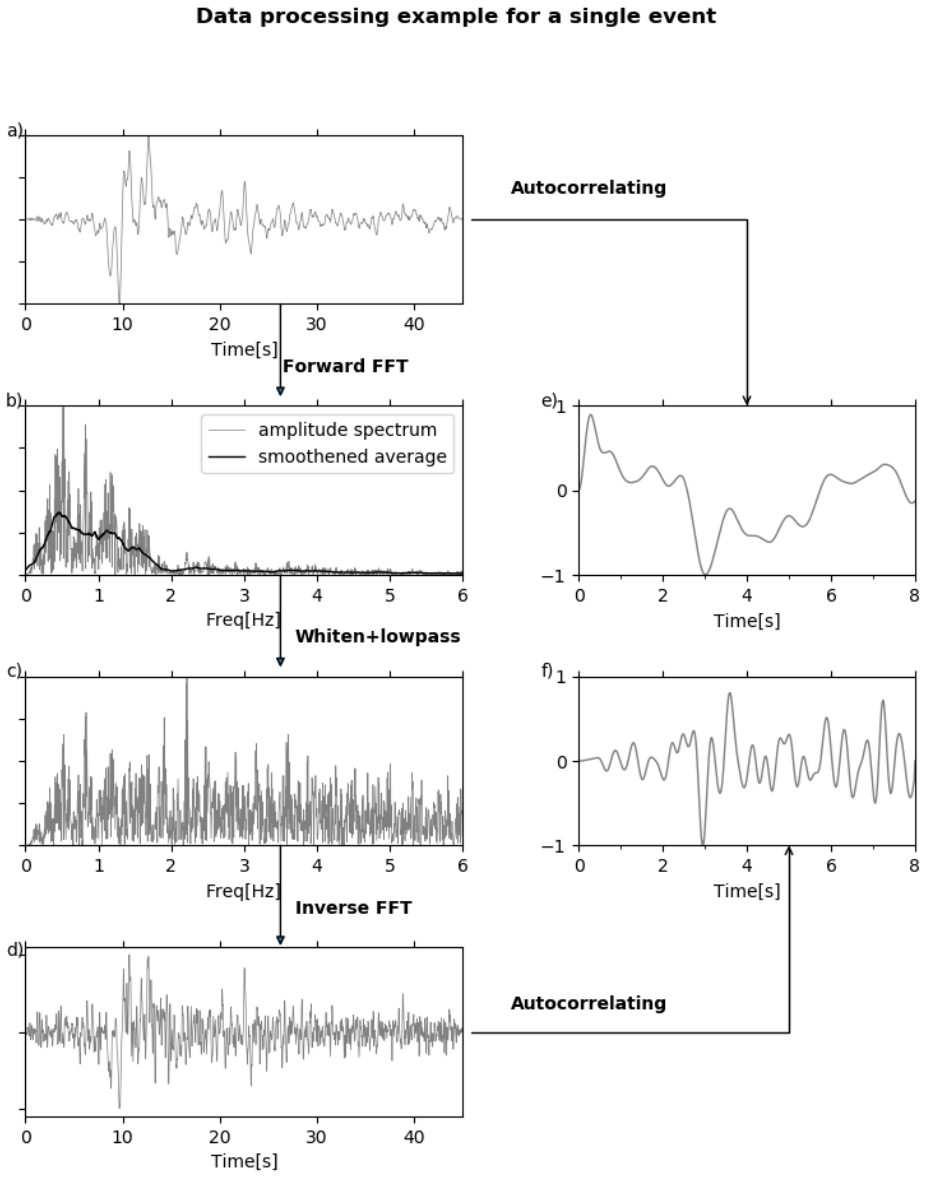

Figure 3.4: a) Short vertical seismogram of earthquake of 7.3Mw on 17 November 2002 (146.45^{0}E, 47.81^{0}N) recorded by station H0010 located over the sediments on Southern part of Nepal. b) Original amplitude spectrum and its smoothened average. c) Whitened amplitude spectrum after applying lowpass filter. d) Whitened seismogram in time domain. e) One sided tapered autocorrelogram of original seismogram. f) One sided tapered autocorrelogram of whitened seismogram.

The autocorrelation of the whitened signal is band-pass filtered to improve the

sharpness of the reflection phases and to avoid the spurious effect caused by the unexpected amplification of very high-frequency noise due to spectral whitening. In the last step, to enhance the SNR of the reflection signals and suppress the incoherent features such as the effect of the source time functions, earthquake depth phases, and source side scattering, we stacked the autocorrelation of individual event by using phase weighted stacking method (Pham & Tkalcic, 2017; Schimmel & Paulssen, 1997).

3.2.3 Synthetic Experiment

We performed some synthetic tests to validate the methodology. By doing this experiment, we would like to understand the phases which could be practically recovered from the P wave coda autocorrelation and their polarities. We are also interested to know whether the reflection delay time depends on the ray parameter or not. The other purpose of doing the synthetic test is to see the effect of different frequency widths applied during spectral whitening and the length of seismogram required to recover the discontinuities at different depths. We created a typical Earth model for a particular station located over a sedimentary basin. The model consists of 5 km thick sediments over half-space. The velocity of P-wave, S-wave, and density are 5 km/s, 2.5 km/s, and 2.25 g/cm^3 respectively in the layer above the half-space. We have computed the complete seismograms (both vertical and radial) for a station on the top of the horizontally stratified structure bounded by a free surface. As the event distance is much larger than the extent of the local structure of interest, we simulate the teleseismic wavefronts as plane waves, which illuminates the local structure from below at different incident angles. There are three steps to generate the complete synthetic seismogram. The first is to produce the temporal impulse response of the local structure for the incident wave (P wave in our case), the second is to produce the source with random frequency and the third is to produce the random noise.

3.3.3.1 Design of Synthetic Seismogram

To produce the impulse response, we used the reflectivity code (respknt) of Randall (Randall, 1989). The code used the reflection and transmission matrix methods developed by Kennet (B. Kennett, 1983). We have converted the epicentral distance to ray-parameter by using the udtdd code (Herrmann, 2013). The ray-parameter is used as inputs to control the incident angles of the incident wave. Other inputs are the velocity model, type of incident wave (P or S wave), duration of the impulse response, and type of conversion (partial or full). In our case, we have used the full conversion so that we could have all the reflected phases in the impulse response.

We considered the Ricker wavelet as a synthetic source which is produced by using equation 3.6:

$$y = 1 - 2\pi^2 f^2 t^2 e^{-\pi^2 t^2 f^2} \quad (3.6)$$

Where f is the frequency of waveform while t is the time. We created the source with period ranges from 1 to 10 s.

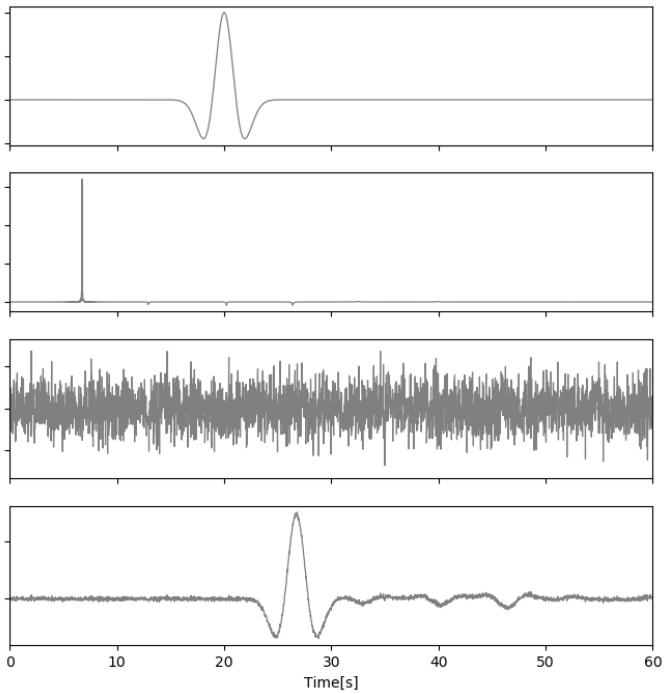

Figure 3.5: source, impulse response, random noise and complete synthetic seismogram from top to bottom.

To add noise in the synthetic seismogram, we produced the random noise with a mean

0 and standard deviation of 0.2. We set the standard deviation value lower to maintain the good SNR ratio, otherwise, the noise will dominate the signal. Finally, we convolved the source with the impulse response and added noise to the convolved result to achieve the complete seismogram.

Seismogram = source ⊛impulse response + noise (3.7)

In this way, we computed the complete synthetic seismogram (both radial and vertical) and the process is repeated for all sets of epicentral distance range from 30 to 95^0. Figure3.5 shows the plots of all the steps used to compute synthetic seismogram.

3.2.3.2 Impulse response and its autocorrelation

To understand the phases which could be recovered from the teleseismic P coda autocorrelation and their polarities, we performed the autocorrelation of the synthetic impulse response as shown in figure3.6.

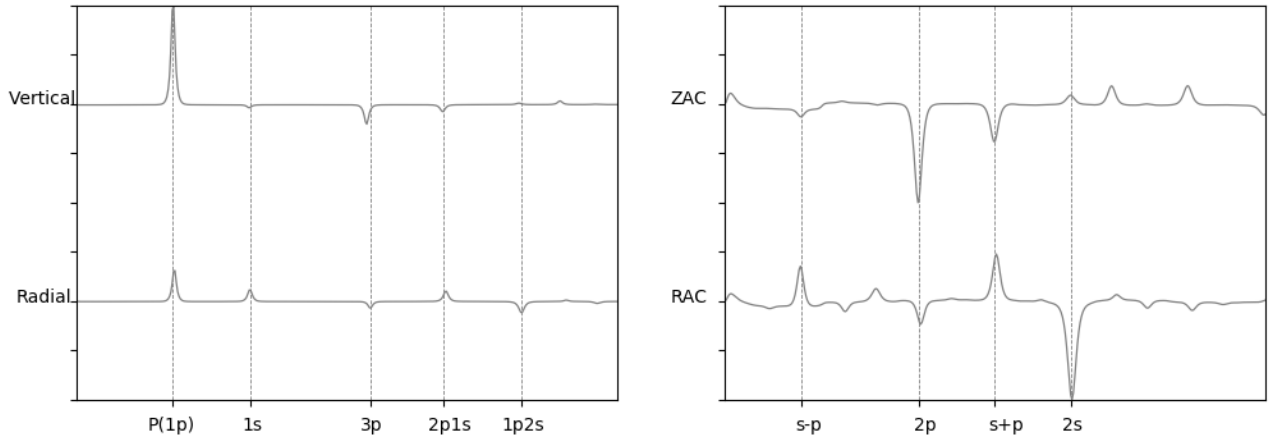

Figure 3.6: Vertical (top) and radial (bottom) component of impulse response (Left), vertical and radial autocorrelation of respective impulse response (Right).

We see the polarity of 1s, 3p, and 2p1s phases are opposite to the polarity of P while 1p2s has the same polarity in the vertical component. In the radial component, 1s and 2p1s have the same polarity as P while 3p and 1p2s have opposite polarity. The polarity of the phases changed once it is reflected from the free surface. In the autocorrelation of the vertical component of the impulse response, we see that s-p, 2p, s+p phases have

negative polarities whiles the 2s phase has positive polarity. In contrast, for the redial component, we can see s-p and s+p phases have positive polarities while 2p and 2s phases have negative polarities. Observing the autocorrelation of the vertical and radial components of the impulse response in detail, we notice that the 2p phase is prominent in the vertical component while the 2s phase is prominent in the radial component. This implies that autocorrelation favors reflection phases (2p and 2s) which is different from the P wave receiver function which favors the mode-conversions phases (s-p and s+p).

3.2.3.3 Synthetic test for input parameters

We performed a synthetic experiment by using synthetic seismogram to verify whether the reflection delay time depends on the ray parameter or not. The reflection delay time of 2p and 2s phases in the stacked autocorrelation is shown in figure3.7.

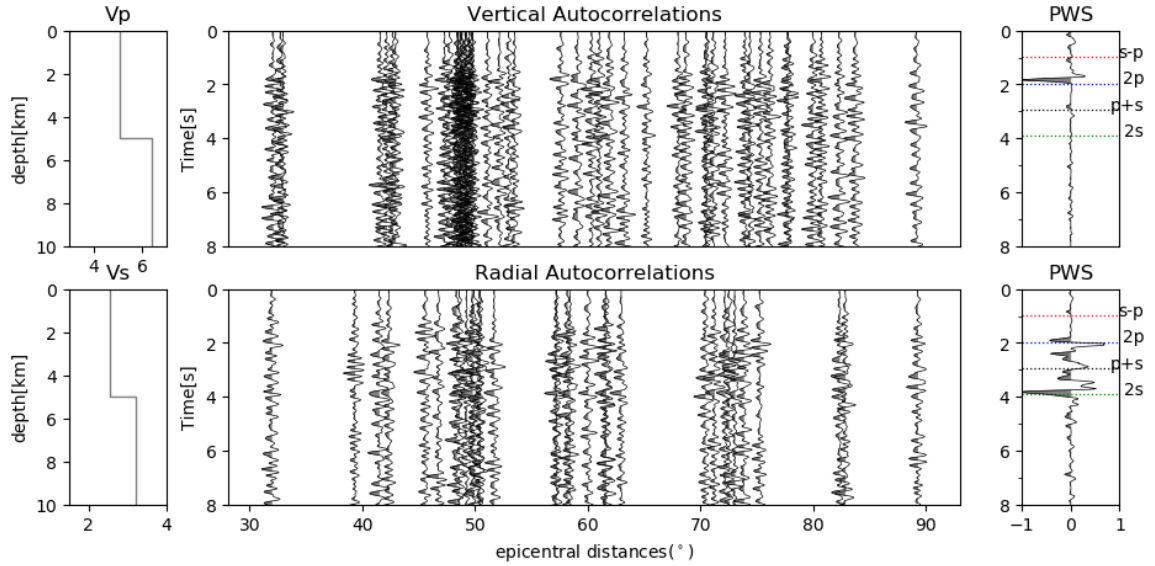

Figure 3.7: Synthetic experiment demonstrating the independence of delay time with ray-parameter. Input 1D velocity model P (top left) and S (bottom left) waves, one sided autocorrelogram of individual vertical (top middle) and radial (bottom middle) seismograms and as function of epicentral distance, one sided phase weighted vertical (top right) and radial (bottom right) stacked autocorrelogram.

In phase weighted stacked autocorrelogram (Fig3.6), we can see the dotted lines which are plotted at delay times of s-p, 2p, s+p, and 2s phases. These delay times are

computed by using the P and S wave velocities from the input model and we did not consider the ray parameter while computing the delay time. We can see the delay time of the 2p phase in vertical and 2s phase in radial stacked autocorrelogram exactly matches the theoretical delay time. Hence, we can say that the delay time of reflected phases is independent of the ray-parameter. We can convert the delay time of 2p and 2s phases to the depth of interface by using the input velocity model. This experiment also shows the capability of the P wave coda autocorrelation technique to recover shallow discontinuity.

To understand the performance of the P coda autocorrelation technique at different frequency widths, firstly we created a velocity model with Moho at depth 50 km and only one layer above the half-space bounded by a free surface. The average velocity of P and S-wave are 6.40 km/s and 3.70 km/s respectively in the layer above half-space. We generated the synthetic seismogram using that velocity model and vary the frequency width from 0.05 Hz to 0.40 Hz and observed the vertical and radial phase weighted stacked autocorrelogram which is shown in figure3.8.

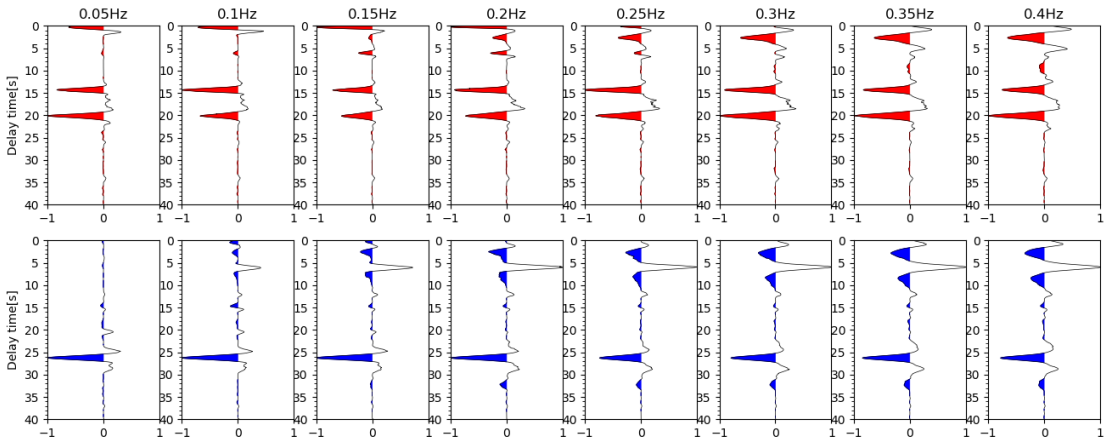

Figure 3.8: comparison of the performance of several whitening–window widths. Top panel is for vertical component while bottom one is for radial component. The frequency width is mentioned in top of every plot.

We can see a prominent peak around 14.5 s and 26.2 s in vertical and radial phase weighted stacked autocorrelogram, respectively. We expected delay time of 2p and 2s phases 15.6 s and 27 s which are close to the delay time we see in the phase weighted

stacked vertical and radial autocorrelograms. From the visualization, we can see the best result is obtained at frequency width 0.10 Hz though we see the expected phases appear for all the frequency width tested.

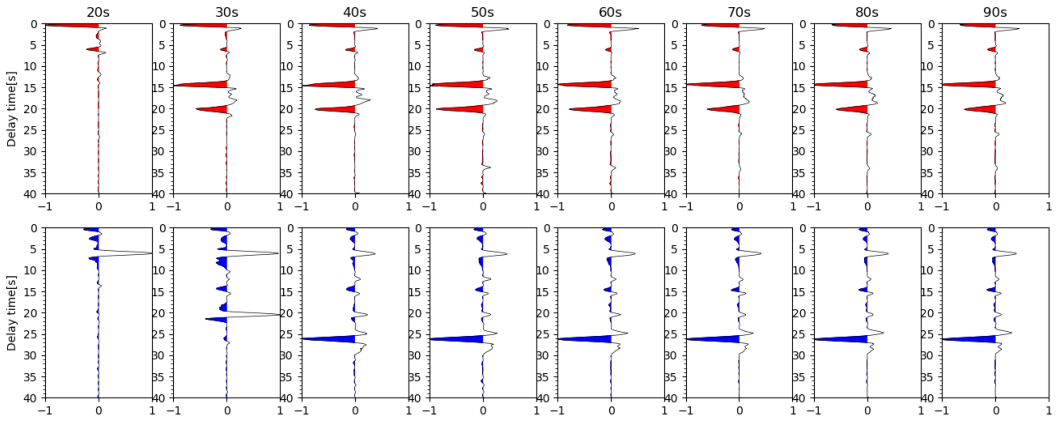

Figure 3.9: comparison of the performance with several length of signal after P arrival. Top panel is for vertical component while bottom one is for radial component. The duration of signal after P wave is mentioned in top of every plot.

To understand the length of seismogram required to recover the discontinuities at different depths, we set the frequency width to 0.10 Hz and vary the length of the signal after P wave arrival from 20 s to 90 s and observed the vertical and radial phase weighted stacked autocorrelograms, for example as shown in figure3.9. We could not see the 2p and 2s phases if we take a 20 s signal after P wave arrival. 2P phases start to appear when the signal duration is more than or equal to 30 s while 2s phases start at 40 s. We can see a prominent 2p phases appear when we take the signal duration of 70 s. This experiment suggests the requirement of a longer record length if we are interested to recover a deeper interface.

Now we fix the frequency width to 0.10 Hz and the length of the signal as 70 s and performed an experiment to see the feasibility of using the P coda wave autocorrelation technique to recover a deeper interface (see Fig 3.10). Here, we set an interface at 50 km depth. In phase weighted stacked autocorrelogram, we can see the dotted lines which are plotted at delay times of s-p, 2p, p+s, and 2s phases. These delay times are computed by using the P and S wave velocities from the input model. We can see the delay time of the 2p phase in vertical and 2s phase in radial stacked autocorrelograms

are very close to the theoretical delay time which is an indication that the autocorrelation technique is able to pick up reflections from the deeper interface.

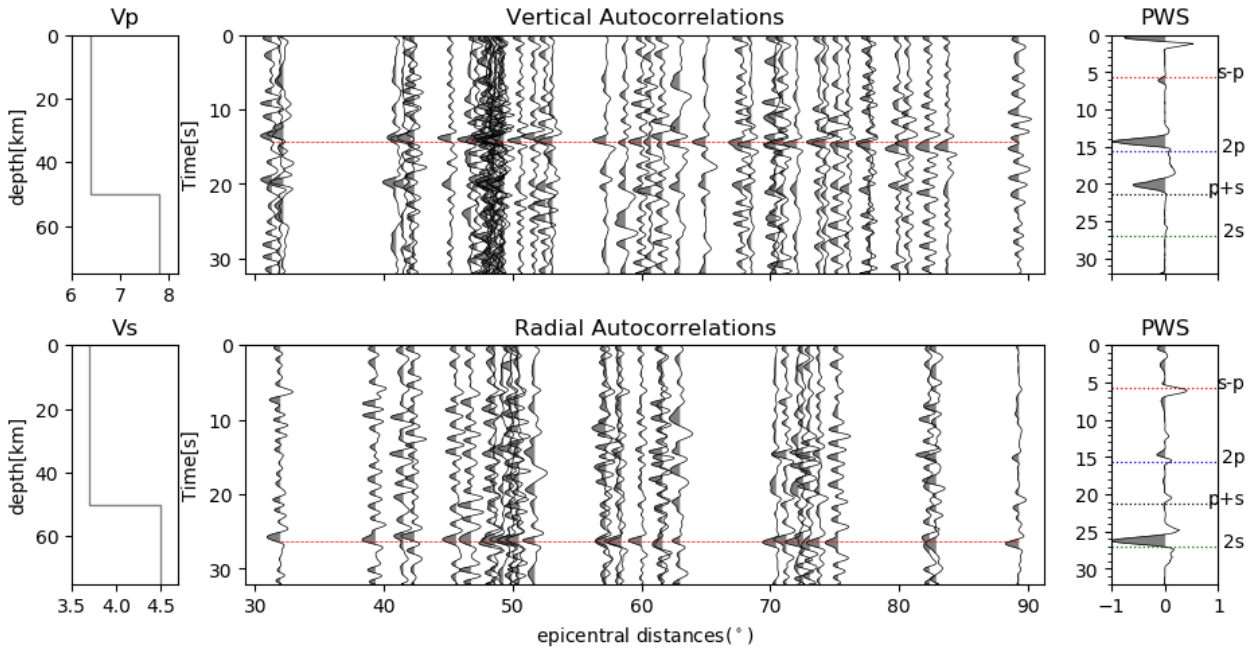

Figure 3.10: Synthetic experiment demonstrating the feasibility of P coda wave autocorrelation technique to recover deeper interface. Input 1D velocity model P (top left) and S (bottom left) waves, one sided autocorrelograms of individual vertical (top middle) and radial (bottom middle) seismograms and as function of epicentral distance, one sided phase weighted vertical (top right) and radial (bottom right) stacked autocorrelogram.

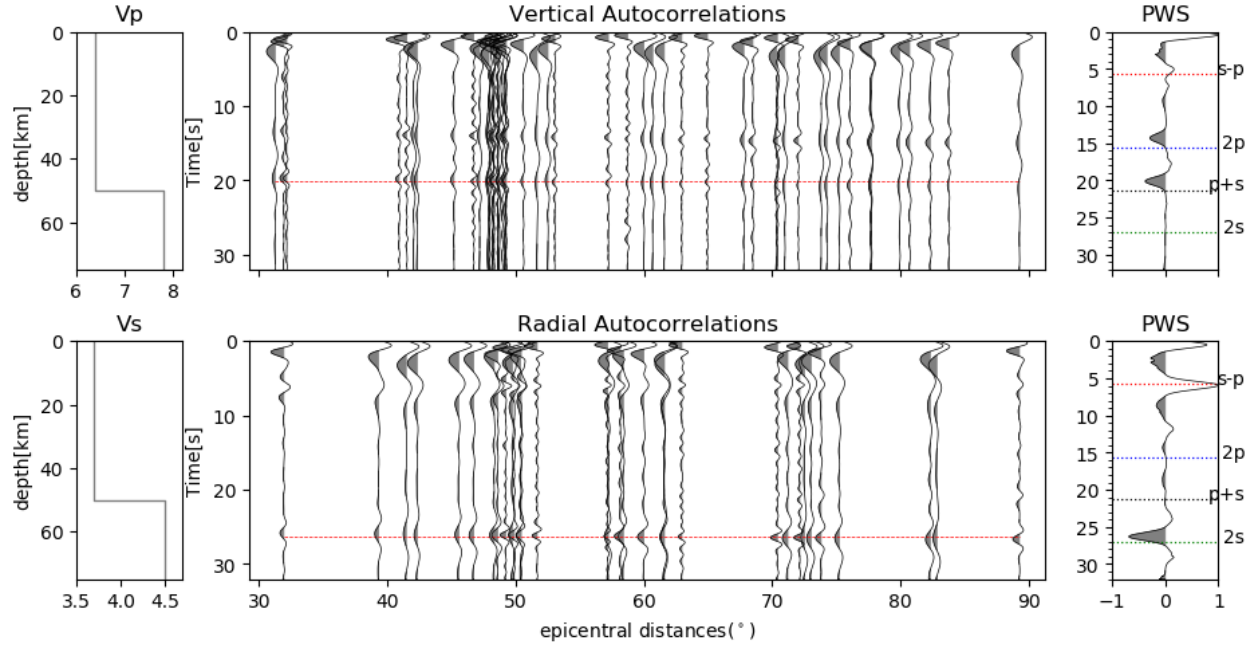

Figure 3.11: Input 1-D velocity model P (top left) and S (bottom left) waves, one sided autocorrelograms of individual vertical (top middle) and radial (bottom middle) seismograms and as function of epicentral distance, one sided phase weighted vertical

(top right) and radial (bottom right) stacked autocorrelogram.

We also saw the significance of using the spectral whitening before autocorrelation of the signal. All the results presented above were obtained by using spectral whitening. The experiment performed without using spectral whitening is shown in figure3.11. If we compare the figure3.11 and figure3.10, we can see the 2p and 2s phases are prominent and sharper in the case where we used spectral whitening. This experiment shows the significance of whitening to recover the phases in the stacked autocorrelogram.

In the above experiment, we set only one interface in the input velocity model. Now, we set three interfaces in the input model. The used input velocity model is shown below in table.

Interface	Depth (km)	V_p (km/s)	V_s (km/s)	Density (g/cm^3)
1	5	5.0	2.9	2.25
2	20	5.5	3.2	2.50
3	50	5.9	3.4	2.80
4	0	7.2	4.2	3.20

The expected delay time of 2p phases corresponding to the first interface is denoted by $2p_1$, the second interface is denoted by $2p_2$, and the third interface is denoted by $2p_3$ in the vertical phase weighted stacked autocorrelogram. The expected delay time of 2s phases corresponding to the first interface is denoted by $2s_1$, the second interface is denoted by $2s_2$, and the third interface is denoted by $2s_3$ in the vertical phase weighted stacked autocorrelogram. Using the information from the previous one-layer over half-space test, we use a 70 s signal and set the frequency with to 0.10 Hz. Figure 3.12 shows the result for the 3-layer of half-space experiment. Here, we see a prominent peak in the phase weighted vertically stacked autocorrelogram very close to the

theoretical delay time of 2p phases corresponding to the third interface and in phase weighted radial stacked autocorrelogram the prominent peak is around the theoretical delay time of 2s phases corresponding to the third interface.

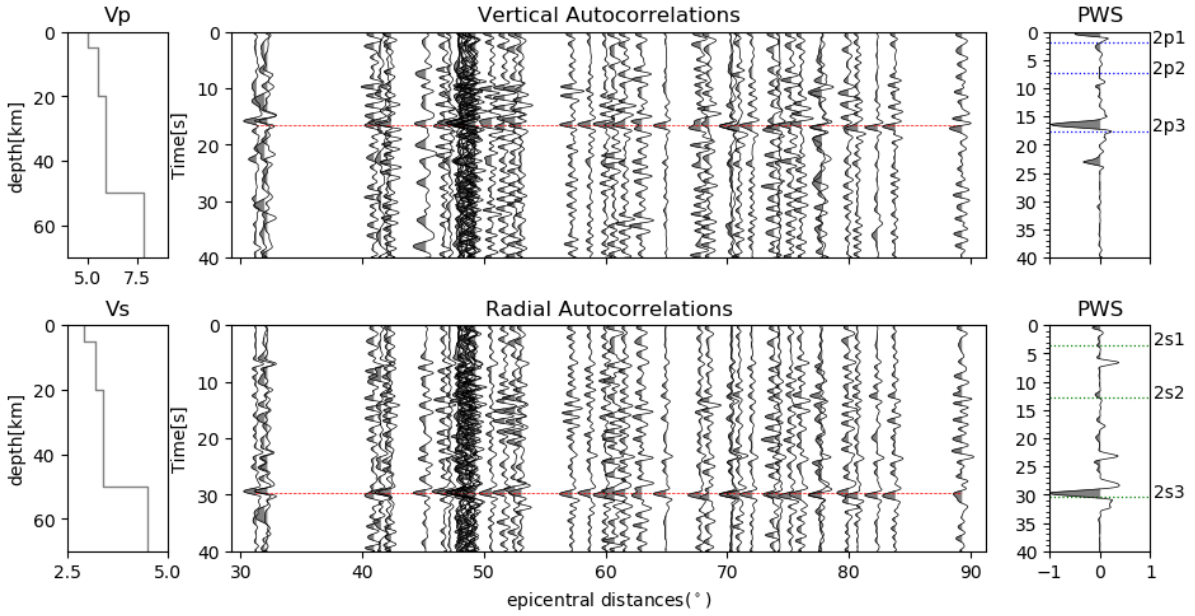

Figure 3.12: Input 1-D velocity model P (top left) and S (bottom left) waves, one sided autocorrelograms of individual vertical (top middle) and radial (bottom middle) seismograms and as function of epicentral distance, one sided phase weighted vertical (top right) and radial (bottom right) stacked autocorrelogram.

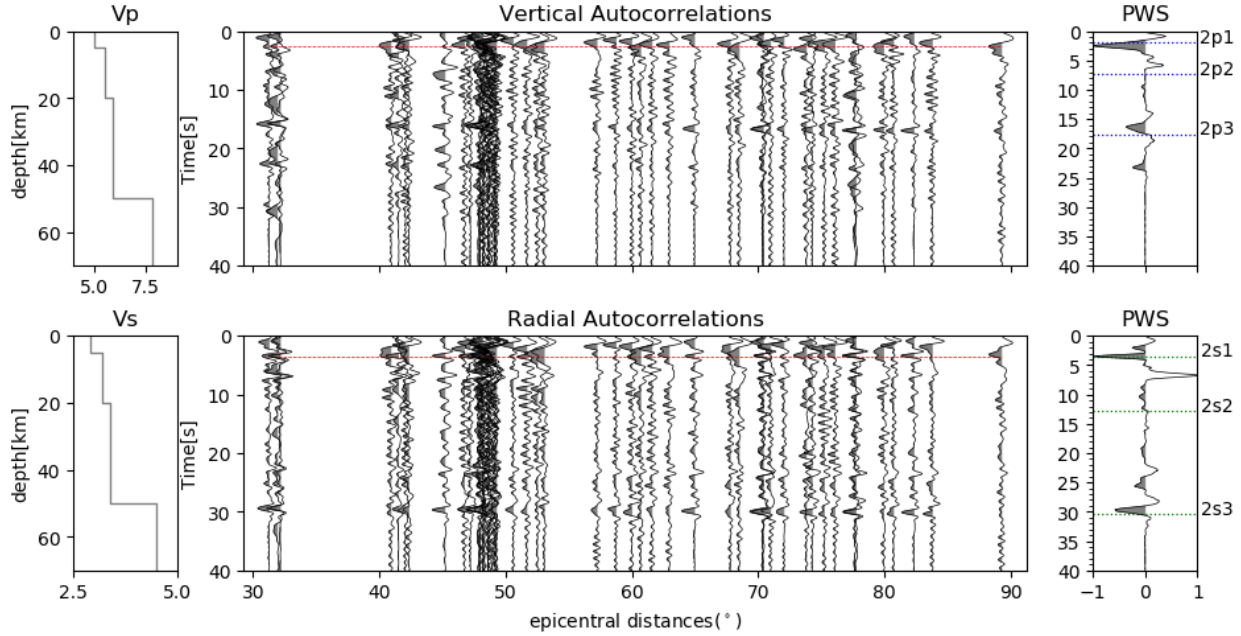

Figure 3.13: Input 1-D velocity model P (top left) and S (bottom left) waves, one sided autocorrelograms of individual vertical (top middle) and radial (bottom middle) seismograms and as function of epicentral distance, one sided phase weighted vertical (top right) and radial (bottom right) stacked autocorrelogram.

To recover the shallow interface, we took a 40 s long signal after P arrival and set the frequency width to 0.35 Hz. The result obtained is shown in figure3.13. We can see the prominent peak in phase weighted vertically stacked autocorrelogram very close to the theoretical delay time of 2p phases corresponding to the first interface and in phase weighted radial stacked autocorrelogram the prominent peak is around the theoretical delay time of 2s phases corresponding to the first interface.

In the above experiment, we have applied a zero-phase bandpass filter to improve the sharpness of reflection signals. We used a bandpass filter to remove very long period signals and very high-frequency noise due to spectral whitening. To see the effect of different bandpass filters while recovering shallow interface (5 km), we perform an experiment where we vary the higher frequency corner from 1 to 5 Hz. The result is shown in figure3.14. In this case, the expected the delay time of the 2p phase is 2.3 s and the 2s phase is 4.0 s. When we see the vertical and radial phase weighted stacked autocorrelograms, we can see the prominent peak is around 2.3 s in vertical and 4.0 s in a radial component when the higher corner frequency is more than or equal to 3 Hz indicating that high-frequency signals are required to image shallow interfaces.

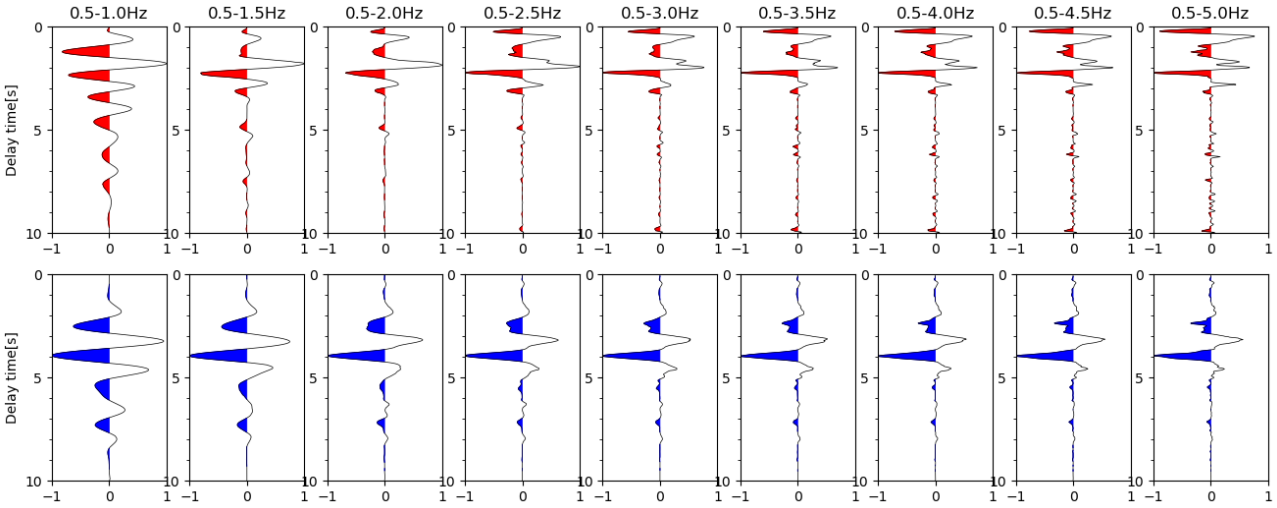

Figure 3.14: comparison of the performance with several ranges of corner frequency of bandpass filter. Top panel is for vertical component while bottom one is for radial component. The range of frequency is mentioned in top of every plot.

The effect of applying different bandpass filters on the autocorrelated waveforms can be observed in figure3.15, where we vary the lower corner frequency from 0.05 to 0.5 Hz and higher corner frequency from 0.7 to 2 Hz. In this case, we expected the delay time of the 2p phase is 15.6 s and the 2s phase is 27.0 s. When we see the vertical and radial phase weighted stacked autocorrelogram, we can see the prominent peak around 15 s in vertical and 26 s in a radial component when the higher corner frequency is 0.7 Hz and lower corner frequency is less than or equal to 0.15 Hz. This indicates the necessity of a lower frequency signal to image the deeper interfaces.

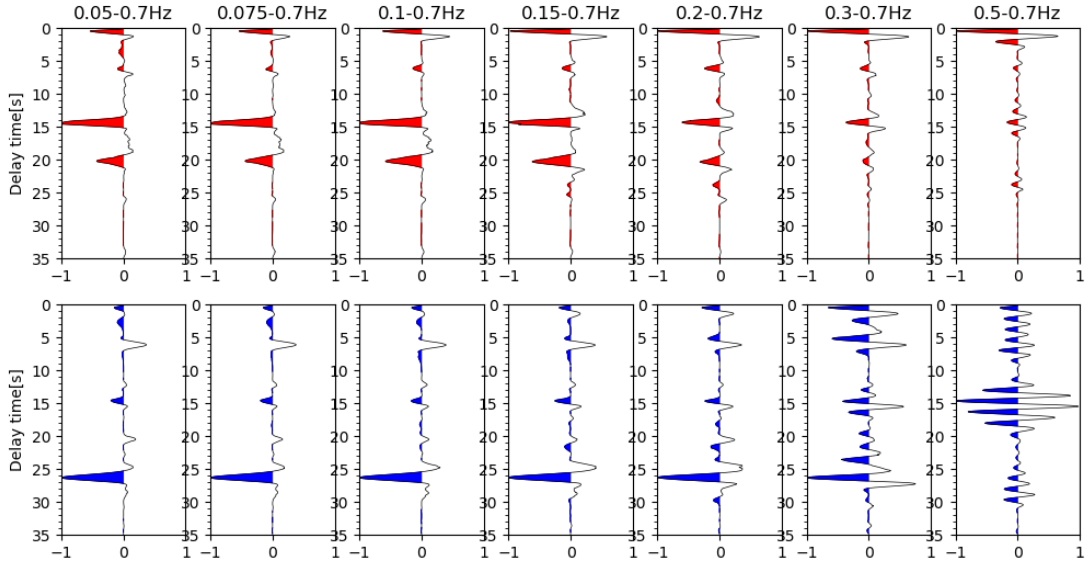

Figure 3.15: comparison of the performance with several ranges of corner frequency of bandpass filter. Top panel is for vertical component while bottom one is for radial component. The range of frequency is mentioned in top of every plot.

3.2.4 Selection of Spectral Whitening Width

3.2.4.1 Synthetic data

One way to select whitening width is a visual inspection of stacked autocorrelation by varying the spectral whitening width which is shown in figure3.8. We can also select spectral whitening width from the resonance patterns recovered in a linear stack of whitened power spectra. In this method, we computed the linear stack of power spectra as function of different frequency width. We validated this method from a synthetic test. The synthetic seismograms are generated with input model that consists of 8 km thick sediments over half-space. We consider the velocity of P-wave, S-wave, and

density as 5.30 km/s, 2.7 km/s, and 2.35 g/cm^3 respectively in the layer above the half-space.

We observed the resonance pattern in linearly stacked power spectra in vertical as well as the radial component when spectral whitening widths are larger than or equal to 0.20 Hz. The space between resonance peaks in the vertical component and radial components are nearly 0.32 Hz and 0.17 Hz, respectively. The two-wave travel time of 2p and 2s phases for a structure having an 8 km layer with P-wave and S-wave velocity 5.30 km/s and 2.7 km/s are nearly 3 s and 6 s. Thus, the spacing of resonance peaks in vertical component and radial component is equivalent to reciprocal of vertical and radial two-way travel time. Empirically, whitening width is selected in the range between one or two times of resonance gap observed in the linear stack of whitened spectra (Pham & Tkalcic, 2018).

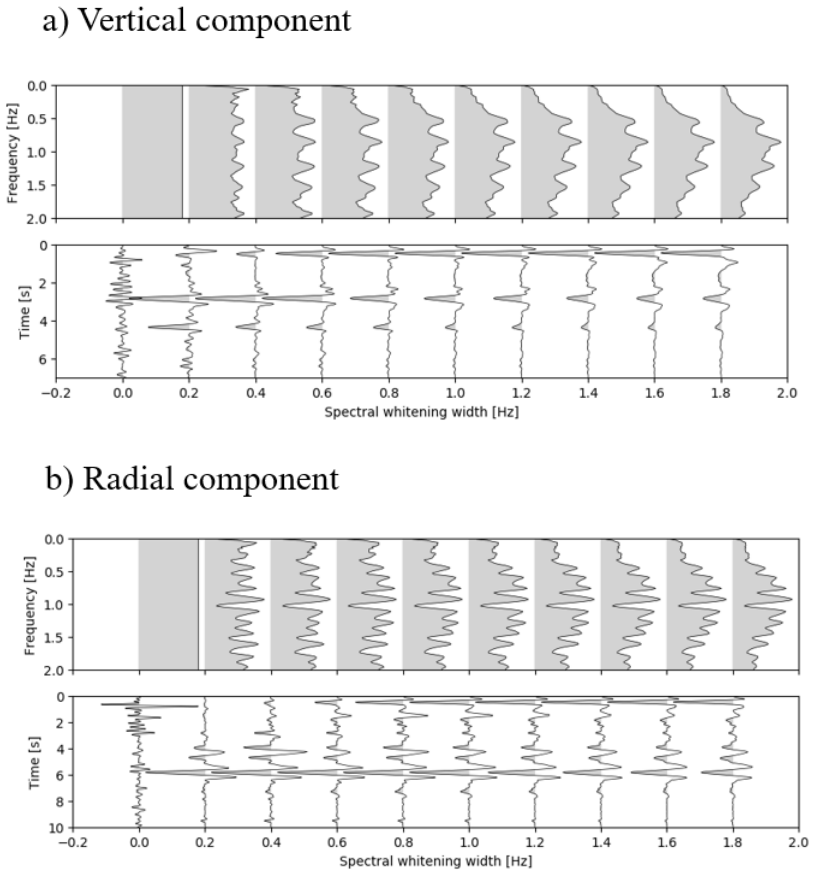

Figure3.16: Effect of varying spectral whitening widths in synthetic autocorrelations. Top panel shows the linear stack of whitened power spectra and bottom panel shows the temporal stacked autocorrelation.

3.2.4.2 Real data

We applied this technique in real data to select the optimal spectral whitening width. For example, linearly stacked power spectra in vertical as well as the radial component for station H0070 is shown in figure3.17.

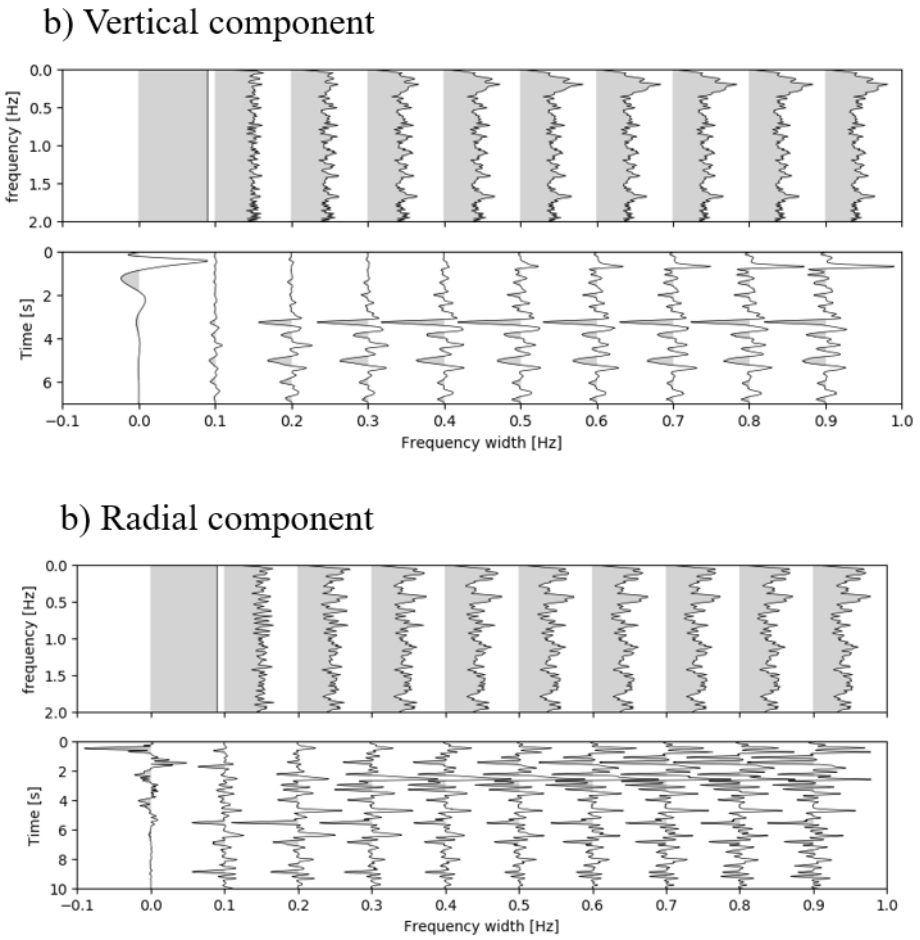

Figure3.17: Effect of tuning spectral whitening width for the vertical and radial component autocorrelations, computed for station, H0070. Top panel shows the linear stack of the whitened power spectra as a function of spectral whitening width and bottom panel refers to temporal autocorrelation computed for different whitening widths.

We observed the resonance pattern in linearly stacked power spectra in a vertical and radial component when spectral whitening widths are greater than or equal 0.20 Hz. The space between resonance peaks in vertical component and radial component are nearly 0.30 Hz and 0.16 Hz, which are equivalent to the reciprocal of the two-wave travel time of the 2p and 2s phase for station H0070.

3.2.5 Estimation of error bound:

We obtained the depth of discontinuities by using the seismic wave velocity model and the reflection delay time. As we know that achieving an accurate velocity model is almost impossible as seismic velocities depend on chemical composition, phase transformation, metamorphic reaction, dehydration, partial melting, temperature, pressure, and porosity. And delay time obtained from the 2p and 2s phases have also some uncertainties. If v is the seismic velocity and t is the two-way reflection delay time corresponding to the interface at depth H, then the error bound in estimating the depth of interface (δH) is given by following expression.

$\delta H = \frac{1}{2}(v\delta t + t\delta v)$

In our work, we obtained the uncertainty in delay time by taking the standard deviation of 100 samples around the minimum amplitude. We resampled the stacked autocorrelogram based on upper corner of bandpass filter so that 100 sample points are within the pulse. For uncertainty in the velocity, we took the standard deviation of velocities obtained from Bayesian inversion.

The ratio of two-way reflection delay time of the 2s (t_{2s}) and 2p (t_{2p}) phases is equivalent to V_p/V_s ratio and its error bound (δp) is obtained from following expression.

$\delta p = t_{2s}\delta t_{2p} + t_{2p}\delta t_{2s}$

3.3 Results and Discussion

3.3.1 P wave reflectivity:

We applied the autocorrelation method to the vertical component to extract P wave reflectivity associated with local structure beneath the seismic stations which were deployed in Nepal. Here, our objective is to estimate the depth of sediments, MHT, interface between Indian upper and lower crust and Moho beneath the seismic stations beneath Nepal. We started our work from the seismic stations deployed in south of

MFT.

3.3.1.1 Results for stations South of MFT:

The individual vertical autocorrelograms as a function of epicentral distance and stacks of seismic records from the teleseismic data set of stations NG010, H0010, JANA, and BIRA are shown in figure3.19.

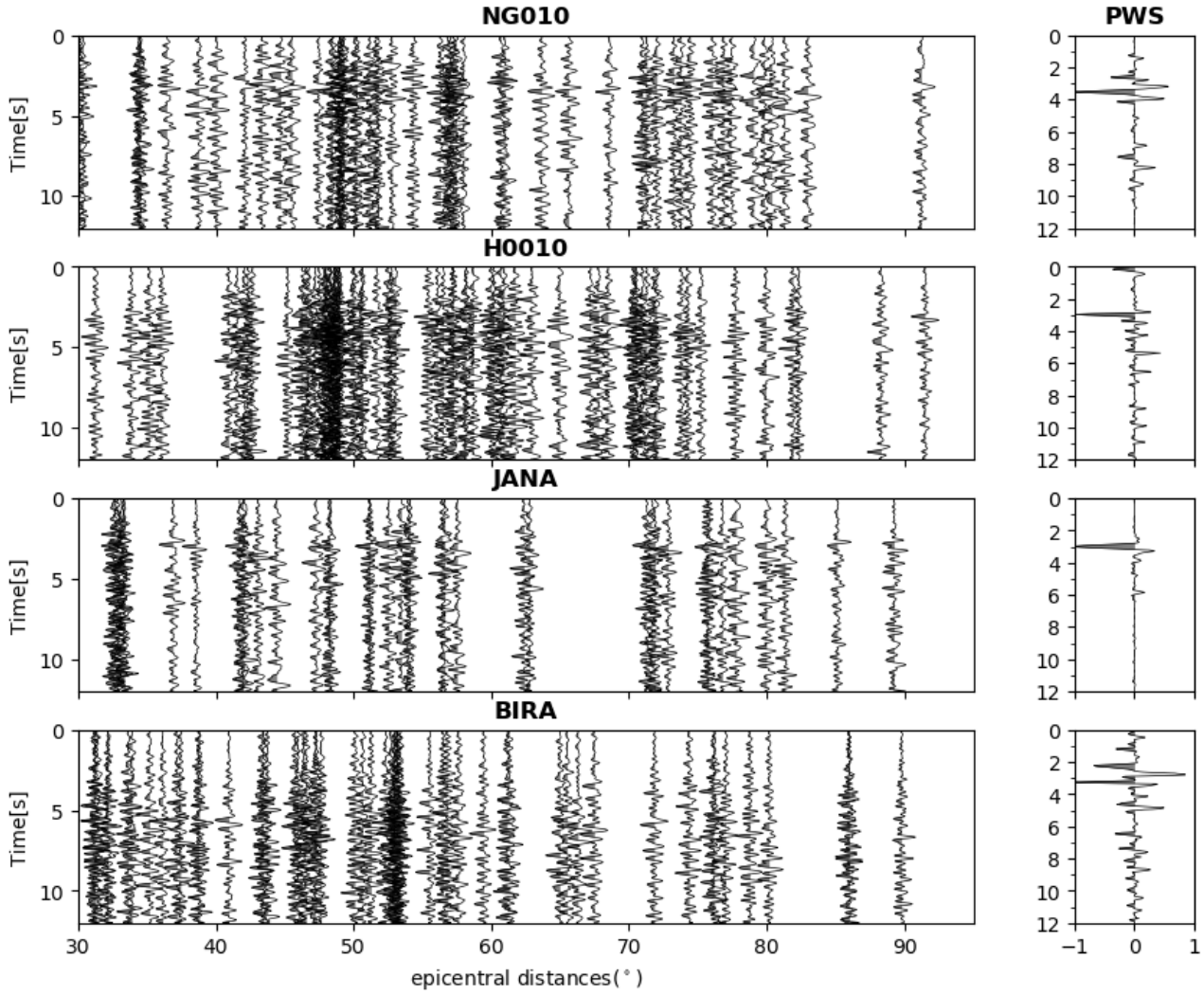

Figure 3.19: One sided autocorrelograms of individual vertical seismograms recorded by station H0010, NG010, JANA and BIRA as a function of epicentral distance (left), one sided phase weighted vertical stacked autocorrelograms (right).

The parameters used in this study are summarized in the table below.

Type of interface	Whitening width (Hz)		Frequency band of filter (Hz)
	vertical	Radial	
shallow	0.25-0.90	0.15-0.45	0.5-3.5
Intermediate	0.10-0.15	0.05-0.10	0.5-2.0

deeper	0.03-0.10	0.03-0.10	0.10-1.0

From phase weighted vertical stacked autocorrelograms (Fig3.19), we can observe a prominent peak around 3 s. We know that the prominent peaks in vertically phase weighted stacked autocorrelograms is 2p. Hence, we can associate the delay time of 2p as the observed phases around 3 s in the vertical autocorrelograms. The 2p phases observed in our results might corresponds with the interface that separates the sediment deposited in the upper crust beneath the south Nepal.

We also estimated the deeper major interface beneath stations in the South of MFT. We computed the depth of deeper interface beneath the stations NG010, H0010, JANA, and BIRA. The purpose of this is to observe the thickness of crust beneath South Nepal when we move eastward in Southern Nepal. The individual autocorrelograms as a function of epicentral distance and stacks of seismic records from the teleseismic data set of stations H0010, NG010, JANA, and BIRA are shown in figure3.20. Here, the individual autocorrelograms are much noisier for the observed data compared to the autocorrelograms from synthetic data (e.g., Fig3.10). Nevertheless, the phase weighted stacked vertical autocorrelograms shows clear prominent peaks at 13-14 s which might be delay time of 2p phase. Interestingly, for station NG010, we observe three prominent peaks on the vertical autocorrelograms. Out of three peaks, one should be 2p phase associated with Moho and others could be associated with other interfaces. Based on the delay time of 2p and 2s phases observed in vertical and radial stacked autocorrelogram (for 2s phase, see S wave reflectivity section), the phase appears at 19.5 s in vertical stacked autocorrelogram might be the s+p phase. Since, we also observed the prominent phases around 7.5 s in vertical stacked autocorrelogram but there are not convincing phases appears in radial stacked autocorrelogram. This might indicate the presence of gradient in P velocity and homogeneous S velocity in shallower structure beneath station NG010.

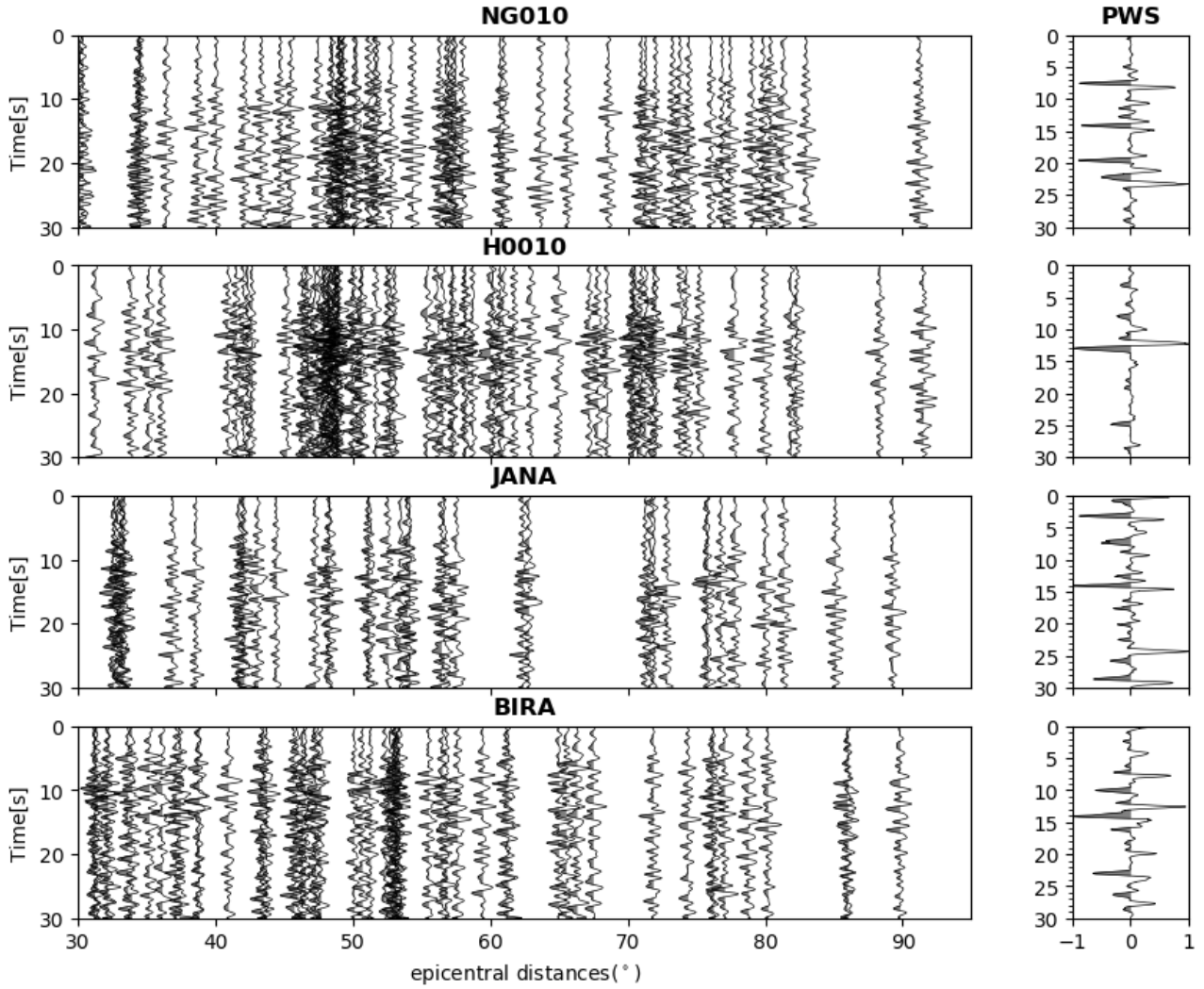

Figure 3.20: One sided autocorrelograms of individual vertical seismograms recorded by station H0010, NG010, JANA and BIRA as a function of epicentral distance (left), one sided phase weighted vertical stacked autocorrelograms (right).

Using the P wave velocity model for the Nepal region (Monsalve et al., 2006) and substituting the delay time of 2p phase obtained from the autocorrelation of the vertical in equation 3.5, we can estimate the depth of major interface recovered from autocorrelation. The computed depth of shallow interface in our work is approximately 9 km. Mitra et al., (2006) suggest up to 10 km thick sedimentary layer in southern Nepal which agrees well with our observation. The depth of deeper interface from our study is approximately 39 km. We associate this discontinuity as the Moho which have been found from receiver function to be around 40 km (e.g., Nábělek et al., 2009; Schulte-Pelkum et al., 2005). We presented the recovered depth of shallow as well as

a deeper interface in figure3.21.

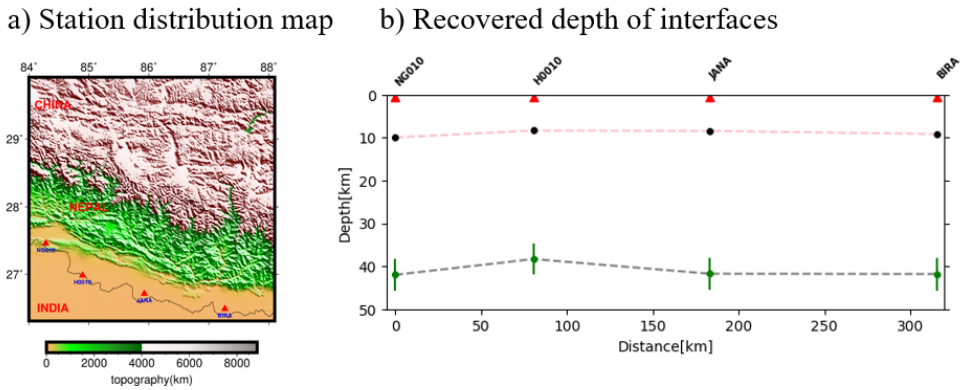

Figure 3.21: Computed depth of shallow and deeper interface beneath the stations in Southern Nepal. Black circles represent the depth of the shallow interface recovered from the delay time of the P wave. Green circles represent the computed depth of the deeper interface from the delay time of the P wave.

3.3.1.2 Results for station North of MFT:

We also have mapped the deeper interface below some stations that belongs to Hi-MNT Network. We chose those stations for which the receiver function results are available. We recovered the deeper interface below stations DINX, RBSH, PHAP, RUMJ, and GAIG from vertical autocorrelation of the coda of the P wave. Pelkum et al., 2005 mapped the Moho beneath these stations by using the receiver function method. The Moho depth obtained by them is shown by the black dashed line in figure3.23(c). The individual autocorrelograms as a function of epicentral distance and stacks of seismic records from the teleseismic data set of station GAIG, RUMJ, PHAP, RBSH, and DINX are shown in figure3.22.

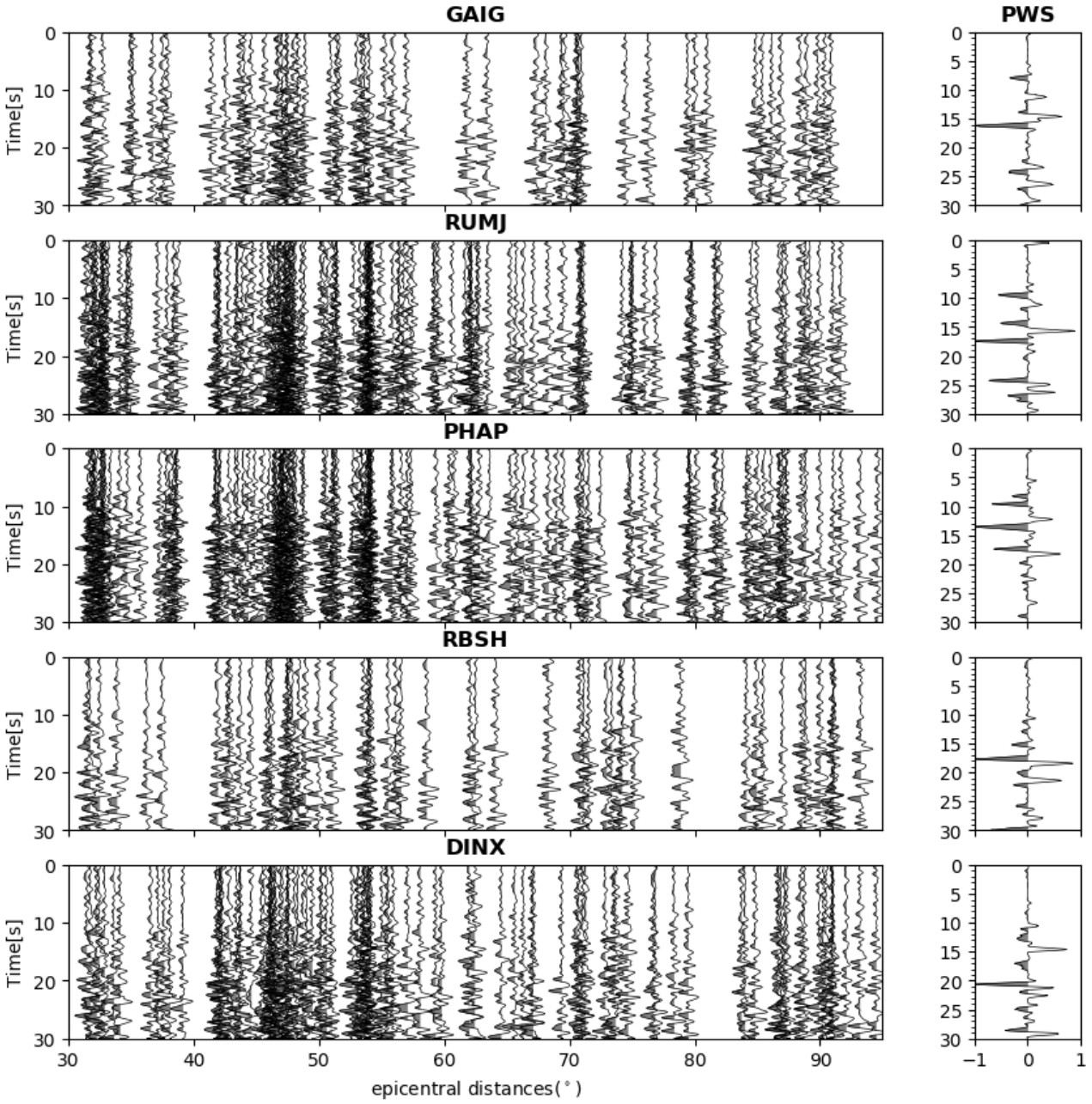

Figure 3.22: one sided autocorrelograms of individual vertical seismograms recorded by station GAIG, RUMJ, PHAP, RBSH and DINX as function of epicentral distance (left) and one-sided phase weighted vertical stacked autocorrelograms (right).

In stations PHAP, RBSH, and DINX, we observed the prominent peaks at 13.5 s, 17.7 s, and 20.6 s. For these stations, we observed the less prominent peaks at 17.4 s, 22.3 s, and 25 s (Fig3.31 (b)). The depth of interface corresponding to reflection phases are calculated by using the equation 3.5 and plotted by black solid circles while the depth computed for less prominent peaks is shown by gray cross in figure3.23(c). We observed the depth of deeper interface

corresponding to prominent peak below stations GAIG and RUMJ is same as Moho depth obtained by Pelkum et al., 2005. The deeper interface recovered corresponding to the prominent peak below PHAP, RBSH and DINX are relatively shallower than Moho reported by Schulte-Pelkum et al., 2005 while the depth corresponding to less prominent peaks is close to the Moho proposed by them. Previous studies along this region suggested the stronger interface between mid-crust and lower crust than between lower crust and upper mantle (Moho) (Q. Xu et al., 2015). We assumed that the prominent reflection phases were observed in vertically stacked autocorrelogram corresponding to the interface between mid-crust and lower crust beneath stations PHAP, RBSH, and DINX. Thus, our results indicated the convincing Moho beneath Nepal and mid-crustal reflector beneath Tethys Himalaya but the Moho recovered beneath Tethys Himalaya is poor.

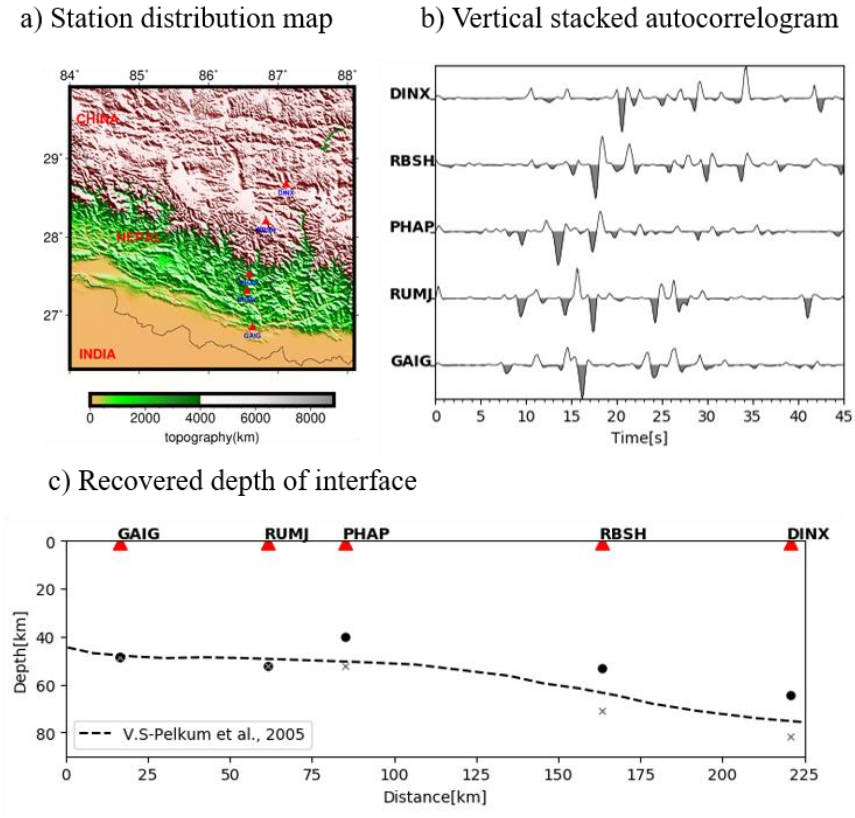

Figure 3.23: Variation of depth of deeper interface below stations DINX, RBSH, PHAP, RUMJ and GAIG.

3.3.1.3 Results for Hi-CLIMB array

We extracted the P wave reflectivity by autocorrelating the vertical component recorded by stations from Hi-CLIMB array which were deployed along South-North in central Nepal. We used the data from 30 seismic stations which were deployed inside the political boundary of Nepal. Here, our objective is to map the discontinuities beneath each station. From the autocorrelations of vertical component of seismogram from each station, we obtained 21 good qualities (based on SNR) stacked autocorrelograms to recover the shallow interface. The stacked autocorrelograms and the station distribution maps are shown in figure3.24.

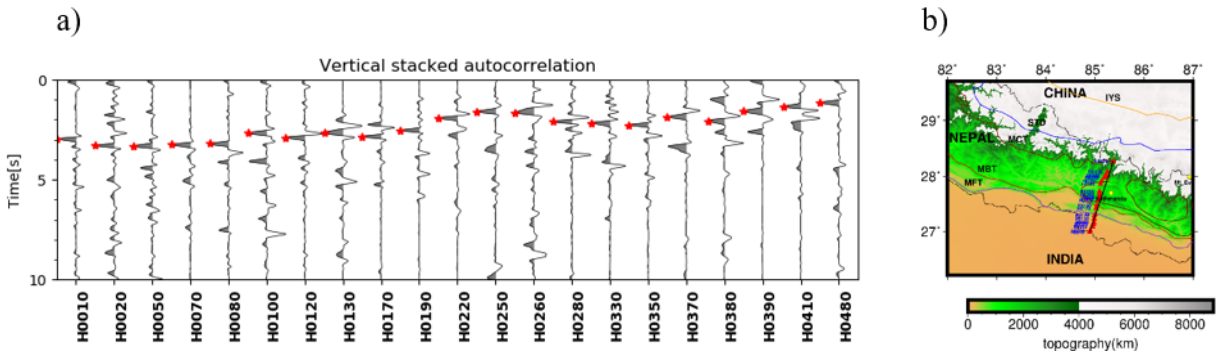

Figure3.24: Vertical autocorrelation stacks for 21 stations along South-North in Central Nepal (left). Red star shows the prominent phases in autocorrelogram which indicate the time picks of P reflections. Station distribution map which are used for autocorrelation (right).

We obtained 15 good qualities vertical stacked autocorrelograms out of 30 to recover the mid-crustal interface beneath Nepal. The stacked autocorrelograms and the station distribution maps are shown in figure3.25.

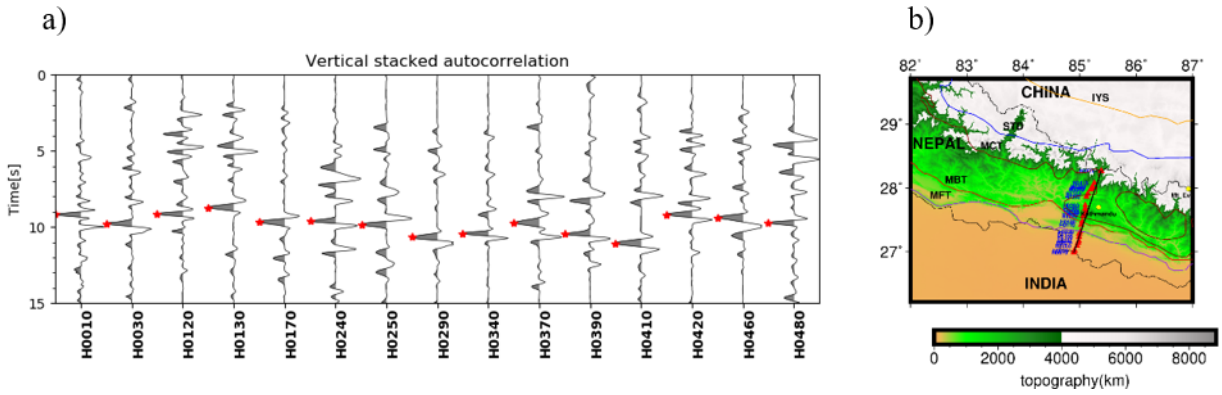

Figure3.25: Vertical autocorrelation stacks for 15 stations along South-North in

Central Nepal (left). Red star shows the prominent phases in autocorrelogram which indicate the time picks of P reflections. Station distribution map which are used for autocorrelation (right).

Those stacked autocorrelogram which shows the prominent peaks are picked to recover the Moho beneath Nepal. The stacked autocorrelograms and the station distribution map is shown in figure3.26.

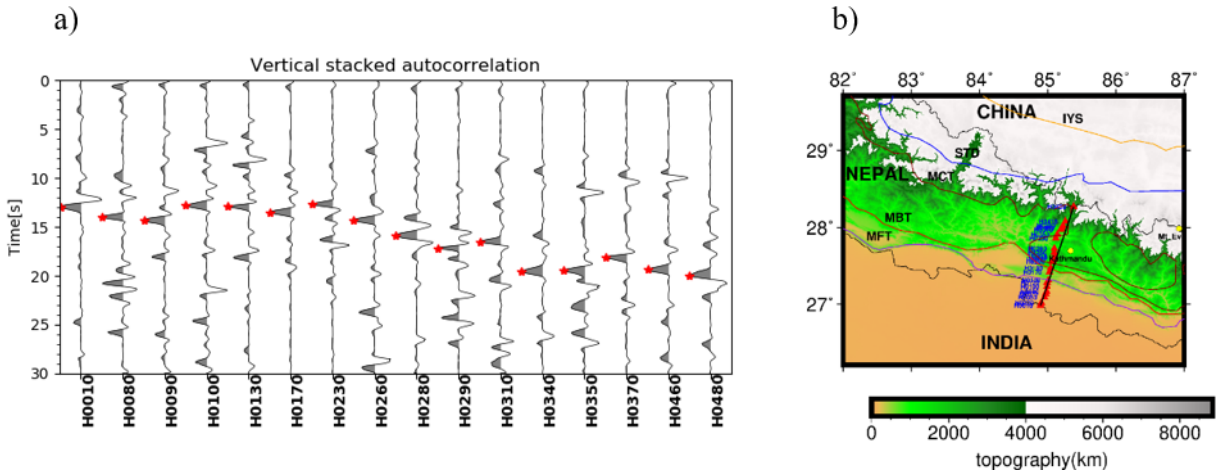

Figure3.26: Vertical autocorrelation stacks for 16 stations along South-North in Central Nepal (left). Red star shows the prominent phases in autocorrelogram which indicate the time picks of P reflections corresponding to Moho beneath each station. Station distribution map which are used for autocorrelation (right).

The P reflection time obtained from the stacked vertical autocorrelogram of each station is inverted to obtain the depth of interface below these stations. To invert the reflection delay time, we used the P wave velocity model for the Nepal region. The recovered depth of shallower interface is shown in figure3.29. The obtained result indicates the presence of a shallower interface at depth 3-9 km. The shallower interface recovered might represent the depth of sediments deposited in south Nepal. We observe that the depth of the interface decreases while moving northward, which is well correlated with the geology of Nepal (Upreti, 1999). The depth of interface slowly increases beneath Kathmandu and again decreases towards North of it. This result indicates that Kathmandu city sits on a thick sedimentary basin. Our result also shows that the depth of sediments deposited beneath Kathmandu is nearly 7 km. We used the stacked autocorrelograms obtained from 21 seismic stations which were distributed

along 150 km long south-north profile. Hence, such dense station distribution ultimately provides image of shallow interface with high lateral resolution. The lateral resolution in our results is in range 3-20 km.

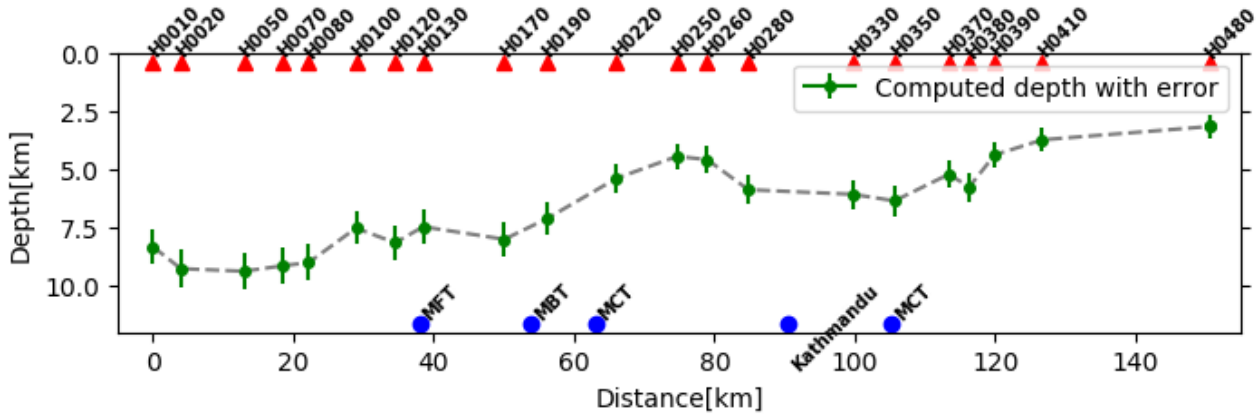

Figure3.27: Depth of sediments below 21 stations along South-North of Central Nepal with the uncertainty. Blue circles mark the location of MFT, MBT, MCT, and Kathmandu along the profile and red triangles represent the seismic station used for autocorrelation.

We have observed flat interface along South-North at depth around 30 km beneath Central Nepal (Fig3.30). This might correlate with seismic reflector obtained between depth 30 and 40 km beneath the Tethyan Himalaya (Zhao et al., 1993). The mid-crustal interface beneath Lesser and Greater Himalayas at around 30 km might be the interface between upper and lower crust of underthrusting Indian Plate. The depth of interface between Indian upper and lower crust obtained from receiver function is shown by blue dotted line and from our work is shown by black circles in figure3.28. We observe the presence of a deeper interface at a depth of 40-60 km along the South-North of Central Nepal. The interface is flat in the South of MCT and starts to deepen towards the North of MCT. Previous studies in this region (e.g., Nábělek et al., 2009) show the Moho is located around a depth of 40 km in the South of Nepal and deepens towards the North (see the black dashed line in Fig3.30). The result obtained from autocorrelation of vertical component shows the presence of Moho at depth 40 km in South of MCT and reaches up to 60 km in North of MCT.

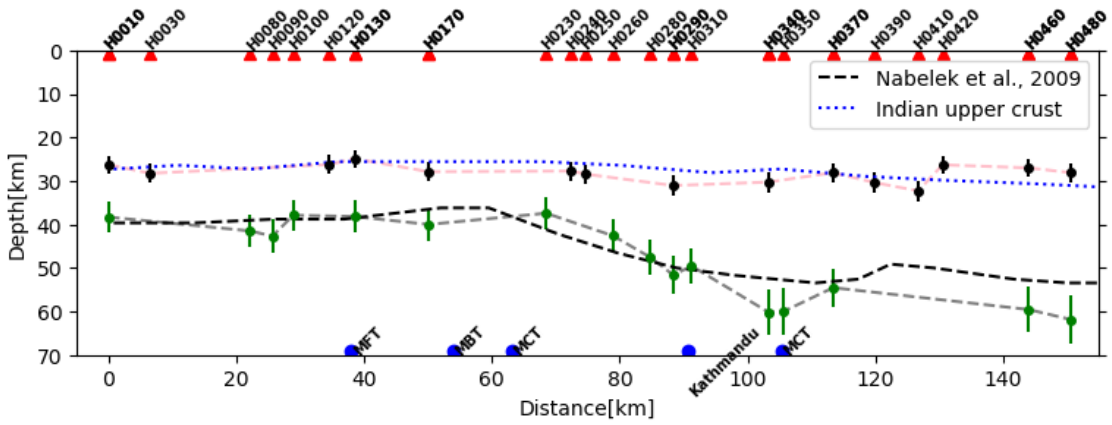

Figure3.28: Depth of Indian upper crust and Moho below stations along South-North of Central Nepal with the uncertainty. Blue circles mark the location of MFT, MBT, MCT, and Kathmandu along the profile and red triangles represent the seismic station used for autocorrelation.

3.3.2 S wave reflectivity:

Though the autocorrelation technique is widely applied to the vertical component to extract P wave reflectivity associated with the local structure beneath the seismic station (Kennett, 2015; Kennett et al., 2015; Saygin et al., 2017), it can also be applied to the radial component to extract S wave reflectivity (Pham & Tkalcic, 2017, 2018). Here, we extract the S- wave reflectivity by autocorrelating the radial component recorded by stations deployed in Nepal.

3.3.2.1 Results for station South of MFT:

The individual radial autocorrelograms as a function of epicentral distance and stacks of seismic records from the teleseismic data set of stations NG010, H0010, JANA, and BIRA are shown in figure3.29. We can observe a prominent peak around 6 s in phase weighted radial stacked autocorrelograms (Fig3.29). We know that the prominent peaks in radially phase weighted stacked autocorrelograms is 2s. Thus, we can associate the delay time of 2s as the observed phases around 6 s in the radial autocorrelograms. The observed 2s phases in our results might corresponds with the interface that separates the sediment deposited in the upper crust beneath the south Nepal.

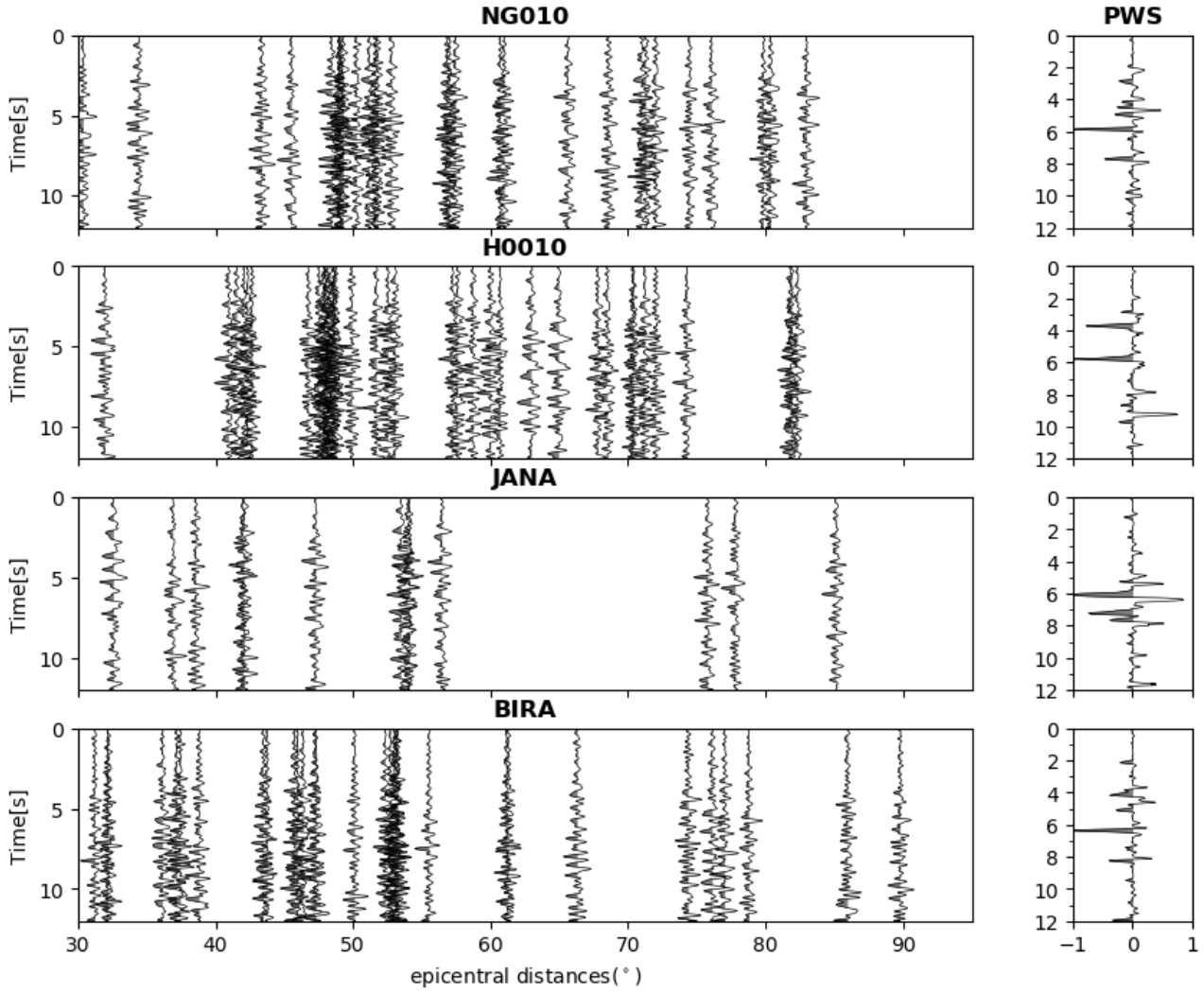

Figure 3.29: One sided autocorrelograms of individual radial seismograms recorded by station H0010, NG010, JANA and BIRA as a function of epicentral distance (left), one sided phase weighted vertical stacked autocorrelograms (right).

We also estimated the deeper major interface beneath stations in the South of MFT from the autocorrelation of radial component of seismogram. The individual radial autocorrelograms as a function of epicentral distance and stacks of seismic records from the teleseismic data set of stations H0010, NG010, JANA, and BIRA are shown in Fig3.30. The reflection delay time corresponding to 2s phase for the stations H0010, JANA, and BIRA is nearly 20 s, while 23.5 s for stations NG010. This might indicate either the presence of deeper Moho than beneath other stations or the low shear wave velocity layer in crust beneath station NG010.

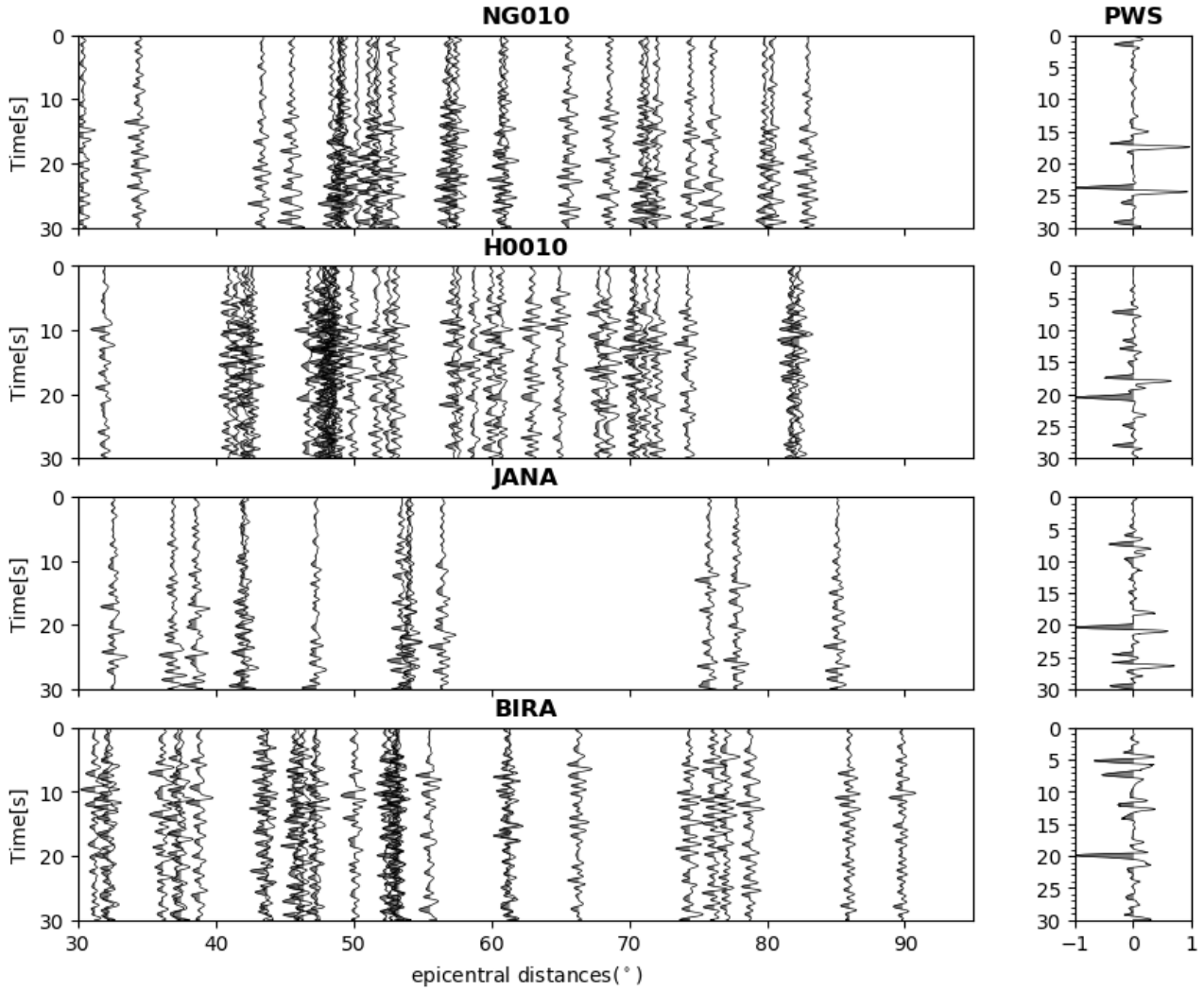

Figure 3.30: One sided autocorrelograms of individual radiall seismograms recorded by station H0010, NG010, JANA and BIRA as a function of epicentral distance (left), one sided phase weighted vertical stacked autocorrelograms (right).

We used the average 1-D velocity model of S wave velocity for Nepal region to estimate the depth of interfaces. Based on the delay time of 2s phases observed in radial stacked autocorrelograms, the estimated depth of shallow interface is 10 km and deeper interface is 35-40 km.

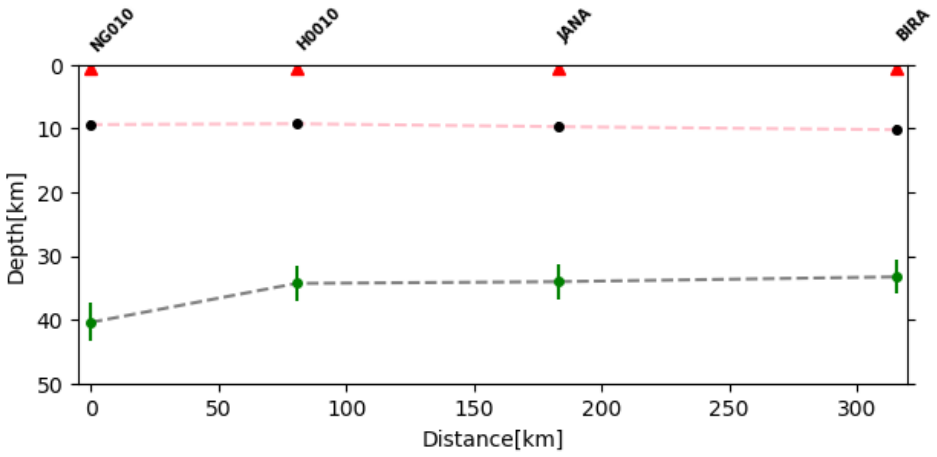

Figure 3.31: Computed depth of shallow and deeper interface beneath the stations in Southern Nepal. Black circles represent the depth of the shallow interface recovered from the delay time of the S wave. Green circles represent the computed depth of the deeper interface from the delay time of the S wave.

3.3.2.2 Results for Hi-CLIMB array

We extracted the S wave reflectivity by autocorrelating the radial component of seismogram recorded by stations belongs to Hi-CLIMB array. From the autocorrelation of radial component of seismograms, we could image two crustal interfaces beneath Nepal. The stacked autocorrelograms and the stations distribution map is shown in figure3.32.

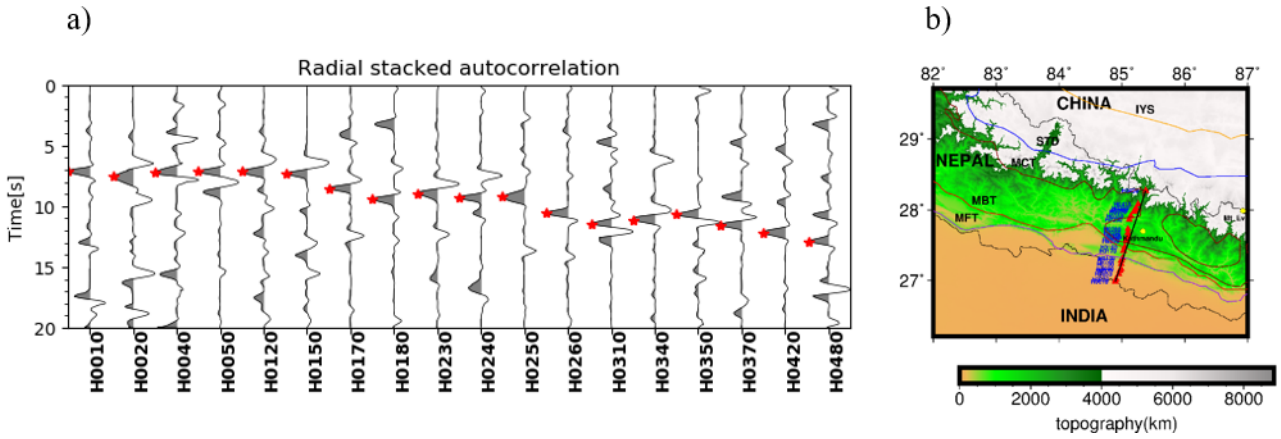

Figure3.32: Radial autocorrelation stacks for 18 stations along South-North of Central Nepal (left). Red star shows the prominent phases in autocorrelogram which indicate the time picks of S reflections. Station distribution map which are used for autocorrelation (right).

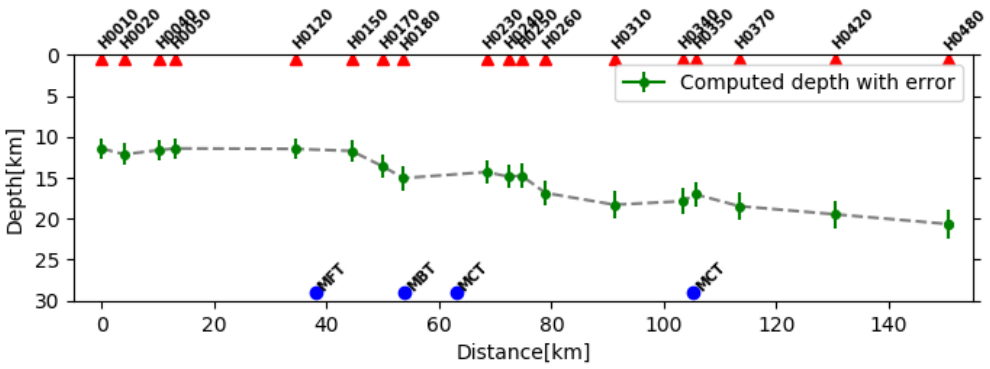

Figure3.33: Depth of mid-crustal interface below 18 stations along South-North of Central Nepal with the uncertainty. Blue circles mark the location of MFT, MBT and MCT along the profile and red triangles represent the seismic station used for autocorrelation.

The S reflection time obtained from the stacked radial autocorrelogram of each station is inverted to obtain the depth of interface below the station. To invert the reflection delay time, we used the S wave velocity model for the Nepal region (Monsalve et al., 2006). The recovered depth of the interface is shown in figure3.33. Our results show the presence of an interface undulating between 10-20 km depth along South-North of Central Nepal. The interface is flat in the South of MFT and slightly deepen towards the North of MFT. We observed the interface is flat again in between MBT and MCT and depth increases slowly towards North of MCT. As we observed the prominent peaks in radial autocorrelogram, the interface might have high reflection coefficient for S-wave. Previous studies shows the presence of low velocity zone (LVZ) at depths of 15 km (Nábělek et al., 2009; Unsworth et al., 2005). Hence, we interpret the interface recovered from S wave reflectivity in South of MFT that separates the LVZ. It has been found that fluids are present in the flat portion of MHT (Lemonnier et al., 1999), which might be the reason for LVZ in South of MFT. Hence, the interface that separates the LVZ might highlights the position of MHT in South of MFT in central Nepal. We have used stacked autocorrelogram from 18 stations along a 150 km profile, which gives the high lateral resolution image of MHT beneath Nepal.

Thus, from the autocorrelation of vertical and radial components, we mapped Moho and three internal crustal interfaces above Moho along the South-North profile beneath

the crust of central Nepal. The shallow discontinuity and Moho are recovered from P wave reflectivity while the interfaces at mid-crust is recovered from both P and S wave reflectivity. All the recovered interfaces from autocorrelation of 30 seismic stations are shown in figure3.34.

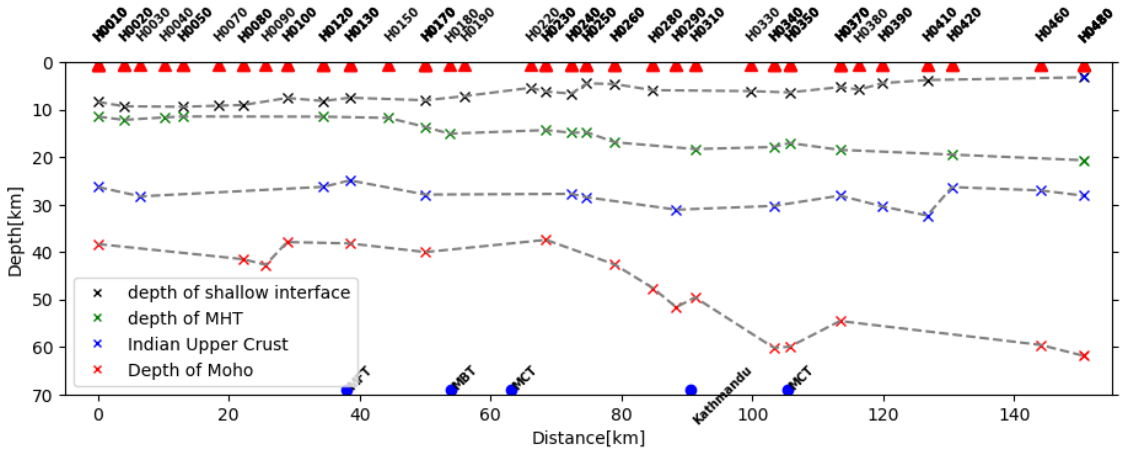

Figure3.34: Depth of all interfaces recovered from the vertical and radial autocorrelation of 30 seismic stations.

3.3.4 Estimating depth of interface from our velocity model:

The average 1-D velocity model has been used to map the interfaces across our study area by receiver function as well as autocorrelation approach. We know that, seismic velocity structure can be varied laterally as well as function of depth, especially for the regions like our study area where the geological conditions vary at different locations (Upreti, 1999). So, using an averaged 1-D velocity model to map the interface may not give the precise depth of the interface. For example, the averaged shear wave velocity (Monsalve et al., 2006) of 3.20 km/s is high for the sediments. Our study (Ambient noise tomography) shows the velocity around 2.70 km/s for sediments. Hence, the depth of shallow interface might be different if we computed the depth by using local 1-D velocity model. In our study, we have produced the local 1-D velocity model by the joint inversion (Bayesian self-parametric) of phase and group velocity of Rayleigh wave (obtained from cross correlation of ambient noise).

3.3.4.1 Results for station South of MFT

We computed the depth of shallow and deeper interface by using delay time of 2s phase and the local 1-D S-velocity model obtained from ambient noise tomography (our work). The interface depth obtained by using our 1-D S-wave model and averaged 1-D velocity model of Monsalve et al., 2006 are presented in figure3.32.

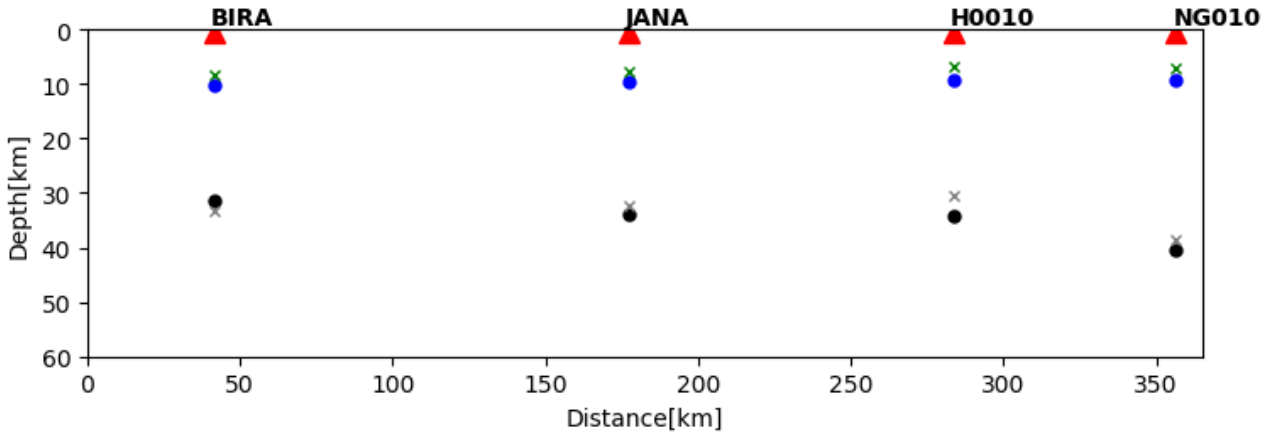

Figure3.35: Comparison of depth of shallow and deeper interface computed by using velocity model of Monsalve et al., 2006 (shown by blue and black circle) and our velocity model (shown by green and gray cross). Red triangles refer to the station used for autocorrelations.

3.3.4.2 Results for station North of MFT

The deeper interfaces below stations GAIG, RUMJ, PHAP, RBSH, and DINX are recovered from a delay time of 2p phases. Hence, we need a P-wave velocity model to compute the depth of the interfaces. In our work, we computed the Shear wave velocity model from the Ambient Noise Tomography method. To convert the S-wave velocity model to the P-wave velocity model, we used the fixed Poisson's ratio of 1.7320. The depth computed from our model and Monsalve et al., 2006 are presented in figure3.33. The depth of interface recovered by using our velocity model corresponding to the prominent peaks in vertically stacked autocorrelograms are shown by the green cross and depth corresponding to less prominent peaks are shown by gray cross in figure3.33. We observed that the recovered depth of interfaces from our model is nearly similar to the depth obtained from Monsalve et al., 2006.

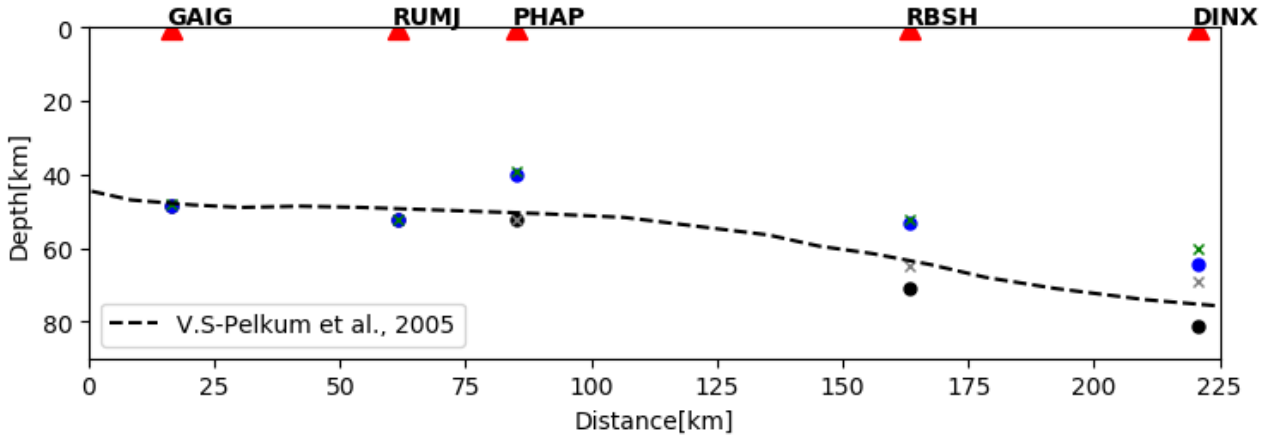

Figure 3.36: Comparison of thickness of deeper interface obtained from our model and existed model (Monsalve et al., 2006) below stations in Nepal and South Tibet. The depth recovered from our model and existed model are shown by cross and circle, respectively.

3.3.4.3 Results for Hi-CLIMB array

We computed the depth of shallow and deeper interface from P wave reflectivity, so we need a P wave velocity model which is obtained by multiplying S velocity obtained from our work by fixed Poison's ratio. The estimated depth of shallow, mid-crustal, and deeper interfaces from our model and Monsalve et al., 2006 model is presented in figure3.37. We observed the difference in the depth of interface in south of MFT. This might be the consequence of not addressing the low velocity for sediments by averaged 1-D velocity model. Our velocity model from ANT shows that S wave velocity for sediments is less than 2.80 km/s in Southern Nepal. The estimated depth of interface from existed 1-D velocity and from our model is very close to each other in north of MFT.

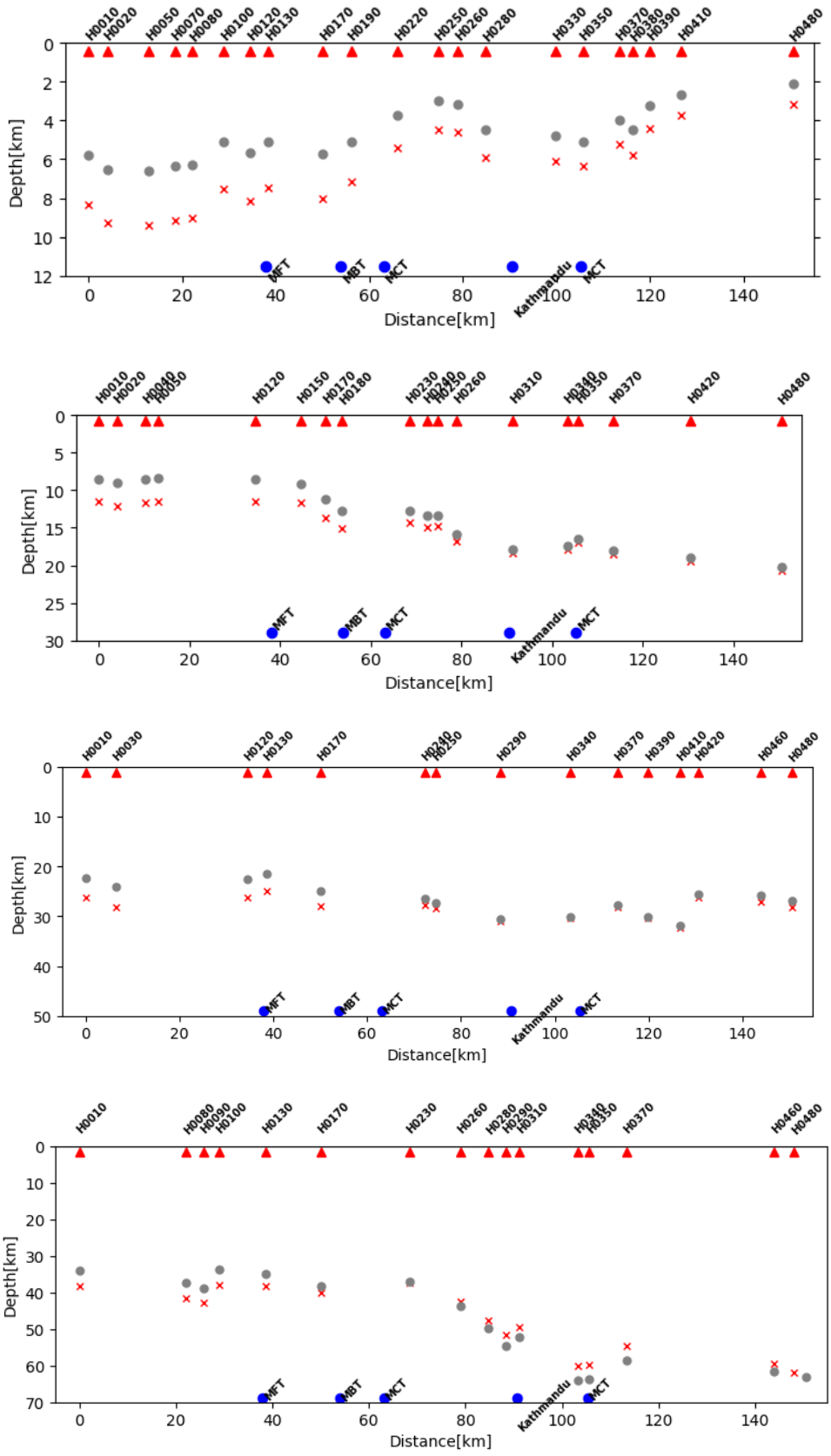

Figure 3.37: Comparison of thickness of interface obtained from our model and Monsalve et al., 2006 below stations along South-North in Central Nepal. The depth recovered from our model is represented by gray circles and Monalve et al., 2006 model is represented by red cross.

3.3.3 Estimating Vp/Vs ratio of shallow crust

In South Nepal, we used data from four different seismic stations. The stacked autocorrelograms of both vertical and radial components shows good signal-to-noise ratio. Thus, we used the vertical and radial component to get delay time of 2p and 2s phases. The ratio of delay time of 2s and 2p phases is equivalent to V_p/V_s ratio. The estimated V_p/V_s ratio by using the delay time of 2p and 2s phases is nearly 2.0 for all the stations in south of MFT. The high V_p/V_s ratio might indicate the presence of loose sediments with water content in South Nepal. The high V_p/V_s ratio is also observed by Wang et al., 2012. The computed V_p/V_s ratio and the vertical and radial stacked autocorrelograms are shown in figure3.38-3.39.

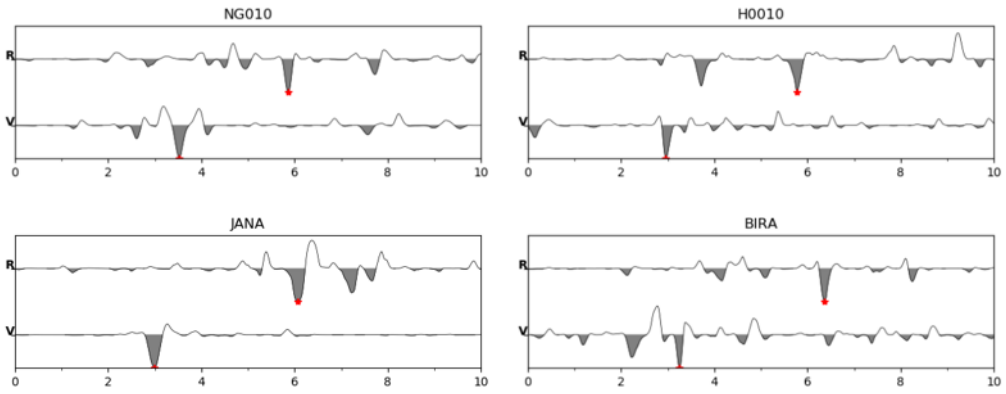

Figure3.38: Autocorrelation stacks for 4 stations of which both radial and vertical components show the good signal-to-noise ratio. The station name is mentioned at top of each plot and R and V indicates the radial component and vertical component. Red star indicates the delay time of P and S wave.

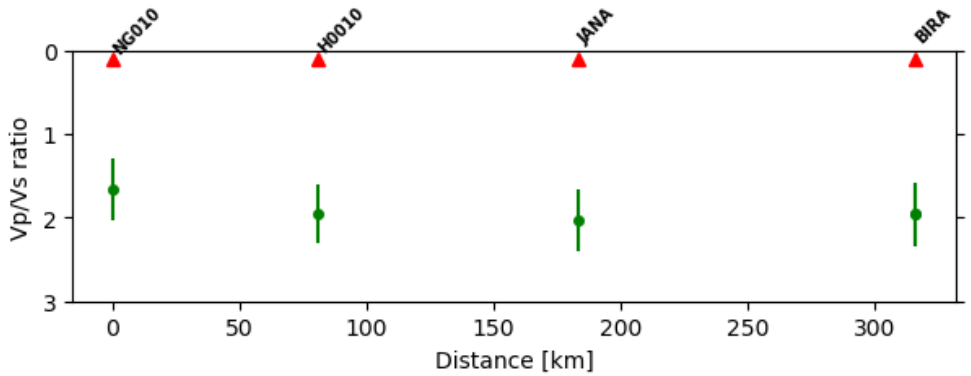

Figure3.39: Estimated Vp/Vs ratio of shallow crust beneath 4 seismic station along East-West profile in South Nepal.

In the South-North profile of Central Nepal, we used seismic data from 30 seismic stations. Out of 33 stations, we obtained autocorrelation stacks of both radial and vertical for 13 stations with a good signal-to-noise ratio (Fig3.35). If we assume the sediments deposited in the shallow crust beneath Nepal as a homogeneous layer, the ratio of S and P wave delay time represents the Vp/Vs ratio. The estimated Vp/Vs ratio is shown in figure3.36. Our results show that the Vp/Vs ratio of sediments is around 2.0.

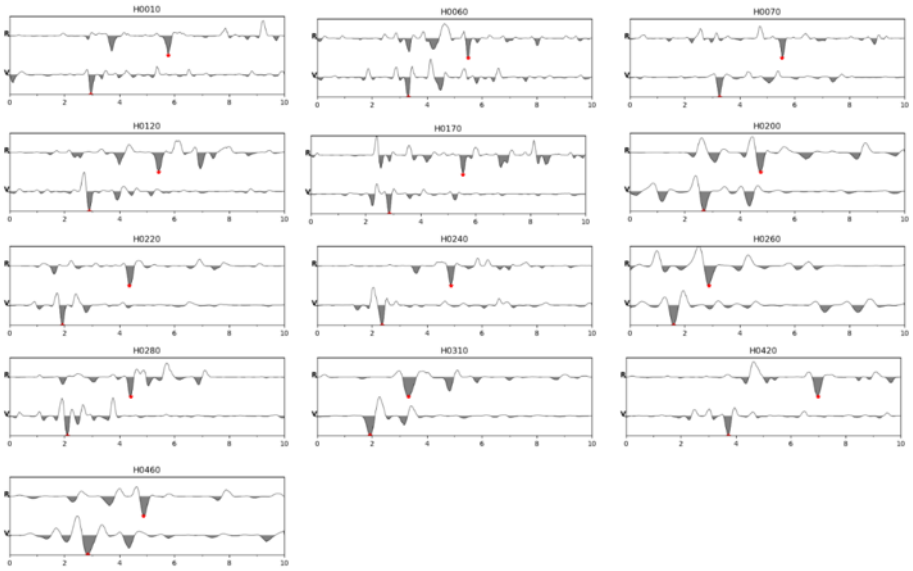

Figure3.35: Autocorrelation stacks for 13 stations of which both radial and vertical components show the good signal-to-noise ratio. The station name is mentioned at top of each plot and R and V indicates the radial component and vertical component. Red star indicates the delay time of P and S wave.

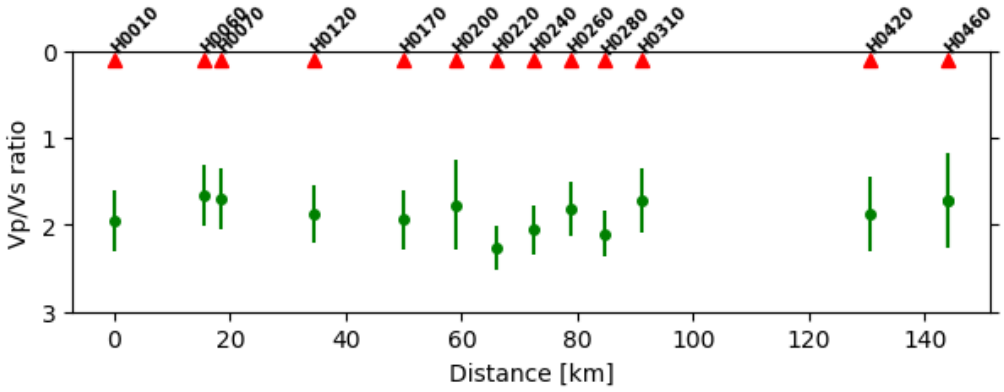

Figure3.36: Estimated Vp/Vs ratio of shallow crust beneath 13 seismic station along South-North profile in Central Nepal.

3.4 Conclusion

Autocorrelation method successfully recovered the four major crustal seismic reflector and Vp/Vs ratio of the shallow crust beneath the Nepal Himalaya by utilizing P wave coda wave forms. Our study shows a major interface in the shallow structure of South Nepal at a depth of around 9 km and thickness of sediments decreasing from 9 km to 3 km while moving northward. We produced high resolution image of MHT along North-South beneath the Nepal Himalaya by autocorrelating the radial component of seismogram recorded by stations belongs to Hi-CLIMB array. Our results show MHT is flat in the South of MFT and deepening towards the North. We recovered the deeper discontinuity just above the Moho which is flat beneath Nepal and deepening towards South Tibet. This might be the interface between upper and lower crust of underthrusting Indian Plate. The Moho in the South of MCT is flat and has a depth of around 40 km and deepens towards the North of MCT. The depth of Moho varies from 40-60 km beneath Nepal while moving from South to North.

We computed the depth of interface recovered from 2p and 2s phases by using the existed model and the 1-D S-wave velocity from our work which is obtained from the Ambient Noise Tomography method. The computed depth of shallow as well as deeper interfaces by using our S-wave model is close to the depth computed from the existed model. In the end, we estimated the Vp/Vs ratio of the shallow crust along the South-North profile of Central Nepal by using the S and P wave delay times. Our study indicates the Vp/Vs ratio of the sediments deposited in the shallow crust of Nepal is around 2.0.

Combined Results

The results obtained from the two different methods (Ambient Noise Tomography and P wave coda autocorrelation) are complimentary. One provides knowledge of the crust

and uppermost mantle velocity structure and other provides the discontinuities. Therefore, it would be good to observe the combined results obtained from both techniques. Here, we presented the shear wave velocity profiles along the profile AA' and JJ' (see in Fig3.37 (b)) and the major interface across this profile.

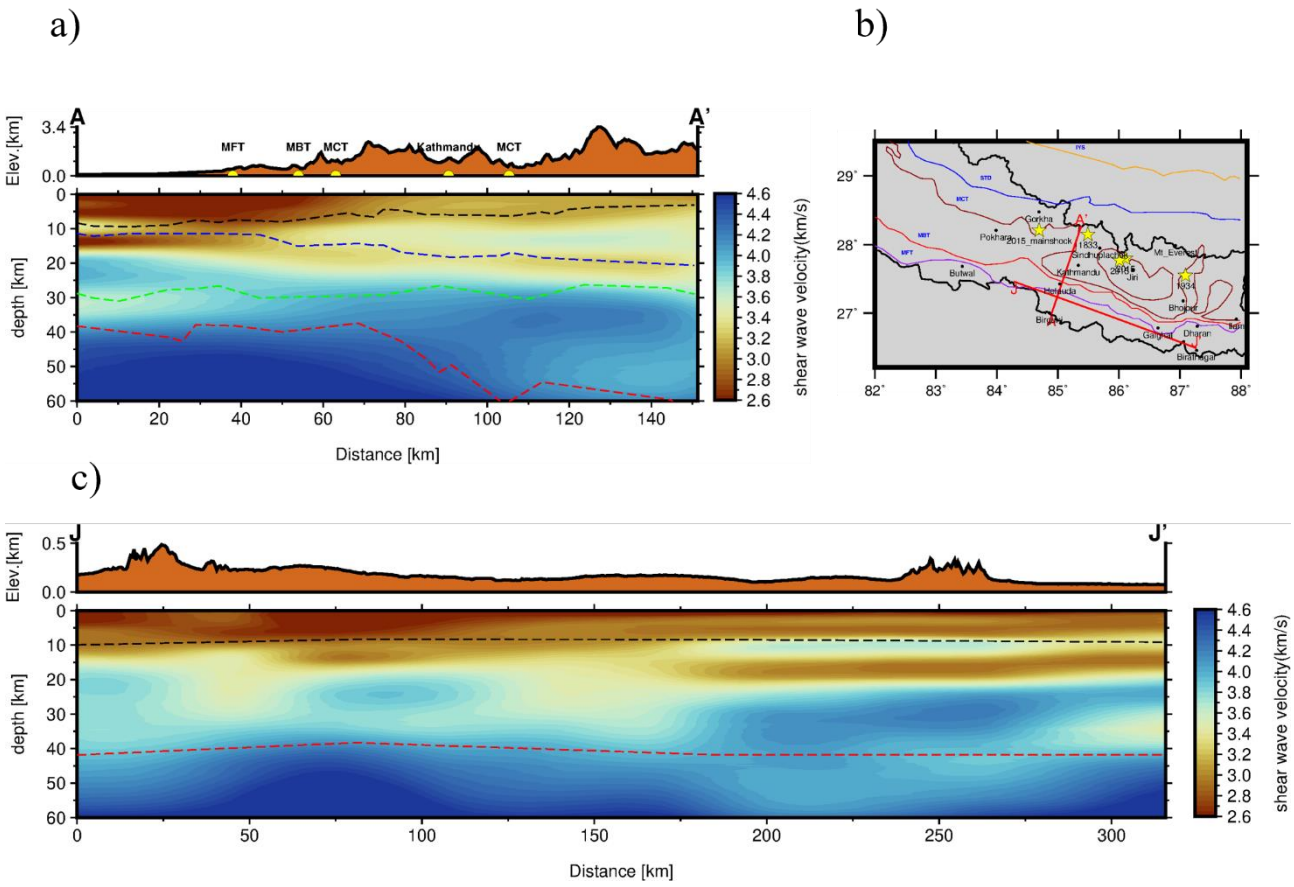

Figure 3.37: Projection of major interface obtained from P wave coda autocorrelation over shear wave velocity structure obtained from ambient noise tomography. The different color dashed line indicates the major interfaces.

Our results along profile AA' shows that the velocity structure and the interface are in good agreement. The shallow interface clearly separates the low velocity top layer. We observed the low velocity layer at depth 10-20 km from the shear wave velocity structure. We interpreted this layer as MHT in chapter two. Interestingly, the interface obtained from the P wave autocorrelation follows the low velocity layer. The interface obtained at depth 30 km from autocorrelation seems like the interface between upper and lower Indian crust. We observed shear wave velocity greater than 4.2 km/s around the deeper interface obtained from the P wave coda autocorrelation. We interpreted this

interface as Moho, which is well supported from the shear wave velocity structure across this profile. We could visualize the high velocity beneath the region south of MCT from shear wave velocity structure and flat interface from P wave coda autocorrelation. The interface seems like deepening towards north, which is well supported by the shear wave velocity structure.

In the region south of MFT, we computed the two major interface from P wave coda autocorrelation. The interfaces obtained are projected in the shear wave velocity structure (see in Fig3.37(c)). The shallow interface clearly separated the low velocity top layer. The deeper interface is located at a depth where shear wave velocity is greater than 4.2 km/s. This indicates that deeper interface is separated the crustal materials from the upper mantle materials. Hence, the interface obtained at theses depths might be the Moho across this profile.

Summary

In our first part of work, we constructed high resolution 2-D phase and group tomography maps in periods of 3-35 s across our study area by cross-correlating ambient noise data recorded by stations belonging to Hi-MNT, Hi-CLIMB, Namaste, Cambridge, and HiKnet. The 2-D tomography results clearly show the velocity gradient along South-North. At shorter periods (sensitive to shallow structures), the south of the MBT shows low group and phase velocities, while the north shows relatively high velocities. These results correlate well with known geological and tectonic features in our study region. The decreasing group velocity with an increasing period in many regions indicates the presence of low velocity structures in the crust beneath Nepal and South Tibet. High group and phase velocities between MBT and STD could be associated with high crustal strength. The relatively low velocity at periods of 20-35 s over southern Tibet indicates the presence of thick crust at South Tibet.

We obtained a high-resolution shear-wave velocity structure of the crust beneath Nepal and part of South Tibet using a self-parameterized Bayesian approach. Our results show the presence of a low velocity layer along SW-NE direction which is known as MHT. Hence, we presented the high-resolution geometry of the MHT beneath Nepal and some part of South Tibet. Our results indicate the presence of weak mid-crust at South Tibet and strong mid-crust at High Himalaya. Our results show the presence of high velocity beneath the High Himalaya at a depth of 40-60 km (V_s=4.0-4.5 km/s), which could be evidence of partial eclogitization. The high velocity layer sandwiched between two low velocity layers at 10-15 km depth beneath Nepal and part of South Tibet could indicate the presence of an anisotropic layer. Our results show the low shear wave velocity at 20-30 km depth at Lesser Himalaya, which indicates the presence of aqueous fluids at high pore pressure. The relatively low S-wave velocity in the crust up to 50 km indicates the presence of thicker crust in South Tibet than in Nepal.

In the second part of our work, we successfully mapped the four major seismic reflectors with high lateral resolution by using the autocorrelation technique. Our study shows a major interface in the shallow structure of South Nepal at a depth of around 9 km and thickness of interface decreased to 3 km while moving towards North. The shallower interface at depth 3-9 km might represent the depth of sediment deposits beneath the Nepal Himalaya. The interface recovered at depth 10-20 km might be equivalent to MHT and the flat interface at depth 30 km might represents the interface between upper and lower Indian crust. The interface obtained at depth 40-60 km might be the depth of Moho. The Moho in the South of MCT is flat and has a depth of around 40 km and deepens towards the North of MCT.

We computed the depth of interface recovered from 2p and 2s phases by using the existed model and the 3-D S-wave velocity from our work which is obtained from the Ambient Noise Tomography method. The computed depth of shallow as well as deeper interfaces by using our S-wave model is close to the depth computed from the existed model. In the end, we estimated the Vp/Vs ratio of the shallow crust beneath Nepal by using the S and P wave delay times. Our study indicates the Vp/Vs ratio of the sediments deposited in the shallow crust of Nepal is around 2.0. The results obtained in our work demonstrated that autocorrelation method might provide the reliable estimation of the crustal thickness as well as images of internal crustal discontinuities independently as like other existed seismological method, such as receiver function.

Thus, we successfully presented the high-resolution images of MHT beneath Nepal Himalaya from ambient noise tomography and P wave coda autocorrelation technique. This might be useful in future for understanding the seismicity beneath the Nepal Himalaya and to mitigate the seismic hazard in this region. The high resolution 3-D shear wave velocity down to 60 km depth and the major seismic discontinuities provided by us could be used to understand the location and physics of earthquakes occurred in the Nepal Himalaya.

Future work

In this study, we have provided a high resolution 3-D shear wave velocity model for Central and Eastern Nepal, and some part of South Tibet. We have also provided constraints on the locations of crustal discontinuities beneath some stations in South and Central Nepal. We successfully presented the velocity structure of the shallow crust in our work. The success of this project implies that it can be carried out in different parts of the Himalaya to provide a complete image of shallow lithospheric structure. Because P coda autocorrelation provide the important crustal information, it can be extended to other stations as well in future. In future, the shear wave velocity model provided from our work can be used for detailed high-resolution location and monitoring of earthquakes occurring in Nepal

Our shear wave velocity model goes down to 60 km depth beneath central and Eastern Nepal, which could be further extended by adding the surface wave of higher periods. The lateral resolution in Western part of Nepal can be further improved in future by adding data from permanent stations as well as temporary stations (operated for long enough time) deployed in West Nepal, North India, and North-West boarder of Nepal and China. The shortest period achieved in our work is 3 s. In future, we can achieve the tomographic images of periods shorter than 3 s by adding the stations pair with short interstation distance so that we can improve the vertical resolution of shallow crust. The dispersion data of short period from ambient noise cross correlation can be jointly inverted with data from receiver functions. This will help remove the depth-velocity trade-offs and provide a better estimation of the anisotropy.

The autocorrelation method successfully recovered the isotropic discontinuities and Vp/Vs ratio of the shallow crust beneath Nepal Himalaya by utilizing P wave coda waveforms. In future, the autocorrelation method presented in our study can be improved by considering the data from permanent stations or temporary stations deployed for long enough period, so that we have enough data for analysis. In future,

the anisotropic properties, especially S wave anisotropy, which is more significant than the P waves, can be studied by modifying the approach to anisotropic approximation. For the anisotropic approximation, we also need to consider transverse component of seismogram. Further, to have a better constraint on the result from P wave coda autocorrelation, we can compute the autocorrelation of ambient noise recorded by the stations.

Bibliography

Ader, T., Avouac, J. P., Liu-Zeng, J., Lyon-Caen, H., Bollinger, L., Galetzka, J., et al. (2012). Convergence rate across the Nepal Himalaya and interseismic coupling on the Main Himalayan Thrust: Implications for seismic hazard. *Journal of Geophysical Research: Solid Earth*, *117*(4). https://doi.org/10.1029/2011JB009071

Austrheim, H., Erambert, M., & Engvik, A. K. (1997). Processing of crust in the root of the Caledonian continental collision zone: the role of eclogitization. *Tectonophysics*, *273*(1–2), 129–153.

Avouac, J.-P., Meng, L., Wei, S., Wang, T., & Ampuero, J.-P. (2015). Lower edge of locked Main Himalayan Thrust unzipped by the 2015 Gorkha earthquake. *Nature Geoscience*, *8*(9), 708–711.

Backus, G., & Gilbert, F. (1968). The resolving power of gross earth data. *Geophysical Journal International*, *16*(2), 169–205.

Bai, L., Klemperer, S. L., Mori, J., Karplus, M. S., Ding, L., Liu, H., et al. (2019). Lateral variation of the Main Himalayan Thrust controls the rupture length of the 2015 Gorkha earthquake in Nepal. *Science Advances*, *5*(6), eaav0723.

Beaumont, C., Jamieson, R. A., Nguyen, M. H., & Lee, B. (2001). Himalayan tectonics explained by extrusion of a low-viscosity crustal channel coupled to focused surface denudation. *Nature*, *414*(6865), 738–742.

Bensen, G. D., Ritzwoller, M. H., Barmin, M. P., Levshin, A. L., Lin, F., Moschetti, M. P., et al. (2007). Processing seismic ambient noise data to obtain reliable broad-band surface wave dispersion measurements. *Geophysical Journal International*, *169*(3), 1239–1260.

Bilham, R. (1995). Location and magnitude of the 1833 Nepal earthquake and its relation to the rupture zones of contiguous great Himalayan earthquakes. *Current Science*, *69*(2), 101–128.

Bilham, R. (2019). Himalayan earthquakes: a review of historical seismicity and early 21st century slip potential. *Geological Society, London, Special*

Publications, *483*(1), 423–482.

Bollinger, L, Lyon-Caen, H., & RESIF. (2011). HiK-NET temporary experiment (RESIF-SISMOB). RESIF - Réseau Sismologique et géodésique Français. https://doi.org/10.15778/RESIF.ZO2014

Bollinger, Laurent, Henry, P., & Avouac, J.-P. (2006). Mountain building in the Nepal Himalaya: Thermal and kinematic model. *Earth and Planetary Science Letters*, *244*(1–2), 58–71.

Castaldo, R., De Novellis, V., Solaro, G., Pepe, S., Tizzani, P., De Luca, C., et al. (2017). Finite element modelling of the 2015 Gorkha earthquake through the joint exploitation of DInSAR measurements and geologic-structural information. *Tectonophysics*, *714*, 125–132.

Copley, A., Avouac, J.-P., & Royer, J.-Y. (2010). India-Asia collision and the Cenozoic slowdown of the Indian plate: Implications for the forces driving plate motions. *Journal of Geophysical Research: Solid Earth*, *115*(B3).

Dettmer, J., & Dosso, S. E. (2012). Trans-dimensional matched-field geoacoustic inversion with hierarchical error models and interacting Markov chains. *The Journal of the Acoustical Society of America*, *132*(4), 2239–2250.

Duputel, Z., Vergne, J., Rivera, L., Wittlinger, G., Farra, V., & Hetényi, G. (2016). The 2015 Gorkha earthquake: a large event illuminating the Main Himalayan Thrust fault. *Geophysical Research Letters*, *43*(6), 2517–2525.

Elliott, J. R., Jolivet, R., González, P. J., Avouac, J.-P., Hollingsworth, J., Searle, M. P., & Stevens, V. L. (2016). Himalayan megathrust geometry and relation to topography revealed by the Gorkha earthquake. *Nature Geoscience*, *9*(2), 174–180.

Gorbatov, A., Saygin, E., & Kennett, B. L. N. (2013). Crustal properties from seismic station autocorrelograms. *Geophysical Journal International*, *192*(2), 861–870.

Grandin, R., Vallée, M., Satriano, C., Lacassin, R., Klinger, Y., Simoes, M., & Bollinger, L. (2015). Rupture process of the Mw= 7.9 2015 Gorkha earthquake (Nepal): Insights into Himalayan megathrust segmentation. *Geophysical Research Letters*, *42*(20), 8373–8382.

Guo, Z., Gao, X., Yao, H., Li, J., & Wang, W. (2009). Midcrustal low-velocity layer beneath the central Himalaya and southern Tibet revealed by ambient noise array tomography. *Geochemistry, Geophysics, Geosystems*, *10*(5).

Hébert, R., Huot, F., Wang, C., & Liu, Z. (2003). Yarlung Zangbo ophiolites (Southern Tibet) revisited: geodynamic implications from the mineral record. *Geological Society, London, Special Publications*, *218*(1), 165–190.

Henry, P., Le Pichon, X., & Goffé, B. (1997). Kinematic, thermal and petrological model of the Himalayas: constraints related to metamorphism within the underthrust Indian crust and topographic elevation. *Tectonophysics*, *273*(1–2), 31–56.

Herrmann, R. B. (2013). Computer programs in seismology: An evolving tool for instruction and research. *Seismological Research Letters*, *84*(6), 1081–1088.

Hochstein, M. P., & Regenauer-Lieb, K. (1998). Heat generation associated with collision of two plates: the Himalayan geothermal belt. *Journal of Volcanology and Geothermal Research*, *83*(1–2), 75–92.

Hodges, K. V. (2000). Tectonics of the Himalaya and southern Tibet from two perspectives. *Geological Society of America Bulletin*, *112*(3), 324–350.

Hsiao, N.-C., Wu, Y.-M., Shin, T.-C., Zhao, L., & Teng, T.-L. (2009). Development of earthquake early warning system in Taiwan. *Geophysical Research Letters*, *36*(5).

Jamieson, R. A., Beaumont, C., Medvedev, S., & Nguyen, M. H. (2004). Crustal channel flows: 2. Numerical models with implications for metamorphism in the Himalayan-Tibetan orogen. *Journal of Geophysical Research: Solid Earth*, *109*(B6).

Julià, J., Ammon, C. J., Herrmann, R. B., & Correig, A. M. (2000). Joint inversion of receiver function and surface wave dispersion observations. *Geophysical Journal International*, *143*(1), 99–112. https://doi.org/10.1046/j.1365-246x.2000.00217.x

Kennett, B. (1983). *Seismic wave propagation in stratified media*. ANU Press.

Kennett, B. L. N. (2015). Lithosphere--asthenosphere P-wave reflectivity across Australia. *Earth and Planetary Science Letters*, *431*, 225–235.

Kennett, B. L. N., Saygin, E., & Salmon, M. (2015). Stacking autocorrelograms to map Moho depth with high spatial resolution in southeastern Australia. *Geophysical Research Letters*, *42*(18), 7490–7497.

Khan, M. A. (2013). Seismic Design for Buildings. In *Earthquake-Resistant Structures* (pp. 283–315). Elsevier. https://doi.org/10.1016/B978-1-85617-501-2.00010-9

Lavé, J., & Avouac, J.-P. (2000). Active folding of fluvial terraces across the Siwaliks Hills, Himalayas of central Nepal. *Journal of Geophysical Research: Solid Earth*, *105*(B3), 5735–5770.

Lemonnier, C., Marquis, G., Perrier, F., Avouac, J.-P., Chitrakar, G., Kafle, B., et al. (1999). Electrical structure of the Himalaya of central Nepal: High conductivity around the mid-crustal ramp along the MHT. *Geophysical Research Letters*, *26*(21), 3261–3264. https://doi.org/10.1029/1999GL008363

Lin, F.-C., Ritzwoller, M. H., Townend, J., Bannister, S., & Savage, M. K. (2007). Ambient noise Rayleigh wave tomography of New Zealand. *Geophysical Journal International*, *170*(2), 649–666.

Lindsey, E. O., Natsuaki, R., Xu, X., Shimada, M., Hashimoto, M., Melgar, D., & Sandwell, D. T. (2015). Line-of-sight displacement from ALOS-2 interferometry: Mw 7.8 Gorkha Earthquake and Mw 7.3 aftershock. *Geophysical Research Letters*, *42*(16), 6655–6661.

Manu-Marfo, D., Aoudia, A., Pachhai, S., & Kherchouche, R. (2019). 3D shear wave velocity model of the crust and uppermost mantle beneath the Tyrrhenian basin and margins. *Scientific Reports*, *9*(1), 1–10.

Martin, S. S., Hough, S. E., & Hung, C. (2015). Ground motions from the 2015 M w 7.8 Gorkha, Nepal, earthquake constrained by a detailed assessment of macroseismic data. *Seismological Research Letters*, *86*(6), 1524–1532.

McKenna, L. W., & Walker, J. D. (1990). Geochemistry of crustally derived leucocratic igneous rocks from the Ulugh Muztagh area, northern Tibet and their implications for the formation of the Tibetan Plateau. *Journal of Geophysical Research: Solid Earth*, *95*(B13), 21483–21502.

Mitra, S., Priestley, K., Gaur, V. K., Rai, S. S., & Haines, J. (2006). Variation of Rayleigh wave group velocity dispersion and seismic heterogeneity of the Indian crust and uppermost mantle. *Geophysical Journal International*, *164*(1), 88–98.

Molnar, P. (1984). Structure and tectonics of the Himalaya: Constraints and implications of geophysical data. *Annual Review of Earth and Planetary Sciences*, *12*(1), 489–516.

Molnar, P., England, P., & Martinod, J. (1993). Mantle dynamics, uplift of the Tibetan Plateau, and the Indian monsoon. *Reviews of Geophysics*, *31*(4), 357–396.

Monsalve, G., Sheehan, A. F., Pandey, M. R., Rajaure, S., & Wu, F. (2006). Seismicity and 1-D velocity structure of the Himalayan collision zone: results from the Himalayan Nepal Tibet Seismic Experiment (HIMNT). *J. Geophys. Res*, *111*, B10301.

Monsalve, G., Sheehan, A., Rowe, C., & Rajaure, S. (2008). Seismic structure of the crust and the upper mantle beneath the Himalayas: Evidence for eclogitization of lower crustal rocks in the Indian Plate. *Journal of Geophysical Research: Solid Earth*, *113*(B8).

Murphy, M. A., & Yin, A. (2003). Structural evolution and sequence of thrusting in the Tethyan fold-thrust belt and Indus-Yalu suture zone, southwest Tibet. *Geological Society of America Bulletin*, *115*(1), 21–34.

Nabelek, J. (2002). Collaborative Research: Lithospheric Scale Dynamics of Active Mountain Building along the Himalayan-Tibetan Collision Zone. International Federation of Digital Seismograph Networks. https://doi.org/10.7914/SN/XF_2002

Nábělek, J., Hetényi, G., Vergne, J., Sapkota, S., Kafle, B., Jiang, M., et al. (2009). Underplating in the Himalaya-Tibet collision zone revealed by the Hi-CLIMB experiment. *Science*, *325*(5946), 1371–1374.

Nelson, K. D., Zhao, W., Brown, L. D., Kuo, J., Che, J., Liu, X., et al. (1996). Partially molten middle crust beneath southern Tibet: synthesis of project INDEPTH results. *Science*, *274*(5293), 1684–1688.

Pachhai, S, Tkalčić, H., & Dettmer, J. (2014). Bayesian inference for ultralow

velocity zones in the Earth's lowermost mantle: complex ULVZ beneath the east of the Philippines. *Journal of Geophysical Research: Solid Earth*, *119*(11), 8346–8365.

Pachhai, Surya, Dettmer, J., & Tkalčić, H. (2015). Ultra-low velocity zones beneath the Philippine and Tasman Seas revealed by a trans-dimensional Bayesian waveform inversion. *Geophysical Journal International*, *203*(2), 1302–1318.

Pandey, M. R., Tandukar, R. P., Avouac, J. P., Lave, J., & Massot, J. P. (1995). Interseismic strain accumulation on the Himalayan crustal ramp (Nepal). *Geophysical Research Letters*, *22*(7), 751–754.

Paulssen, H., Visser, J., & Nolet, G. (1993). The crustal structure from teleseismic P-wave coda—I. Method. *Geophysical Journal International*, *112*(1), 15–25.

Pham, T. S., & Tkalcic, H. (2017). On the feasibility and use of teleseismic P wave coda autocorrelation for mapping shallow seismic discontinuities. *Journal of Geophysical Research: Solid Earth*, *122*(5), 3776–3791.

Pham, T. S., & Tkalcic, H. (2018). Antarctic ice properties revealed from teleseismic P wave coda autocorrelation. *Journal of Geophysical Research: Solid Earth*, *123*(9), 7896–7912.

Pilia, S., Jackson, J. A., Hawkins, R., Kaviani, A., & Ali, M. Y. (2020). The southern Zagros collisional orogen: new insights from transdimensional trees inversion of seismic noise. *Geophysical Research Letters*, *47*(4), e2019GL086258.

Randall, G. E. (1989). Efficient calculation of differential seismograms for lithospheric receiver functions. *Geophysical Journal International*, *99*(3), 469–481.

Rawlinson, N., Houseman, G. A., & Collins, C. D. N. (2001). Inversion of seismic refraction and wide-angle reflection traveltimes for three-dimensional layered crustal structure. *Geophysical Journal International*, *145*(2), 381–400.

Royden, L. H. (1993). The steady state thermal structure of eroding orogenic belts and accretionary prisms. *Journal of Geophysical Research: Solid Earth*, *98*(B3), 4487–4507.

Ruigrok, E., & Wapenaar, K. (2012). Global-phase seismic interferometry unveils P-

wave reflectivity below the Himalayas and Tibet. *Geophysical Research Letters*, *39*(11).

Sapkota, S. N., Bollinger, L., Klinger, Y., Tapponnier, P., Gaudemer, Y., & Tiwari, D. (2013). Primary surface ruptures of the great Himalayan earthquakes in 1934 and 1255. *Nature Geoscience*, *6*(1), 71–76.

Saygin, E., Cummins, P. R., & Lumley, D. (2017). Retrieval of the P wave reflectivity response from autocorrelation of seismic noise: Jakarta Basin, Indonesia. *Geophysical Research Letters*, *44*(2), 792–799.

Schimmel, M., & Paulssen, H. (1997). Noise reduction and detection of weak, coherent signals through phase-weighted stacks. *Geophysical Journal International*, *130*(2), 497–505.

Schulte-Pelkum, V., Monsalve, G., Sheehan, A., Pandey, M. R., Sapkota, S., Bilham, R., & Wu, F. (2005). Imaging the Indian subcontinent beneath the Himalaya. *Nature*, *435*(7046), 1222–1225.

Shapiro, N. M., & Campillo, M. (2004). Emergence of broadband Rayleigh waves from correlations of the ambient seismic noise. *Geophysical Research Letters*, *31*(7).

Shapiro, N. M., Campillo, M., Stehly, L., & Ritzwoller, M. H. (2005). High-resolution surface-wave tomography from ambient seismic noise. *Science*, *307*(5715), 1615–1618.

Sheehan, A. (2001). Himalayan Seismotectonics, Nepal and Tibet. International Federation of Digital Seismograph Networks. https://doi.org/10.7914/SN/YL_2001

Sheehan, A. F., de la Torre, T. L., Monsalve, G., Abers, G. A., & Hacker, B. R. (2014). Physical state of Himalayan crust and uppermost mantle: Constraints from seismic attenuation and velocity tomography. *Journal of Geophysical Research: Solid Earth*, *119*(1), 567–580.

Sun, W., & Kennett, B. L. N. (2016). Receiver structure from teleseisms: Autocorrelation and cross correlation. *Geophysical Research Letters*, *43*(12), 6234–6242.

Unsworth, M. J., Jones, A. G., Wei, W., Marquis, G., Gokarn, S. G., & Spratt, J. E. (2005). Crustal rheology of the Himalaya and Southern Tibet inferred from magnetotelluric data. *Nature*, *438*(7064), 78–81.

Upreti, B. N. (1999). An overview of the stratigraphy and tectonics of the Nepal Himalaya. *Journal of Asian Earth Sciences*, *17*(5–6), 577–606.

Verbeke, J., Boschi, L., Stehly, L., Kissling, E., & Michelini, A. (2012). High-resolution Rayleigh-wave velocity maps of central Europe from a dense ambient-noise data set. *Geophysical Journal International*, *188*(3), 1173–1187.

Wang, X.-Q., Schubnel, A., Fortin, J., David, E. C., Guéguen, Y., & Ge, H.-K. (2012). High Vp/Vs ratio: Saturated cracks or anisotropy effects? *Geophysical Research Letters*, *39*(11), n/a-n/a. https://doi.org/10.1029/2012GL051742

Wang, X., Wei, S., & Wu, W. (2017). Double-ramp on the Main Himalayan Thrust revealed by broadband waveform modeling of the 2015 Gorkha earthquake sequence. *Earth and Planetary Science Letters*, *473*, 83–93. https://doi.org/10.1016/j.epsl.2017.05.032

Xu, Q., Zhao, J., Yuan, X., Liu, H., & Pei, S. (2015). Mapping crustal structure beneath southern Tibet: Seismic evidence for continental crustal underthrusting. *Gondwana Research*, *27*(4), 1487–1493.

Xu, Z. J., Song, X., & Zhu, L. (2013). Crustal and uppermost mantle S velocity structure under Hi-CLIMB seismic array in central Tibetan Plateau from joint inversion of surface wave dispersion and receiver function data. *Tectonophysics*, *584*, 209–220.

Yang, Y., & Ritzwoller, M. H. (2008). Characteristics of ambient seismic noise as a source for surface wave tomography. *Geochemistry, Geophysics, Geosystems*, *9*(2).

Yang, Y., Zheng, Y., Chen, J., Zhou, S., Celyan, S., Sandvol, E., et al. (2010). Rayleigh wave phase velocity maps of Tibet and the surrounding regions from ambient seismic noise tomography. *Geochemistry, Geophysics, Geosystems*, *11*(8).

Yanovskaya, T. B., & Ditmar, P. G. (1990). Smoothness criteria in surface wave

tomography. *Geophysical Journal International*, *102*(1), 63–72.

Yanovskaya, T. B., Kizima, E. S., & Antonova, L. M. (1998). Structure of the crust in the Black Sea and adjoining regions from surface wave data. *Journal of Seismology*, *2*(4), 303–316.

Zhang, L., Li, J., Liao, W., & Wang, Q. (2016). Source rupture process of the 2015 Gorkha, Nepal Mw7. 9 earthquake and its tectonic implications. *Geodesy and Geodynamics*, *7*(2), 124–131.

Zhao, W., Nelson, K. D., Che, J., Quo, J., Lu, D., Wu, C., & Liu, X. (1993). Deep seismic reflection evidence for continental underthrusting beneath southern Tibet. *Nature*, *366*(6455), 557–559.

Acknowledgement

I would like to acknowledge the guidance and support I have received from my supervisors Prof. Abdelkrim Aoudia and Dr. Surya Pachhai. I am always grateful for their encouragement and assistance. This project would not have succeeded without their guidance and persistent help. I acknowledge “The Abdus Salam International Centre for Theoretical Physics (ICTP)” for funding provided for this work.

I am thankful to Dr. Daniel Manu-Marfo for his continuous support and inspiration throughout this work. I would like to express my sincere thanks to all my respected faculty members of Solid-Earth Geophysics, ICTP and the ICTP staffs.

I would like to express my sincere thanks to my seniors Dr. Blaz Vicic and Dr. Amir Sadeghi-Bagherabadi for their help and scientific advice. I am also thankful to my friends Sisay Alemayehu, Donna Bou-Rabbe and Alvina Kusumadewi Kuncoro with whom I enjoy every academic and non-academic discussions which adds a morale-boost in my work. I am thankful to two anonymous reviewers Prof. Supriyo Mitra and Prof. Naresh Kumar for their comments on my thesis. I would like to acknowledge

Indian Institute of Science Education and Research Kolkata (IISER-K) for providing the data of six seismic stations.

Finally, I am grateful to my lovely fiancée Apsara Sharma Dhakal for her support and encouragement throughout this work. I would like to dedicate this thesis to my parents, whose immense support in each and every step of my life, help to reinforce my morale.